Spectroscopic and mechanistic investigation of the enzyme mercaptopropionic acid dioxygenase (MDO), the role of the conserved outer-sphere 'catalytic triad' in directing promiscuous substrate-specificity

A DISSERTATION

Presented to the faculty of the Graduate School of

The University of Texas at Arlington in Partial fulfillment

Of the requirements of the Degree of

Doctor in Philosophy in

CHEMISTRY

by

SINJINEE SARDAR

Under the guidance of

Dr. Brad S. Pierce

2nd May, 2018

ACKNOWLEDGEMENT

It gives me immense pleasure to thank my compassionate guide Dr. Brad S. Pierce, for his exemplary guidance to accomplish this work. It has been an extraordinary pleasure and privilege to work under his guidance for the past few years.

I express my sincere gratitude to my doctoral committee members Prof. Frederick. MacDonnell, Dr. Rasika Dias, and Dr. Jongyun Heo for their valuable advice and constant help. I would also like to thank the Department of Chemistry and Biochemistry of UTA for bestowing me the opportunity to have access to all the departmental facilities required for my work.

Here, I express my heartiest gratitude to the ardent and humane guidance of my senior lab mates Dr. Josh Crowell and Dr. Bishnu Subedi which was indispensable. I am immeasurably thankful to my lab mates Wei, Mike, Phil, Nick, Jared and Sydney for their constant support and help. It has been a pleasure to working with all of you. The jokes and laughter we shared have reduced the hardships and stress of graduate school and had made the stressful journey fun.

To end with, I utter my heartfelt gratefulness to my parents and my sister for their lifelong support and encouragement which helped me chase my dreams and aspirations and sincere appreciation towards my friends who are my extended family for their lively and spirited encouragement.

2nd April,2018

Abstract

Spectroscopic and mechanistic investigation of the enzyme mercaptopropionic acid dioxygenase (MDO), the role of the conserved outer-sphere 'catalytic triad' in directing promiscuous substrate-specificity

Sinjinee Sardar, Ph.D.

The University of Texas, Arlington

Supervising professor: Dr. Brad. S. Pierce

Mercaptopropionate dioxygenase (MDO) from *Aztobacter Vinelandii* is a non-heme mononuclear iron enzyme that catalyzes the oxygen dependent conversion of 3-mercaptopropionic acid (***3mpa***) to produce 3-sulfinopropinioic acid (***3spa***). Nearly, all thiol dioxygenases have a conserved '*catalytic triad*' within the active site, consisting of three outer Fe-coordination sphere residues S155, H157 and Y159. With the notable exception of mammalian cysteamine (2-aminoethanethiol) dioxygenase (ADO), this '*catalytic triad*' is universally conserved across phylogenic domains. X-ray crystallographic studies clearly show a hydrogen bond network connecting the '*catalytic triad*' to the mononuclear iron site; however, its influence on substrate specificity and catalytic efficiency is poorly understood. In this work, kinetic and spectroscopic characterization of *Av*MDO is presented, focusing especially on the role of the conserved 'catalytic triad' on enzyme catalysis. In addition, pH/pD-dependent to solvent kinetic isotope (SKIE) experiments and proton inventory experiments were performed to investigate rate limiting proton-dependent steps during catalysis. Complementary viscosity studies are presented to probe diffusion limited steps in steady-state reactions.

Comparative studies were performed for reactions with L-cysteine and 3mpa as a substrate, for the active site variants, H157N and Y159F to investigate the role of specific residues within the 'catalytic triad'. Taken together with supporting EPR and Mössbauer spectroscopic studies, a mechanistic model is proposed in which the '*catalytic triad*' serves to gate proton delivery to the substrate-bound Fe-site. These studies suggest that the primary role of the '*catalytic triad*' is to neutralize the negative charge of the substrate-carboxylate group in the rate-limiting non-chemical steps leading up to O_2-activation.

Table of contents

Chapter 3 Solvent kinetic isotope effects on 3-Mercaptopropionic acid dioxygenase(MDO) from Azotobacter vinelandii reveals ionization events associated with substrate binding are rate limiting

Chapter 4: Thiol dioxygenase turnover yields benzothiazole products from 2-mercaptoaniline and O_2-dependent oxidation of primary alcohols.

List of Illustrations

List of Tables

List of schemes

Chapter 1: Introduction to Non-heme iron enzymes

The reductive activation of dioxygen, though thermodynamically favorable, is a spin-forbidden process. In its ground triplet state, $^3O_2$ is paramagnetic whereas organic substrates and their corresponding oxygenated products are diamagnetic. As the spin-angular momentum of products and reactants are not conserved, the reaction is termed 'spin-forbidden' and is kinetically slow. In nature, enzymes utilize transition metals, which can adopt multiple d^n-electronic configurations to overcome this kinetic barrier.[1, 2]Among oxidases/oxygenase enzymes, copper and iron are the most commonly utilized metals, however a few Mn-dependent dioxygenases have been reported in the literature.[3] Among the Fe-dependent oxidase/oxygenases, the specific chemical mechanism carried out by each enzyme is largely defined the presence of heme (protoporphyrin IX) cofactor and the number of iron atoms within the active site.[4]

All oxygen activating enzymes can be classified into two groups, oxidases and oxygenases. Oxidases catalyze the oxidation of a substrate in redox reactions, whereas, oxygenases incorporate oxygen atoms into the substrates to form products. Number of oxygen atoms incorporated determines whether the enzyme will be called as a monooxygenase or a dioxygenase enzyme. Alternatively based on the active site structures, iron-containing oxidases/oxygenases can be divided into two groups based on the active site structures, i.e. heme and non-heme containing enzymes. The non-heme iron enzymes can in turn be divided in mononuclear and dinuclear iron enzymes.[5]

Historically, non-heme Fe enzymes have been of considerable interest given the remarkable diversity of chemical oxidation reactions catalyzed by these enzymes. The array of catalysis carried out these enzymes includes hydroxylation, epoxidation, homolytic and heterolytic cleavage of carbon-carbon bonds and heterocyclic ring formation.[6] Heme oxidase/oxygenase enzymes utilize a strong field macrocyclic porphyrin ligand (protoporphyrin IX) and one protein derived amino acid (Cys, Tyr, His) to coordinate a mononuclear iron within the enzymatic active site.[2] The open 6-coordination site remains open for inner-sphere O_2-coordination and subsequent activation. Conversely, non-heme iron enzymes lack a heme moiety cofactor. Instead, either a mononuclear or dinuclear iron cluster is coordinated within the enzymatic site by protein derived ligands; typically, histidine (σ-only) and glutamate and/or aspartate (π-donor).

Enzymes, which carry out a 2-electron oxidation process, often need an external electron sources or cofactors like Nicotinamide adenosine dinucleotide phosphate(NADP) etc. Conversely, mononuclear dioxygenases do not require an external electron source as they can carry out 4-electron oxidation of the substrate without the need for external electron source.[7] The advantage of binding extra ligand/cofactors gives the enzymes opportunity to tune the different redox states of the Fe center itself.

Crystallographic data available for these mononuclear enzymes reveal a common structural feature among many of those enzymes, consisting of two neutral histidine and a monoanionic aspartate/glutamate residue at the active site attached to the metal center, occupying one face of the octahedron. The remaining sites, opposite to the facial triad, are open to bind to cofactors, substrates and molecular oxygen. This structural motif is named as the 2-His-1-carboxylate facial triad.[8]

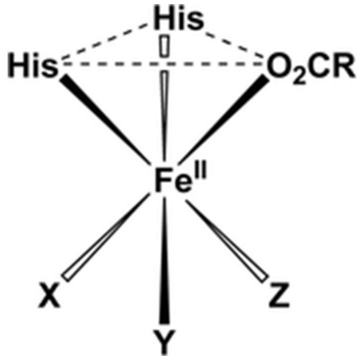

Figure 1-1: 2-His-1-carboxylate facial triad[2]

This structural feature has been established in more than 30 different enzymes and considered to be one of nature's recurring motifs[6] and it is conserved among enzymes. The flexibility of the outer-sphere residues surrounding the conserved 2-His-1-carboxylate motif is largely believed to 'tune' the active site for specific reactivities and substrate preferences.

One of the interesting aspect of the reaction mechanism carried out by this superfamily of enzyme is the "obligated ordered" addition of substrate prior to dioxygen binding.[9] Typically, the six-coordinated reduced active site is unreactive towards molecular oxygen. Instead, only the substrate bound enzyme is reactive towards oxygen. In the first step, binding of oxygen to the substrate-bound ferrous active site results in an internal electron transfer producing a short-lived ferric-superoxo [Fe^{III}-$O_2^{\bullet-}$] species.[10] The reaction mechanism diverges from this point onwards in case of different enzymes depending their function. In most of the cases, the O-O bond cleavage and occurrence of high valent Fe-oxo species take place.[11] Various literature shows evidence of formation of high valent Fe-oxo species in case of α-ketoglutarate dependent enzymes TauD,[12] on the other hand in case of enzyme Isopenicilin N-synthase (IPNS) formation of Fe(III)-superoxide as the oxidizing species, has been suggested.[13]

Depending upon the nature of the reactive iron-oxo intermediate dictates whether the enzyme is going carry out oxygenase or oxidase function.

Classification of enzymes bearing 2-His-1carboxylate facial triad

Among non-heme mononuclear iron enzymes, the 2-his-1-carboxylate motif is utilized to catalyze a variety of chemical transformations. Depending on their functions, these enzymes can be classified into five main categories, Table 1 provides s a brief description of the enzymes, the detailed accounts of the structures and functions are described later.

Table 1-1: Summary of structure and function for non-heme iron enzymes -

Enzyme family	Enzyme	Function
Catechol dioxygenase	2,3- HPCD, 4,5- PCD, BphC	Phenolic C-C bond cleavage
Rieske dioxygenase	NDO	Cis-dehydroxylation of arenes
α-ketogulate dependent enzymes	TauD, ANS, DAOCS, HPPD	Oxidation and C-H bond activation
Pterin dependent hydroxylases	PheOH, TyrOH, TryOH	Biosynthesis of amino acids
Other enzymes	ACCO, IPNS, TDO	Biosynthesis of antibiotics

Catechol cleaving dioxygenases

Catechol cleaving dioxygenases are non-heme mononuclear iron enzymes that are found in soil bacteria. These enzymes are involved in the biodegradation of aromatic compounds by oxidative bond cleavage of catechol (dihydroxybenzene) and its derivatives.[14] Two principal classes of catechol dioxygenases have been identified, which are classified based on their regioselectivity of bond cleavage. Intradiol catechol dioxygenase cleaves the enediol C-C bond whereas the extradiol catechol dioxygenase cleaves the C-C bond adjacent to the enediol bond. Though they carry out the same cleaving mechanism their respective reaction pathways are quite different from each other.[15]

The metal active centers and the coordination around the active site for the two catechol dioxygenases differ from each other as well.[16]

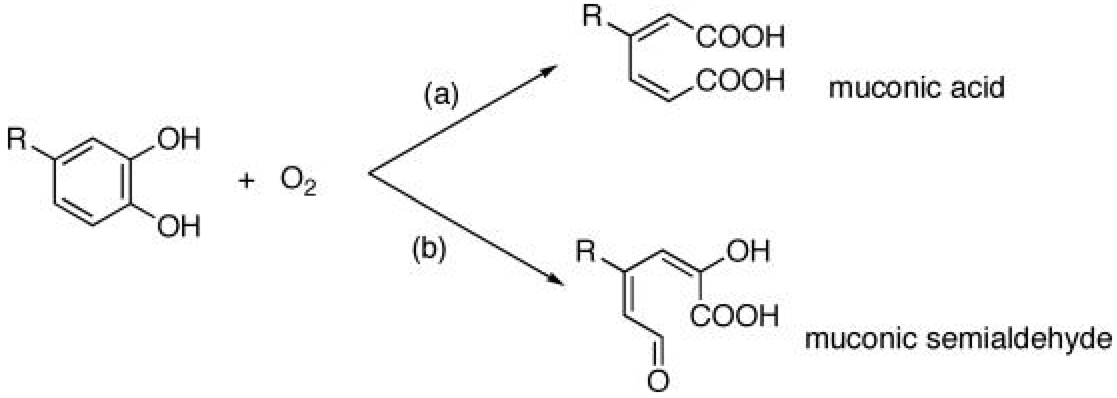

Scheme 1-2: Ring cleavage by a) Intradiol and b) Extradiol catechol dioxygenase enzymes

Unlike the aforementioned 2-His-1-carboxylate active site co-ordination, intradiol catechol dioxygenases contain a mononuclear ferric iron site coordinated 2-histidine, 2- tyrosine residues and a fifth hydroxide resulting in a 5-coordinate trigonal bipyramidal geometry. Whereas, the extradiol enzyme has a Fe(II) center with 2-histidine and 1-glutamate residue forming a square pyramidal geometry with the occupation of the other two co-ordination sites by water molecules. Thus, the metal center is positively charged.[17]

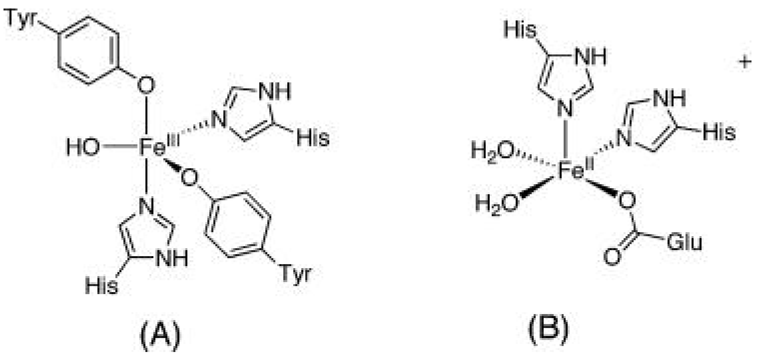

Figure 1-2: Active site structure of A) Intradiol and B) Extradiol dioxygenase enzyme

Though extradiol cleavage is more common in nature, the intradiol dioxygenases system has garnered considerably more attention. The ease of studying Fe(III) compared to a Fe(II) spectroscopically, probably have attributed to the fact.[12, 18] With the availability of multiple X-ray crystal studies, a great deal of structural and mechanistic information is available for this sub-class of non-heme iron enzymes.

Extradiol catechol cleaving enzyme binds with the substrate after displacing the two water molecules from the active site, leaving one open co-ordination site for the O_2 molecule. The Fe(III)-O_2 superoxide species is formed instead of high valent Fe -oxo species.[19] The higher Lewis acidity of the Fe-center favors the deprotonation of the already monoanionic substrate, the superoxide species then activates the semiquinone radical on the substrate,[20] forming an Fe-alkyl-peroxo complex. The formation of this intermediate is observed in the crystal structure using of 2,3-homoprotochatacute dioxygenase with 2-nitrocatechol. The complex then takes in one O atom to form a seven-membered lactone ring which later gets hydrolyzed to form muconic aldehyde product.[21]

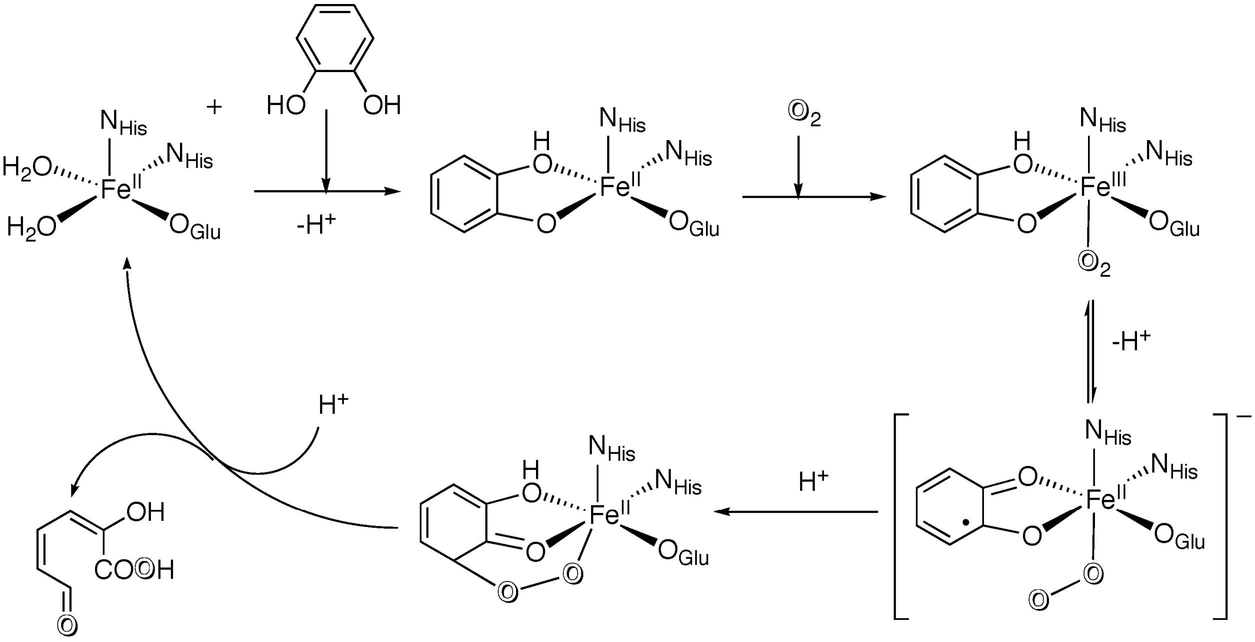

Scheme 1-3: Proposed mechanism of extradiol cleavage

Intradiol catechol cleaving dioxygenases like their extradiol counterpart also bind its substrate bidentate, but there is no evidence of Fe(III) getting reduced to Fe(II). The presence of high spin Fe(III) species was proven by EPR and Mössbauer spectroscopy after chelation with substrate catechol. The 2His-2Tyr motif at the active site is perturbed by substrate binding and turns into 2-his-1-tyr motif by displacing the axial tyrosine.[22] Unlike in the mechanism for extradiol dioxygenase, in this case O_2 doesn't co-ordinate directly to the Fe site.

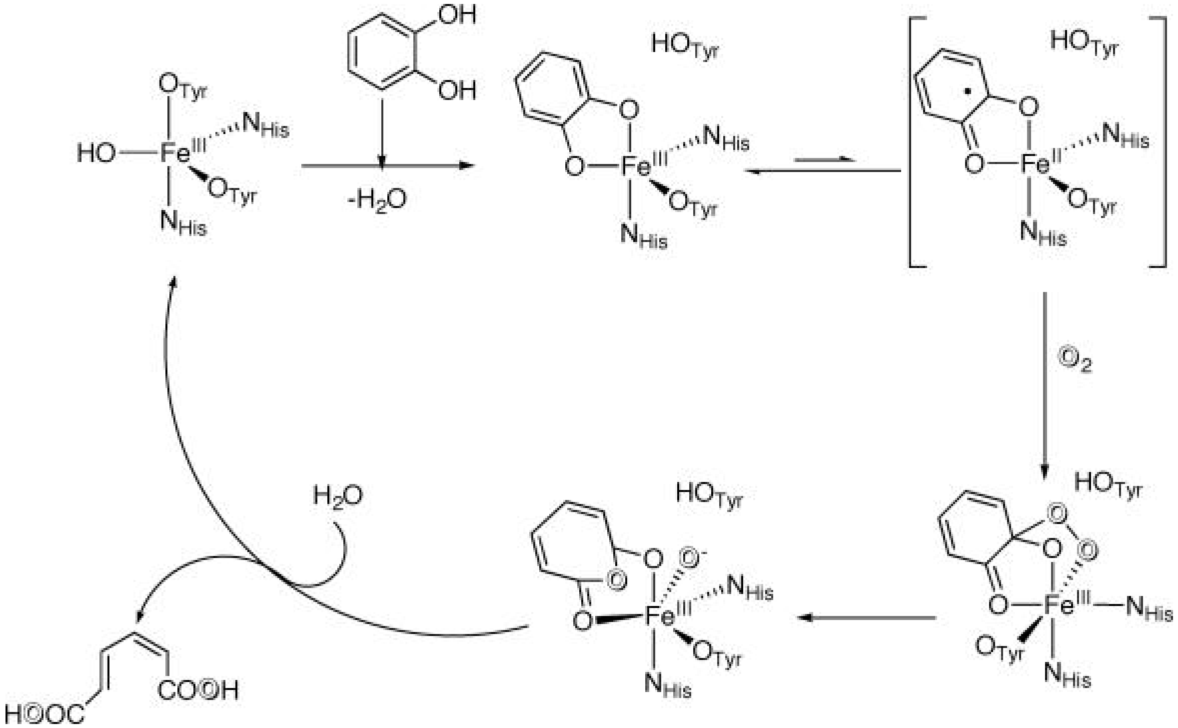

Scheme 1-4: Proposed mechanism of intradiol cleavage

Instead, the electron transfer between the ligand and metal center gives rise to a short-lived Fe(II) species which in turn is attacked by a radical formed on oxygen.[23] This reaction allows molecular oxygen to attack the semiquinone attached to the substrate which gives rise to the hydroperoxide intermediate species. After this, the intermediate undergoes Criegee rearrangement to yield the muconic acid product.[21]

Rieske dioxygenase

This class of non heme iron enzyme are multicomponent systems which are primarily found in soil bacteria and they catalyze the cis-hydroxylation of polyaromatic hydrocarbons.[24] These dioxygenases form cis-diols both regioselectively and stereospecifically. These cis-diols are further metabolized by catechol cleaving dioxygenase discussed in the previous section. Polyaromatic hydrocarbons are recognized as serious environmental pollutants, the Rieske dioxygenases are of importance for bioremediation.[19] Other than cis-hydroxylation, these enzymes perform a vast array of other oxygenation reactions including mono-dehydroxylation, sulfoxidation, desaturation, N-and O-dealkylation and amine oxidation. Below, are a few examples of reactions carried out by this class of enzymes.[20, 21, 24]

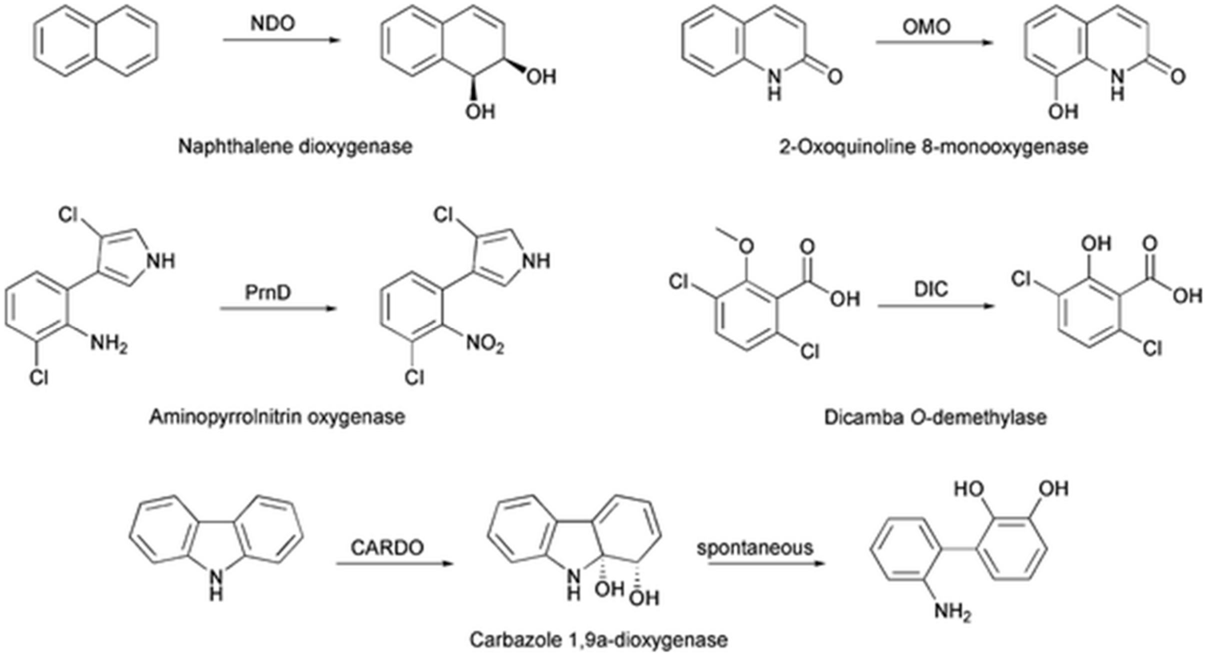

Scheme1-5: Reactions catalyzed by various Rieske dioxygenases

The Rieske dioxygenases are multiple component enzymes that consist of a) flavoprotein reductase that houses a Rieske-type [2Fe-2S] cluster b) ferredoxin and c) an oxygenase component. Generally, the substrate oxidation occurs in the oxygenase component which contains Rieske [2Fe-2] and a mononuclear Fe active site. The Rieske center differs from typical ferredoxin Fe-S cluster in their by means of higher redox potential (typically 100-200 mV more positive) and by increased anisotropy observed by EPR spectroscopy (g_{obs} of 2.0, 1.9 and 1.7).[23] Out of the four-electron required for full reduction, two are provided by the substrate and the other two are provided by

NADPH. The later of which are shuttled into the oxygenase active site by the Rieske-[2Fe-2S] cluster and the reductase unit[24] and then moves to the non-heme active site.

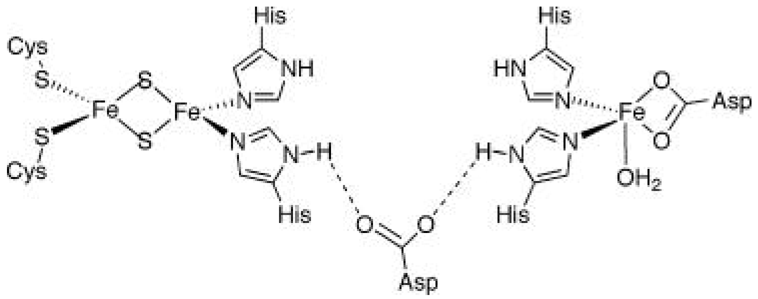

Figure 1-3: Active site structure of a arene cis-hydroxylating oxygenase

In a single sub-unit of the enzyme the Fe-S cluster and non-heme iron site is too far apart (~45Å) for electron transfer but in the quaternary structure the iron site comes close to another Rieske center (~12Å) by folding, thereby allowing the electron transfer. It is believed the aspartate bridge between the subunits plays a crucial role in electron transfer. Single site mutation of this aspartate leads to loss of catalytic activity.[25] It has been proven, that the substrate does not directly bind the active site, instead, is housed in the vicinity. The entire reaction is controlled by the change in redox states of the Rieske factors allosterically.[26] The obligate ordered attachment of oxygen is gated by substrate and the attachment (away from the active site) converts the active site into a five-coordinated geometry, which in turn opens the channel for binding oxygen.

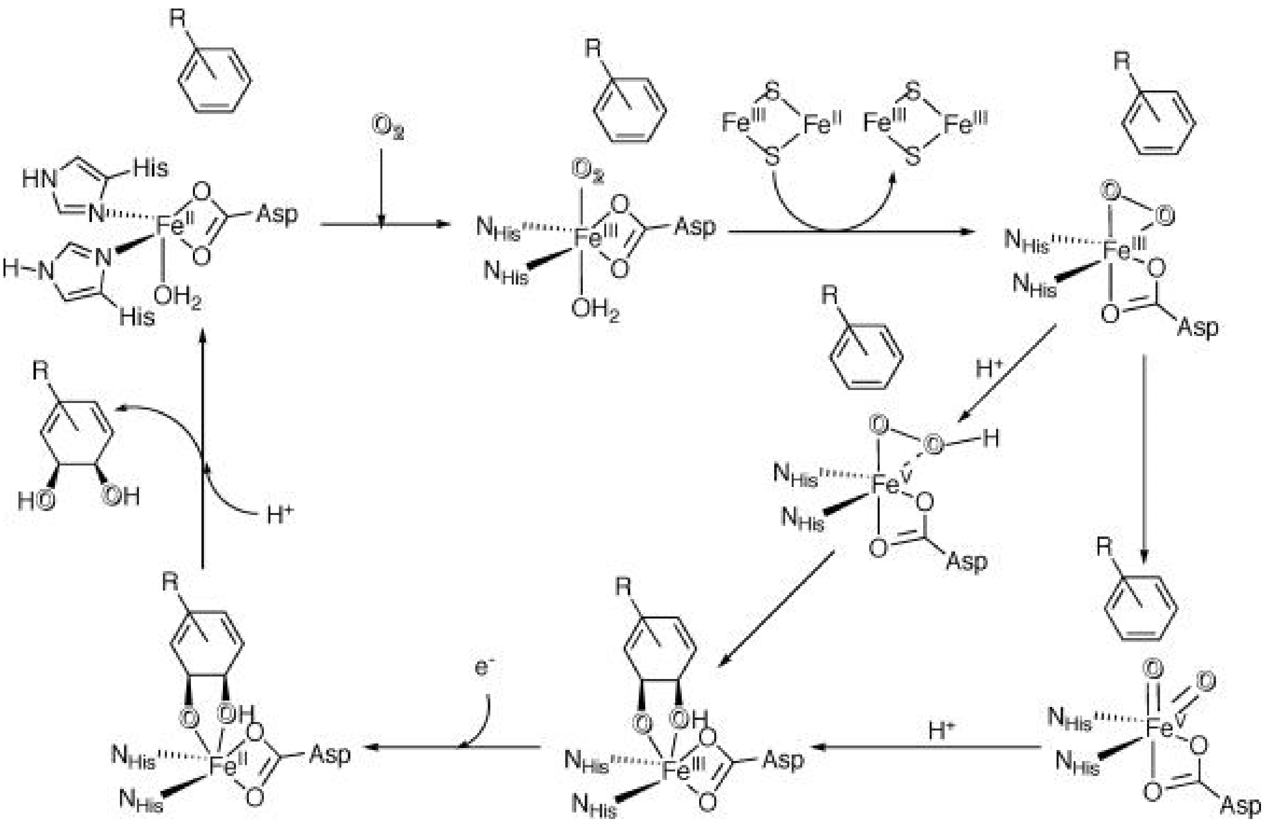

Scheme 1-6: Proposed mechanism for arene-cis dihydroxylation catalyzed by Rieske dioxygenase

Naphthalene dioxygenase (NDO), the most studied enzyme belonging to this class of enzymes, has an oxygenase unit which consists of a non-heme mononuclear iron center, attached to 2-histidine, one bidentate aspartate residue and water in its first co-ordination sphere.[24]The crystal structure of the said unit of NDO from *P. Putida* is the only three-dimensional structure reported of this component for the entire class of enzyme and it shows that the oxygen binding in this case deviates from the traditional end-on binding and shows an unusual η^2-coordination. The binding is immediately followed by a reduction step induced by electron transfer from the Rieske cluster, forming the species Fe(III)-η^2-O_2.[19] Though various reaction mechanisms have been suggested regarding the fate and the function of hydroperoxide. Computational studies suggest that at this stage of the reaction the substrate is attacked directly by the Fe(III)-η^2-O_2 and an arene radical species is formed. This step is followed by addition of another oxygen molecule attaching to the radical species.[20] Another proposed mechanism suggests reduction of the oxy complex by one electron to form a Fe(III)-peroxo species intermediate, followed by O-O heterolysis to form a high-valent Fe-oxo species, followed by oxidation of substrate and reduction of the Fe center back to the Fe(III) state.[21] The cleavage of the O-O bond gives rise to many anionic and cationic radical species as proven by isotope labelling studies which show exchange of labelled oxygen between the active species and the enzyme.[22] The selectivity demonstrated by the Rieske dioxygenase enzymes are determined by the orientation of the substrate in the protein binding pocket, and physical interactions such as hydrogen bonding between the residues and the incoming substrate determine the spatial orientations.[23]

α-Ketoglutarate dependent enzyme

The α-Ketoglutarate dependent enzyme or 2-oxoglutarate enzyme family is the largest subfamily of enzymes containing the 2-his-1- carboxylate motif in their active site. The decarboxylation reaction of the α-ketoglutarate co-factor acts as the external electron source during catalysis. This family of enzymes consist of versatile oxidizing biological catalysts which take part in various oxidation reactions including ring closure, ring expansion, desaturation, dehydroxylation, oxygen-atom transfer etc.[27] and take part in various biological processes including repair of DNA/RNA, biosynthesis of antibiotics, regulation of transcription. These enzymes are also one of the most studied systems in biological sciences due to the importance of the reactions carried out by them.[18]

Abundance of available crystallographic data on various α-ketoglutarate dependent enzymes have provided structural information which lead to interpreting the general mechanism involving the enzymes.[6] The active site of these enzymes consists of 2-His-1-carboxylate facial triad bound to Fe(II), and in the resting state, three molecules of water occupy the free co-ordination sites. Based on the steady state kinetic data, it was shown, first the α-ketoglutarate co-factor binds the Fe center bidentate and displaces two water molecules.[18]

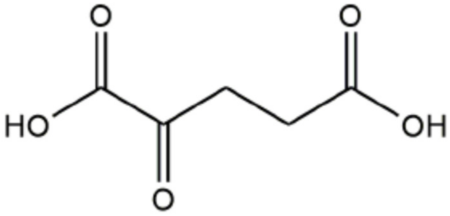

Figure 1-4: General structure of α-ketoglutarate cofactor

The substrates in this case do not bind directly to the active site, instead they bind to a site adjacent to the metal center and it is held in position by interaction of the C5 hydroxylate from the conserved resides in the vicinity. Afterwards, the third water molecule displaces and oxygen binds directly to the metal forming Fe(III)-($O_2^{\bullet -}$) species followed by a series of reduction reactions involving the α-ketoglutarate cofactor [28] . The nucleophilic attack by the ketone at the α- position of the co-factor and the terminal oxygen molecule from Fe-superoxo intermediate forms a bicyclic structure[29]. The next step involves decarboxylation and O-O bond cleavage to form a succinate molecule and yielding the high valent Fe(IV)=O species. This species is believed to be involved in the 2-electron oxidation of substrate.[30]

TauD or Taurine/α-ketoglutarate dioxygenase is one the most characterized enzymes from this family. In TauD, a ferryl intermediate is predicted by rapid freeze-quench Mössbauer, and its presence confirmed by EXAFS, and resonance Raman studies.[12, 31] These spectroscopic studies provided the first direct evidence of the involvement of an iron(IV) intermediate in reactions catalyzed by mononuclear non-heme iron enzymes.

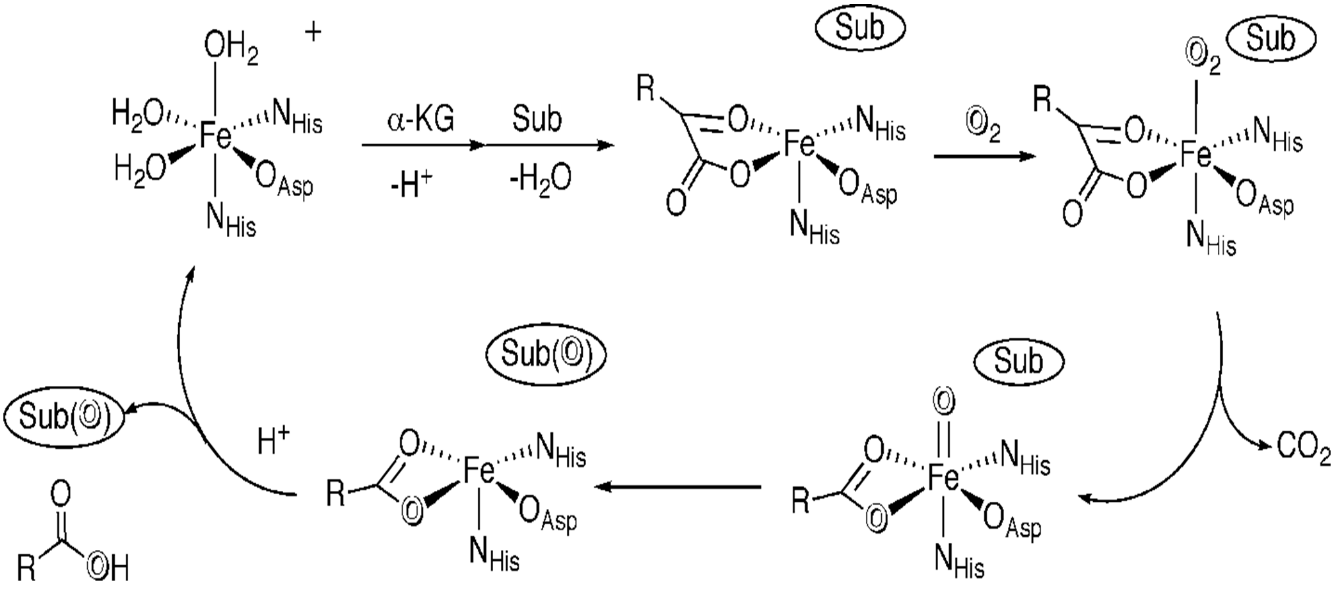

Scheme 1-7: Proposed mechanism of α-glutarate dependent enzyme TauD

From this point onwards in the reaction mechanism, the steps become diverse, depending on the substrates and the variation of oxidative transformations. It has been hypothesized, that the structural characteristics of the specific substrate determines the generation of the pivotal ferryl–oxo species.[32] In case of all the different enzymes across the entire subgroup, the Fe(IV)=O intermediates are generated in similar environment, still should be capable of different reactivity. In case of TauD, formation of the ferryl species is followed by abstraction of a hydrogen atom, followed by the coordinated hydroxyl radical recombining with the substrate radical to form the hydroxylated product. A large substrate deuterium kinetic isotope effect shown by the C-H bond in the Fe(IV)=O proves that it is indeed the crucial oxidative species involved in the mechanisms carried out by the enzymes of the subfamily.[13]

Pterin-dependent hydroxylases

This small family of aromatic amino acid hydroxylases (AAAH) requires the cofactor tetrahydrobiopterin (BH_4) for their reactivity.[33] This sub-family consists of enzymes such as, phenylalanine hydroxylase (PheH), tyrosine hydroxylase (TyrH), and tryptophan hydroxylase (TrpH). These enzymes, catalyze the hydroxylation of amino acids along with the simultaneous oxidation of the pterin cofactor. This group of enzymes has received considerable attention because of the reactions catalyzed by them have implications in various physiological and neurological diseases.[34]

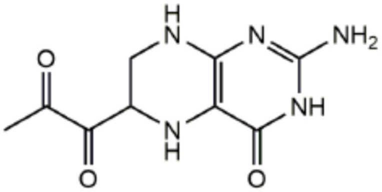

Figure 1-5: Structure of the Pterin co-factor(tetrahydrobiopterin)

TyrH and TrpH catalyze the synthesis of neurotransmitters catecholamine and serotonin respectively, and PheH catabolizes excess phenylalanine. From the crystal structure data of the enzymes, it has been shown, that they all feature a mononuclear non-heme iron active site, attached to the 2-His-1-carboxylate facial triad and three water molecules. The equatorial glutamate ligand binds bidentate in bacterial PheH as compared monodentate binding mode observed in human PheH.[33] The general reaction mechanism of TyrH and TrpH is depicted in the scheme below.

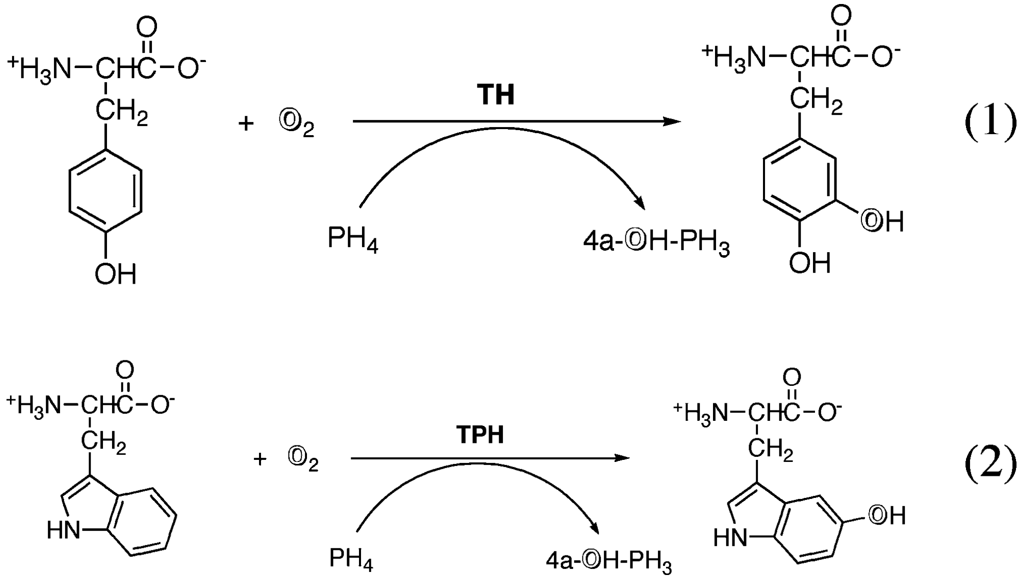

Scheme 1-8: Reactions catalyzed of TyrH and TrpH

Similar to the reaction mechanism of Rieske dependent enzymes, in this case neither the substrate nor the cofactor binds directly to the metal center. Though no intermediate has been isolated, the study of kinetic isotope effects on the reactions prove that except for the rate limiting step, the overall reaction mechanism is similar in all three enzymes. In case of PheH, once the pterin cofactor is displaced towards the iron, a significant conformational change take place.[35] The monodentate glutamate co-ordinates in a bidentate fashion, water molecules are displaced, facilitating the binding of oxygen at the active site. UV-visible and EPR spectroscopic studies using nitric oxide as a surrogate for oxygen binding indicate that upon binding, oxygen displaces the last remaining water molecule on the Fe-site to give rise to a five-coordinate species.[36]

These changes in conformation bring the pterin very close to the Fe center and the pterinperoxo–iron(II) species is formed (B), which undergoes a heterolytic cleavage to yield a highly reactive iron(IV)–oxo intermediate. Recently, a high-spin Fe(IV) intermediate has been reported for TyrH.[37] which was found by rapid-freeze quench Mössbauer spectroscopy, similar to the intermediates observed for the α-ketoglutarate-dependent enzymes. Kinetic experiments on the Fe(IV)–oxo, proves it to be the hydroxylating intermediate. At this stage of the mechanism electrophilic attack of the substrate results in a cationic intermediate. Kinetic isotope effects studies on the three enzymes in this family show partitioning of intermediates via branched pathways.[38] In the next step the Fe(IV)-oxo species oxidizes the substrate, and subsequent tautomerisation leads to product formation.

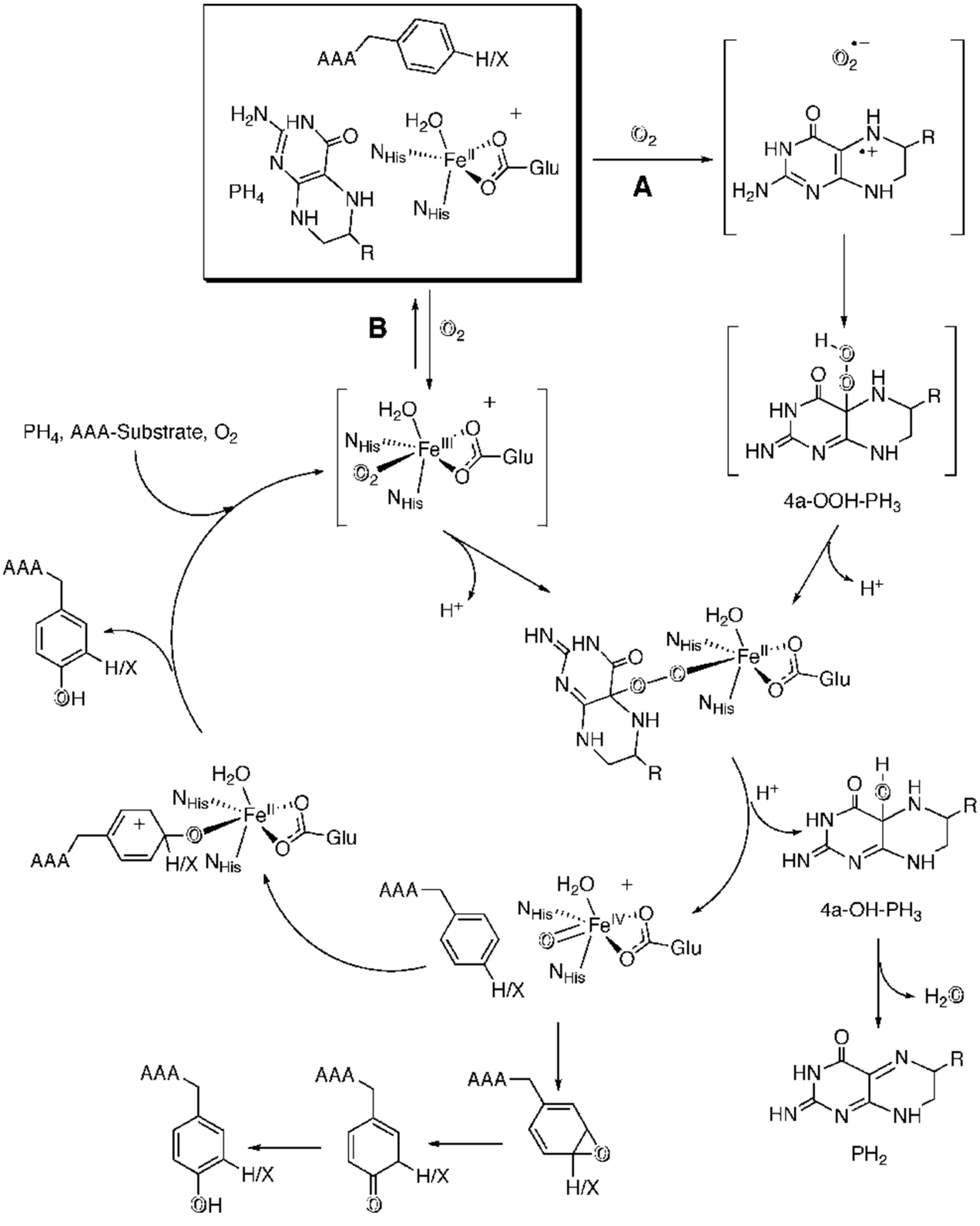

Scheme 1-9: Mechanism of Pterin-dependent Aromatic amine hydroxylase enzyme

IPNS

Biosynthesis of penicillin-type antibiotics in microorganisms first involves the formation of the bicyclic backbone of penicillin. Isopenicillin N- synthase (IPNS) is a non-heme iron oxidase which is crucial to the biosynthesis of β-lactam antibiotics. IPNS converts the tripeptide δ-(l-α-aminoadipoyl)-l-cysteinyl-d-valine (ACV) (**1**) to Isopenicillin N (**2**) while reducing molecular oxygen to water.[39] Despite showing high sequence homology to the α-ketoglutarate-dependent enzymes, IPNS does not need α-ketoglutarate as a cofactor for catalysis and does not incorporate oxygen into the product.[40]

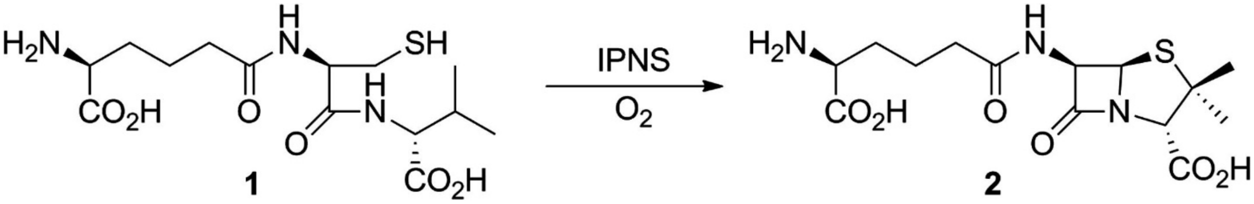

Scheme1-10: Reaction catalyzed by IPNS

In this case, the substrate provides all four electrons required for the reduction of molecular oxygen to water. Spectroscopic studies (EPR and Mössbauer) using Nitric oxide (NO) as a surrogate for O_2 binding have provided insight into the oxygen binding site and studies involving substrate analogues, for a proposed mechanism.[41]

The active site, in the resting state of the enzyme has a 2-His-1-carboxylate facial triad and remains attached to a glutamine residue. Upon substrate binding glutamine gets replaced from the active site along with two molecules of bound water. ACV binds to the active site via the deprotonation of the thiol group of cysteine group and is suggested to change the redox potential of the metal center helping in the binding of oxygen.[10]

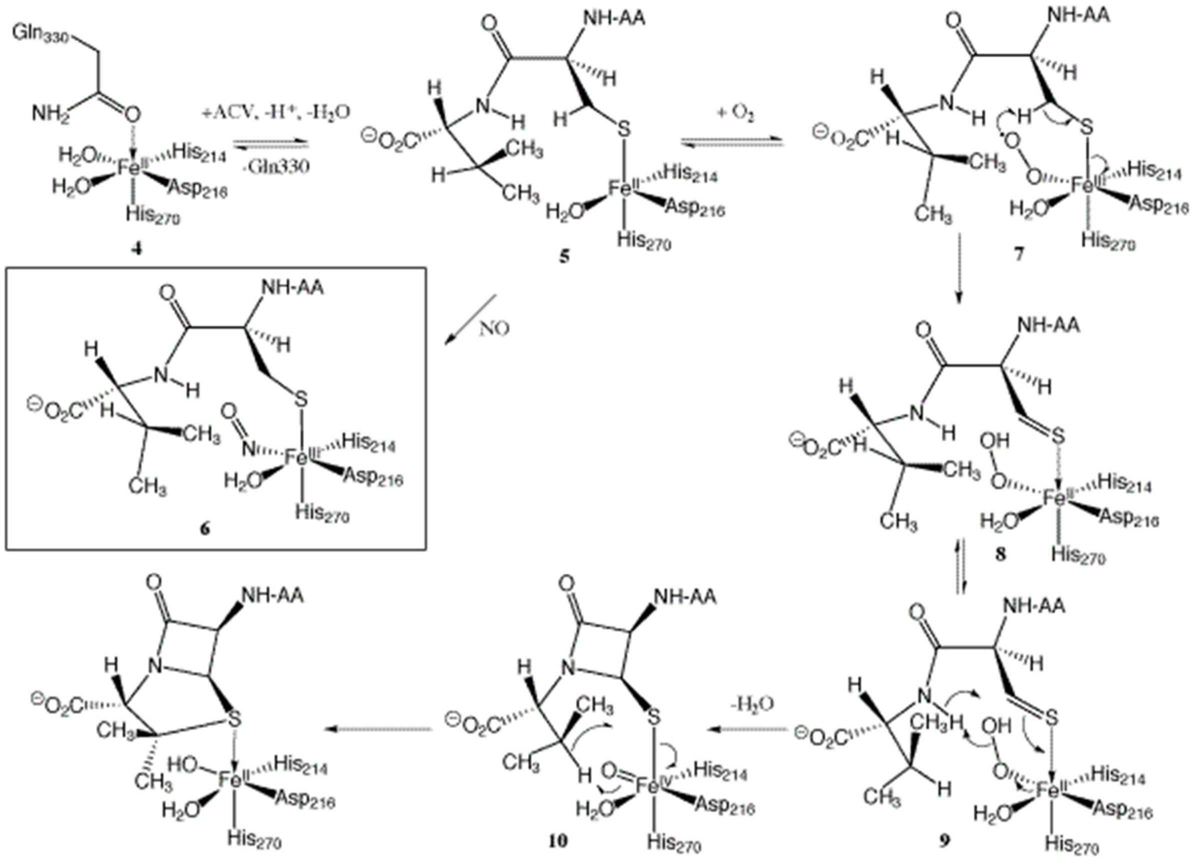

Scheme1-11: Proposed mechanism of Isopenicilin-N synthase

Spectroscopic and computational studies have shown, that the thiolate-bound substrate stabilizes the formation of the end-on superoxide, which in turn has the proper electronic configuration and orbital orientation for hydrogen abstraction. This step forms a Fe-hydroperoxide which in turn takes up a hydrogen from the adjacent nitrogen, causing the first oxidative ring closure product (β-lactam) and in the formation of a high-valent iron(IV)–oxo species. Formation of the thiazolidine ring or second ring closure occurs when the high valent species acts as the oxidant and mediates the second oxidative ring closure.[10]

ACCO

1-aminocyclopropane-1-carboxylic acid oxidase (ACCO) produces the plant hormone ethylene, which is involved in a variety of events such as germination, growth and development and fruit-ripening. Like IPNS, this enzyme also shows a high sequence homology to the α-ketoglutarate-dependent enzymes, but does not require α-ketoglutarate as cofactor for catalysis.

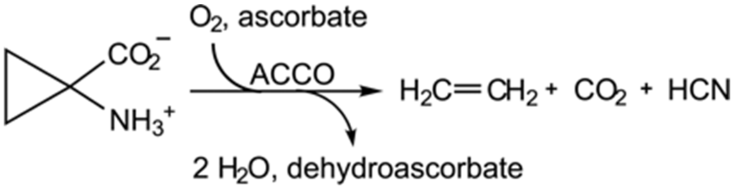

Scheme 1-12: Oxygen activation and ethylene formation reaction catalyzed out by ACCO

ACCO catalyzes the two-electron oxidation of the unusual amino acid 1-aminocyclopropane-1-carboxylic acid (acc) to produce ethylene while reducing oxygen to two water molecules. CO_2 and HCN are also formed as by-products of the reaction.[42] Due to inherent complexity of the system and lack of available structural information the mechanism of ACCO is not yet understood.[43] However, a proposed mechanism has been described through results of steady state kinetics and solvent kinetic isotope effect studies.[42]

The active site contains an Fe(II) metal with a of 2-His-1-carboxylate facial triad and three bound water molecules. In the presence of bicarbonate, an activator for catalysis, substrate (ACC) binds to the active site in a bidentate fashion through the carboxylate and amine group, concomitantly displacing two water molecules.

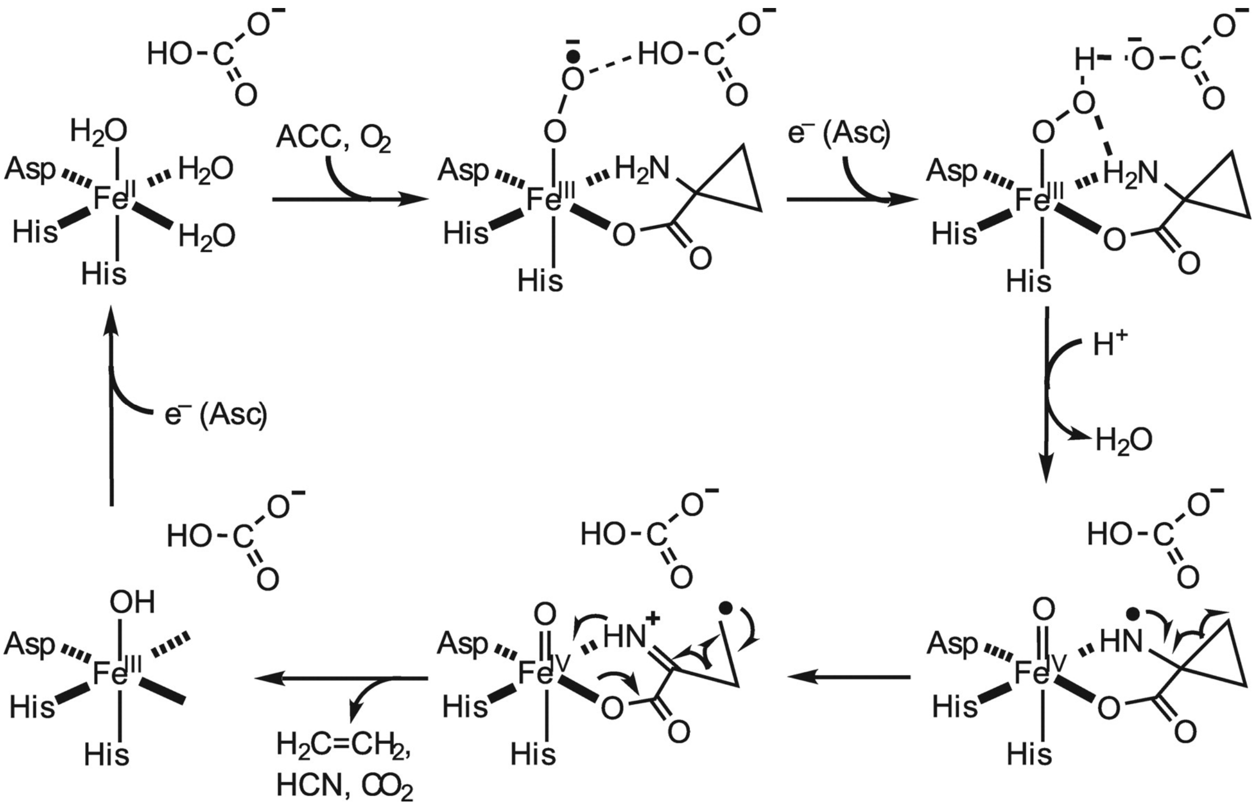

Scheme 1-13: Proposed mechanism of ethylene formation by ACCO

L-ascorbic acid is utilized as a 2-electron reductant in these reactions. Binding of ascorbate to a remote site initiates the conversion the Fe(II) site from a six- to five-coordinate system and facilitates oxygen binding by stimulating the loss of bicarbonate species. Kinetic isotope studies using $^{18}O_2$ shows that both the presence of ascorbate and bicarbonate are essential for catalysis. The latter acts as an activator, i.e. stimulates catalysis independent of its redox properties, and increases the k_{cat} and protects ACCO from oxidative deactivation.[11] The ENDOR studies prove the formation of a ternary ACCO–Fe(II)–acc–NO species, when NO was used as a surrogate for O_2 binding and also suggest that the orientation of substrate binding is dictated by the enzyme.[44]

It has been proposed that binding of oxygen to the metal center results in formation in a Fe(III)-superoxo species, electron transfer from ascorbate forms the Fe(III)-OOH species which extracts hydrogen from the amine group resulting in the formation of Fe(IV)=O species and a nitrogen based radical. After rapid radical rearrangement and hydroxyl radical transfer, the metal bound intermediate eventually goes through a cyclopropane ring cleavage and product formation, along with the formation of CO_2 and HCN as by-products.[43]

3His facial triad

Though the entire family of non-heme mononuclear Fe-enzyme active sites are dominated by versatile 2-His-1-carboxylate motifs, active site containing three histidine ligands have been described for enzymes that, bind redox inactive metals with filled d-shells, such as zinc. Carbonic anhydrase is a very well-studied example.[45] Among the group of non-heme iron enzymes, however, the 3-His centers have come into limelight only recently. There are only a three of those enzymes exist which have been crystallographically characterized, they are cysteine dioxygenase (CDO), gentisate 1,2 dioxygenase (GDO) and Diketone dioxygenase (Dke1).[46]

Dke1 is a dioxygenase enzyme, that cleaves carbon–carbon bonds in β-diketone substrates and incorporates one atom of molecular oxygen into each site of bond fission simultaneously.[47] The crystal structure solved from *Acinetobacter johnsonii* shows an inactive zinc-bound variant of the native enzyme that requires iron(II) for activity. The enzyme converts acetylacetone (2,4-pentanedione) into methylglyoxal and acetate. The active site structure of Dke1 shows significant similarity to that of CDOs structure except for the catalytically incompetent zinc metal attached via three histidine residues.

GDO catalyzes an oxygen-dependent ring opening reaction of gentisic acid into maleylpyruvate which is a crucial intermediate in metabolism of aromatic compounds in bacteria. The structure of

GDO from *Escherichia coli* revealed a bicupin fold which is a conserved β-barrel fold, characteristic feature of Fe-containing dioxygenases. Crystallographic data shows that GDO from *E. Coli*, in its resting state, has an Fe(II) in its active site, ligated by a 3-His triad leaving the three solvent-occupied sites available for interactions with substrates.[48]

Structural comparison of 3-His and 2-His-1-carboxylate centers of non-heme iron

Location of the metal center

The residues ligating the iron center in CDO and the other 3-His enzymes are buried deep inside in the very rigid core of the protein. In CDO, the active site is inside the protein core, enclosed in a solvent-filled environment at the distance of approximately 8 Å away from the surface.[49]

Conformation of the metal center

A remarkable degree of structural similarity is observed between 3-His and 2-His-1-carboxylate centers of non-heme iron containing proteins. When structures of CDO and TauD were superimposed, Both the core structure and the active-site residues align very well, except for few additional α-helices and β-sheets towards the surface of the protein in case of TauD.[11]

The spatial arrangement of ligands around the metal active site is quite similar in both enzymes despite histidine, an uncharged residue in case of CDO replaces negatively charged side chain of the aspartate residue in TauD. Structural overlay studies suggest, the both enzymes feature identical iron-binding geometries, with Asp-101 in TauD and His-88 in CDO adopting the same position in the protein.[50]

Iron is usually coordinated in an octahedral geometry with a 3-His facial arrangement and the three *cis*-sites are left open for the binding of substrate, co-substrate and oxygen. By comparing crystal structures data and evidence from X-ray absorption spectroscopy(XAS), it has been determined that an average co-ordination distance of 2.1 Å for the histidine side chains is determined for Fe(II) in 3-His motif in CDO[50] compared to average distances of 2.04 Å and 2.16 Å for aspartate/glutamate carboxylate O-atoms and histidine imidazole N ligands to ferrous iron in 2-His-1 carboxylate. So, it has shown that the co-ordination distance of carboxylate groups in non-heme Fe(II) centers is significantly shorter than that of imidazole groups along to the difference in overall net charge of 3-His iron sites compared with the 2-His-1-carboxylate counterparts, which presumably impact the structural and possibly functional difference between the two metal centers.

Cysteine dioxygenase

Thiol dioxygenase enzymes catalyzes the O_2-dependent conversion of sulfur containing thiol compounds to corresponding sulfinic acid derivatives. Till date, two mammalian thiol dioxygenases are known, cysteine dioxygenase, (CDO) and cysteamine dioxygenase (ADO), between these two CDO is more studied. The enzyme takes part in regulation cysteine in mammalian tissues by catalyzing the oxidative conversation of cysteine into cysteine sulfinic acid. The product of the CDO-catalyzed reaction is cysteinesulfinic acid, which is the precursor in hypotaurine and taurine biosynthesis.[51] It has been proposed that disruption in cysteine regulation gives rise to generation of reactive oxygen species in cell and imbalance in cysteine metabolism is been associated with various neurodegenerative disease. Hence, the enzyme is a potential drug target in therapies addressing Parkinson's or Alzheimer’s and other motor neuron diseases.[52]

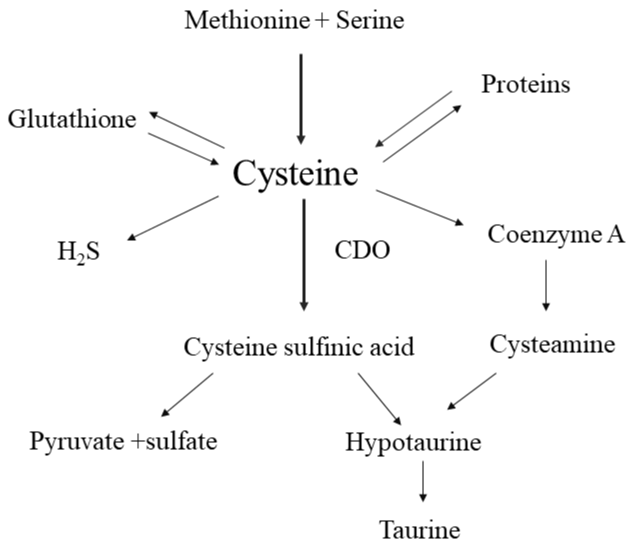

Scheme 1-14: Importance of cysteine in sulfur metabolism[51]

As the conversion cysteine to cysteine sulfinic acid is also a crucial step in production of taurine, irregularity in the pathway leads to taurine deficiency, which in turn leads to heart related issues.

CDO incorporates both O-atoms from molecular oxygen into the product without an external reductant; hence, classified as a dioxygenase.[53] CDO also exhibits high specificity for L-cysteine, showing little or no reactivity with d-cysteine, glutathione, L-cystine, or cysteamine.

From the X-ray data, it is known that in CDO, 3 histidine residues occupy a face of the octahedron leaving the other co-ordination sites for three water molecules. The enzyme follows an obligated ordered addition of substrate prior to oxygen. An Fe(III)-oxo intermediate species forms after the substrate and oxygen binds to the active site replacing the water molecules. Distal oxygen atom then attacks the sulfur atom and forms a Fe-O-O-S four membered persulfenate ring. At this point of reaction can diverge into two different pathways.

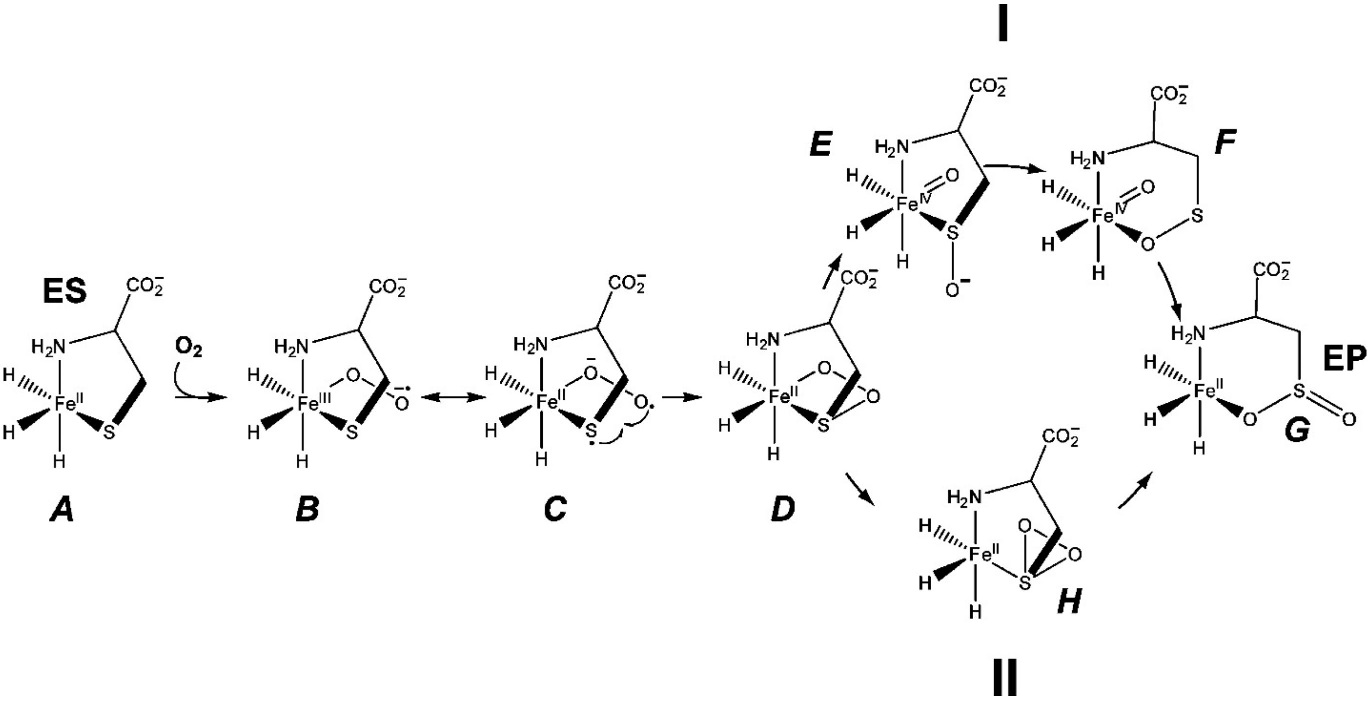

Scheme 1-15: Conversion of cysteine to cysteine sulfinic acid by CDO

A nucleophilic attack can take place of the distal oxygen can place on the sulfur giving rise to a cys-thiadioxirane ring, followed by a heterolytic cleavage of the O-O bond which leads to the formation of cysteine sulfinic acid.[54]

Considering the other pathway, homolytic cleavage of the O–O bond then occurs simultaneously with abstraction of a hydrogen atom from nearby the Tyr157 residue(ref). The electron in the O–O bond forms a bond with the iron center resulting in a highly reactive Fe(IV)= O. The phenoxide then removes a hydrogen atom from cysteine's thiol. At this stage, Fe(IV)=O species, being a powerful oxidizing agent, can attack the lone pair on cysteine's sulfur, forming a single S–O bond. The intermediate then under goes through reductive elimination to form CSA and the product is released from the active site.[54,53]

Crystal structure available for mammalian CDO shows quite a few interesting structural features. The enzyme has a β-barrel structure around its active site which is a characteristic feature of Cupin superfamily of enzymes. In the active site, traditional 2-His-1 carboxylate motif is replaced by a 3-His facial triad and moreover the carboxylate residue is replaced a cysteine residue (C93). This said residue participates in another interesting post-transcriptional modification involving a Tyrosine residue (Tyr 157) close to the metal active site.[55] These two residues form a covalent bond between themselves and they are both conserved among all mammalian CDOs.

3-mercaptopropionic acid dioxygenase (MDO)

Thiol dioxygenase (TDO) enzymes, like CDOs utilize a mononuclear ferrous iron active site to catalyze the O_2-dependent oxidation of sulfur-containing amino acid to sulfinic acid derivative. Sequence homology studies done comparing bacterial TDOs with bacterial CDO genes suggest that, this subclass of enzymes that lack the traditionally conserved Arg60 residue that has been proposed as a key outer-sphere interaction involved in substrate-stabilization in other CDO species.[56] In this subclass, the Arg60 residue is replaced by a Gln67 while the spatial orientation of all other residues remains conserved. This has led to 'bacterial CDOs' being classified into two categories 'Arg-type' or 'Gln-type', depending on the residue involved in stabilization. Previously, the bacterial TDO 3-mercaptopropionate dioxygenase (MDO) was found to have high sequence homology with the 'Gln-type' subclass of bacterial CDO enzymes and thus it was originally annotated as a CDO. Subsequent characterization of this enzyme by our group and independently by Jameson *et.al* verified that this enzyme is more appropriately defined 3-mercaptopropionic acid dioxygense.[100,110] This subclass of bacterial CDOs remain largely uncharacterized.[57]

Characterization of a bacterial TDO enzyme, MDO cloned from *Azotobacter vinelandii*, showed an annotated 'Gln-type' bacterial CDO to have activity with multiple substrates, including cysteine, cysteamine, and 3-mercaptopropionic acid(3mpa), with significant specificity towards 3mpa. Comparable turnover numbers across multiple substrates, gives rise to the question regarding the binding of substrate onto the active site. Experimental data suggest that the enzyme binds substrate monodentate and deviates from regular binding motif of mammalian CDO. Despite the promiscuous behavior, this enzyme shares quite a few structural and functional similarity with CDO. MDO has Fe(II) resting state, attached to 3-His facial triad and it follows obligate-ordered addition of substrate, prior to O_2 [58].

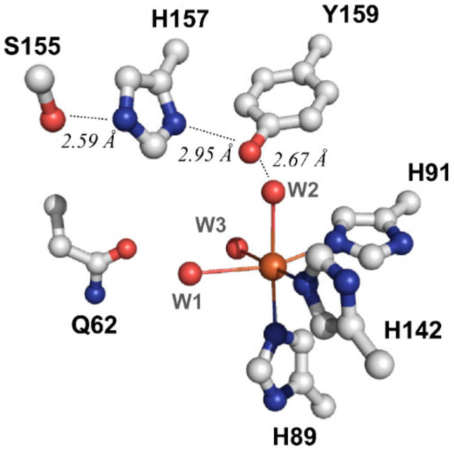

Figure 1-6: Crystal structure *Pseudomonas aeruginosa* 'Gln-type' MDO

Most of thiol dioxygenases have a conserved '*catalytic triad*' within the active site, consisting of three outer sphere Fe-coordination residues S155, H157 and Y159. With the notable exception of mammalian cysteamine (2-aminoethanethiol) dioxygenase (ADO), this '*catalytic triad*' is universally conserved across phylogenic domains. X-ray crystallographic studies clearly show a hydrogen bond network connecting the '*catalytic triad*' to the mononuclear iron site; however, its influence on substrate specificity and catalytic efficiency is poorly understood. In this work, kinetic and spectroscopic characterization of the MDO is presented, focusing specially on the role of the conserved catalytic triad on enzyme catalysis.

To explore the influence of the second-sphere residues on catalysis, the pH-dependent steady state kinetics for wild-type MDO and selected variants (H157N and Y159F) are compared using both

3mpa and L-cysteine (***cys***) as a substrate. Taken together with supporting EPR and Mössbauer spectroscopic studies, a mechanistic model is proposed in which the '*catalytic triad*' serves to gate proton delivery to the substrate-bound Fe-site. These studies suggest that the primary role of the '*catalytic triad*' is to neutralize the negative charge of the substrate-carboxylate group in the rate-limiting non-chemical steps leading up to O_2-activation.

Chapter 2

The 'Gln-type' thiol dioxygenase from *Azotobacter vinelandii* is a 3-mercaptopropionic acid dioxygenase

Cysteine dioxygenase (CDO) is a non-heme mononuclear iron enzyme that catalyzes the O_2-dependent oxidation of l-cysteine (***cys***) to produce cysteinesulfinic acid (***csa***).[59, 60] CDO and cysteamine (2-aminoethanethiol) dioxygenase (ADO) are the only known mammalian thiol dioxygenase enzymes. Among these, mammalian CDO is the best characterized.[57] [61, 62] This enzyme catalyzes the first committed step in ***cys*** catabolism and thus is central to sulfur metabolism and redox homeostasis. Enzymes involved in sulfur oxidation and transfer are increasingly being recognized as potential drug targets for the development of antimicrobials and therapies for cancer and inflammatory disease.[63, 64, 65, 66] Imbalances in ***cys*** metabolism have also been identified in a variety of neurological disorders (motor neuron disease, Parkinson's, and Alzheimer's).[51, 67, 68].These observations suggest a potential correlation among impaired sulfur metabolism, oxidative stress, and neurodegenerative disease.[69, 70]

As illustrated in Figure 1A, the active site coordination of the *Rattus norvegicus* CDO [Protein Data Bank (PDB) entry 4IEV][71] is comprised of iron ligated by the N_ε atoms of H86, H88, and H140, representing a 3-His variant on the classic 2-His-1-carboxylate facial triad observed in mononuclear non-heme iron enzymes.[53] Within the non-heme mononuclear iron family, only a handful of enzymes with a 3-His active site motif have been crystallographically characterized (CDO; diketone dioxygenase, Dke1;[50] and gentisate 1,2-dioxygenase, GDO.[72] Another unusual feature within the mature eukaryotic CDO active site is a post-translational modification 3.3 Å from the Fe center in which spatially adjacent Cys93 and Tyr157 residues are covalently cross-linked to produce a C93–Y157 pair. Among CDO enzymes identified, Y157 is conserved across phylogenic domains, whereas the C93–Y157 pair is unique to eukaryotes.[60, 5] It has been proposed that the C93–Y157 pair facilitates appropriate substrate orientation and stereoselectivity. However, the exact mechanism of C93–Y157 pair formation remains unresolved.

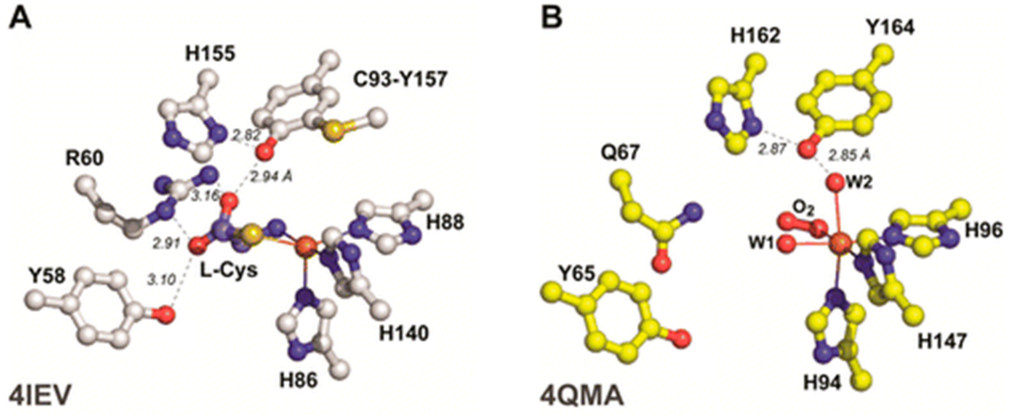

Figure 2- 1. Crystal structure of the substrate-bound *R. norvegicus* CDO active site (A, PDB entry 4IEV) as compared to the annotated "Gln-type" MDO isolated from *Ralstonia eutropha* (B, PDB entry 4QMA).(22) Solvent waters and a putative bound-oxygen are designated W1, W2, and O_2, respectively.

By contrast, all known bacterial CDO enzymes lack the Cys-Tyr post-translational modification. Sequence homology of annotated bacterial *cdo* genes suggests a subclass of enzymes, which lack the conserved R60 residue utilized for substrate stabilization. To illustrate, the crystal structure for the putative "Gln-type" CDO isolated from *Ralstonia eutropha* (PDB entry 4QMA) is shown in Figure 1B.[47] Of note, the 3-His facial triad motif is conserved; however, the outer-sphere Arg residue involved in electrostatic stabilization of the substrate is replaced with Gln (Q67). The spatial orientations of all other conserved residues (Figure 1A, H155, Y157, and Y58) within the active site remain invariant. For this reason, putative bacterial CDO enzymes have been subdivided as either "Arg-type" or "Gln-type" depending on which residue is involved in substrate stabilization.[48] In this context, the “Arg-type” bacterial CDO enzymes are most analogous to the mammalian enzymes.

Previously, a thiol dioxygenase [3-mercaptopropionate dioxygenase (MDO)] was isolated from the soil bacterium *Variovorax paradoxus* and characterized. Because 3-mercaptopropionic acid (***3mpa***) is widespread in coastal sediments, it has been proposed that this enzyme provides an advantage for soil bacteria to utilize this additional sulfur/carbon source in both assimilatory and catabolic metabolism.[56, 73] This enzyme shares a high degree of sequence identity (46–55%) with the “Gln-type” subset of annotated CDO enzymes, which thus calls into question the validity of this nomenclature.[56] Indeed, it has recently been proposed that this subclass of putative bacterial CDOs actually function as MDOs.[48] To date, the “Gln-type” enzymes remain largely uncharacterized. Therefore, this subset of enzymes offers a unique point of comparison to better understand the significance of the first- and outer-sphere coordination environment surrounding the Fe site and their impact on thiol dioxygenase chemistry.

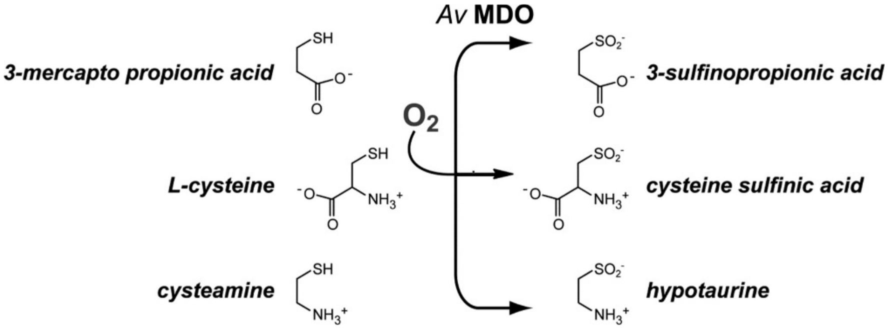

Scheme 2-1: Thiol Dioxygenase Reactions Catalyzed by *Av* MDO

In this work, the initial characterization of a putative “Gln-type” thiol dioxygenase enzyme cloned from the Gram-negative soil bacterium *Azotobacter vinelandii* is presented. For reasons that will be discussed later, this enzyme will be termed *Av* MDO. As indicated by Scheme 1, steady-state assays were performed using three potential substrates [3-mercaptopropionic acid (***3mpa***), l-cysteine (***cys***), and cysteamine (***ca***)]. Complementary X-band EPR experiments using nitric oxide (NO) as a surrogate for O_2 binding were also performed to investigate relative binding affinities for each substrate within the enzymatic active site. Collectively, these results suggest significant deviations in substrate coordination to the Fe site and enzymatic specificity of *Av* MDO as compared to the *Mus musculus* cysteine dioxygenase (*Mm* CDO).

Materials and Methods

Expression of *Av* MDO

The isopropyl β-d-1-thiogalactopyranoside (IPTG) inducible T7 vector (designated pRP42) was a generous gift from T. Larson (Department of Biochemistry, Virginia Tech, Blacksburg, VA). This vector expresses *Av* MDO with a C-terminal $(His)_6$ affinity tag and a recognition sequence for thrombin protease such that the affinity tag can be cleaved following purification. Sequence verification of *Av* MDO was performed by Sequetech (Mountain View, CA, http://sequetech.com/). The pRP42 vector was transformed into competent BL21(DE3) *Escherichia coli* cells (Novagen catalog no. 70236-4) by heat shock and plated for overnight growth at 37 °C on LB agar containing 100 mg/L ampicillin (Amp). The following day, a single colony was selected for growth in liquid LB (Amp) medium for training on antibiotic prior to inoculation of a 10 L BF-110 fermentor (New Brunswick Scientific) at 37 °C. Cell growth was followed by optical density at 600 nm (OD_{600}). Cells were induced by addition of 1.0 mM IPTG, 20 g of casamino acids, and 40 μM ferrous sulfate at an OD_{600} of ~4. At the time of induction, the temperature of the bioreactor was decreased from 37 to 25 °C and agitation was set to maintain an O_2 concentration of 20% relative to air-saturated medium. After 4 h, the cells were harvested by centrifugation (Beckman-Coulter Avanti J-E, JA 10.5 rotor) at 18600*g* for 15 min, and the paste was stored at −80 °C. Confirmation of *Av* MDO expression was performed by sodium dodecyl sulfate–polyacrylamide gel electrophoresis (SDS–PAGE) of lysed cells before and after induction.

Enzyme Purification

In a typical preparation, 20 g of frozen cell paste was thawed on ice by addition of 30 mL of HEPES buffer [20 mM HEPES and 50 mM NaCl (pH 8.0)]. To this suspension were added lysozyme, deoxyribonuclease, and ribonuclease I to a final concentration of 10 μg/mL each, and they were allowed to react for 30 min. Following enzymatic digestion, the suspension was sonicated for a 15 s on/off pulse cycle for a total time of 10 min. Insoluble cell debris was removed by centrifugation for 1 h at 4 °C (48000*g*). The cell free extract was loaded onto a DEAE fast flow anion exchange column pre-equilibrated in 20 mM HEPES and 50 mM NaCl (pH 8.0). The column was washed with 3 column volumes of the HEPES buffer prior to elution with a NaCl gradient (from 50 to 350 mM) at pH 8.0. Fractions (10 mL) were collected overnight and pooled on the basis of enzymatic activity with ***3mpa*** and/or ***cys*** as described elsewhere.[74] SDS–PAGE was also used to verify the presence of the recombinant protein (~23 kDa) within each fraction. Broad range protein molecular weight markers utilized in SDS–PAGE experiments were purchased from Promega (Madison, WI, catalog no. V8491). The pooled fractions were concentrated to approximately 5–10 mL using an Amicon stir cell equipped with a YM-10 ultrafiltration membrane. Thrombin protease (Biopharma Laboratories) was added to cleave the C-terminal His tag from *Av* MDO. In a typical reaction, ~0.3 molar equivalent of thrombin per *Av* MDO (based on UV–visible absorbance at 280 nm) was added to batches of purified protein for overnight cleavage at 4 °C in HEPES buffer. The remaining thrombin and free $(His)_6$ tag were removed from *Av* MDO by size exclusion chromatography using a Sephacryl S100 column.

Iron Analysis

For all batches of *Av* MDO used in these experiments, spectrophotometric determination of ferrous and ferric iron content was conducted using 2,4,6-tripyridyl-*s*-triazine (TPTZ) according to previously published methods.[74 ,57] Briefly, a 200 μL aliquot of ~100 μM enzyme was hydrolyzed in a microfuge tube by addition of 250 μL of 2 N HCl, 250 μL of 20% (w/v) trichloroacetic acid, and 300 μL of Milli-Q H_2O. The sample was heated to 95 °C for 15 min before centrifugation to pellet precipitated protein. Following centrifugation, 750 μL of the sample was added to 300 μL of 1.0 mM TPTZ, 3.0 M acetic acid, and 0.4 mM hydroxyl amine (NH_2OH) (pH 6.0). The resulting solution was allowed to equilibrate for 30 min at ambient temperature to ensure complete reduction of all ferric iron to the ferrous oxidation state. The total iron concentration was measured spectrophotometrically at 596 nm (ε = 22.6 mM^{-1} cm^{-1}).[57] The amount of ferrous iron present in purified *Av* MDO was determined as described above, except in the absence of a reductant (NH_2OH). The amount of ferric iron within samples was determined by difference. For the sake of clarity, the concentrations reported in enzymatic assays reflect the concentration of ferrous iron within samples of *Av* MDO (Fe^{II}-MDO). Protein content was determined by the Bio-Rad protein assay.

Enzyme Assays

3-Sulfinopropionic acid (***3spa***), cysteinesulfinic acid (***csa***), and hypotaurine (***ht***) were assayed using the HPLC method described previously.[47, 74] Instrumental conditions were as follows: column, Phenomenex C18 (100 mm × 4.6 mm); mobile phase, 20 mM sodium acetate, 0.6% methanol, and 1% heptafluorobutyric acid (pH 2.0). Analytes were detected spectrophotometrically at 218 nm. Reaction mixtures (1 mL) were prepared in a buffered solution at the desired pH to obtain a final concentration from 0.1 to 10 mM ***3mpa*** (0.1–60 mM ***cys*** and ***ca***). The composition of reaction buffers for all pH profile experiments consisted of 20 mM Good's buffer and 50 mM NaCl. 2-(*N*-Morpholino)ethanesulfonic acid (MES) was used to buffer reactions over the pH range of 5.5–6.7, and 2-[4-(2-hydroxyethyl)piperazin-1-yl]ethanesulfonic acid (HEPES) was used to buffer reactions over the pH range of 6.8–8.4. 2-(Cyclohexylamino) ethanesulfonic acid (CHES) was used to buffer reactions over the pH range of 8.5–10. Each reaction was initiated by addition of 0.5 μM *Av* MDO at 25 ± 2 °C. Sample aliquots (250 μL) were removed from the reaction vial at selected time points (1, 2, and 3 min) and reactions quenched by addition of 10 μL of 1 N HCl (final pH of 2.0) followed by spin filtration [0.22 μm cellulose acetate membrane; Corning, Spin-X (0.22 μM)] prior to HPLC analysis. The product concentration was determined by comparison to calibration curves as described elsewhere.[47, 74] The rate of dioxygen consumption in activity assays was determined polarographically using a standard Clark electrode (Hansatech Instruments, Norfolk, England) in a jacketed 2.5 mL cell. Calibration of the O_2 electrode is described in detail elsewhere.[58, 75] As with HPLC assays, all reactions were initiated by addition of 1.0 μM *Av* MDO under identical buffer conditions as described for HPLC assays. Reaction temperatures were maintained at 25 ± 2 °C by a circulating water bath (ThermoFlex 900, Thermo Scientific).

All reaction mixtures used in steady-state experiments in which the O_2 content was varied were prepared anaerobically described below (Anaerobic Manipulations). The desired oxygen concentration for each reaction was prepared by mixing anaerobic reaction mixtures with an O_2-saturated buffer prepared by sparging O_2 gas into the reaction buffer for 20 min under constant stirring at 25 °C. Reaction mixtures (2 mL) were prepared with final O_2 concentrations ranging from 50 to 400 μM and a fixed, saturating substrate concentration.

Synthesis of 3-Sulfinopropionic Acid

3-Sulfinopropionic acid (***3spa***) was prepared by acid saponification of the commercially available methyl ester [sodium 1-methyl 3-sulfinopropanoate (Sigma-Aldrich catalog no. 778168)]. Briefly, the compound was dissolved in a solution of 12% (v/v) acetic acid in 1 N HCl and refluxed overnight at 120 °C. The resulting ***3spa*** was dried on a rotovap and rinsed with cold water to remove acid and/or salt. Mass spectrometry analysis of the ***3mpa*** product was conducted at the Shimadzu Center for Advanced Analytical Chemistry of The University of Texas at Arlington.

Data Analysis

Steady-state kinetic parameters were determined by fitting data to the Michaelis–Menten equation using SigmaPlot version 11.0 (Systat Software Inc., Chicago, IL). From this analysis, both the kinetic parameters (k_{cat} and K_M) and the error associated with each value were obtained by nonlinear regression. For reactions in which the pH dependencies of steady-state kinetic parameters (k_{cat} or k_{cat}/K_M) are "bell-shaped" in that they decrease at both low and high pH values, data were fit to equation 1.[76, 77, 78]

Equation **1**.
$$\log Y = log\left(\frac{C}{\left(1+\frac{[H]}{K_1}\right)\left(1+\frac{K_2}{[H]}\right)}\right)$$

(1) where Y is defined as either k_{cat} or k_{cat}/K_M. The variables [H], K_1, and K_2 represent the hydrogen ion concentration and the two observable dissociation constants for ionizable groups involved in catalysis, respectively. This expression is scaled by a constant scalar quantity (C) that represents the maximal kinetic rate (k_{cat} or k_{cat}/K_M). Alternatively, k_{cat}– or k_{cat}/K_M–pH profiles approaching limiting values (Y_L and Y_H) at low and high pH were fit to equation 2.

Equation **2**.
$$\log Y = log\left(\frac{Y_L+Y_H\cdot\frac{K_1}{[H]}}{1+\frac{K_1}{[H]}}\right)$$

(2)Finally, for results in which k_{cat}– or k_{cat}/K_M–pH profiles decreased only at low pH, the data were fit to equation 3.[75 55, 77] Similar to equation 1, this expression is scaled by a constant scalar quantity (C) that represents the maximal kinetic rate (k_{cat} or k_{cat}/K_M). The error associated with each parameter (k_{cat}, k_{cat}/K_M, pK_{a1}, and pK_{a2}) determined from fits to equations 1–3 is reported in Table 1.

Equation 3: $\log Y = \log\left(\frac{C}{1+\frac{[H]}{K_1}}\right)$

Anaerobic Manipulations

All anaerobic samples were prepared in a glovebox (Coy Laboratory Products Inc., Grass City, MI) with the O_2 concentration maintained below 1 ppm. Solutions were degassed on a Schlenk line prior to being transferred into the anaerobic chamber. Analytical grade argon was passed through a copper catalyst (Kontes, Vineland, NJ) to remove trace O_2 impurities and then sparged through distilled water to hydrate the gas.

Physical Methods

All UV–visible measurements were taken on an Agilent (Santa Clara, CA) 8453 photodiode array spectrometer using ES Quartz cuvettes (NSG Precision Cells, Farmingdale, NY). X-Band (9 GHz) EPR spectra were recorded on a Bruker (Billerica, MA) EMX Plus spectrometer equipped with a bimodal resonator (Bruker model 4116DM). Low-temperature measurements were taken using an Oxford ESR900 cryostat and an Oxford ITC 503 temperature controller. A modulation frequency of 100 kHz was used for all EPR spectra. All experimental data used for spin quantification were collected under non- saturating conditions.

Analysis of the EPR spectra utilized the general spin Hamiltonian equation (4)

Equation 4 $$\hat{H} = \boldsymbol{D}\left(\hat{S}_Z^2 - \frac{S(S+1)}{3}\right) + \boldsymbol{E}\left(\hat{S}_X^2 + \hat{S}_Y^2\right) + \beta \mathbf{B} \cdot \boldsymbol{g} \cdot \boldsymbol{S}$$

where D and E are the axial and rhombic zero-field splitting (zfs) parameters, respectively, and $\mathbf{g}$ is the $\mathbf{g}$ tensor.[79] EPR spectra were simulated and quantified using Spin Count (version 5.4.5414.16762), written by M. P. Hendrich at Carnegie Mellon University (Pittsburgh, PA). The simulations were generated with consideration of all intensity factors, both theoretical and experimental, to allow for determination of species concentration. The only unknown factor relating the spin concentration to signal intensity was an instrumental factor that is specific to the microwave detection system. However, this was determined by a spin standard, Cu(EDTA), prepared from a copper atomic absorption standard solution purchased from Sigma-Aldrich.

Nitric Oxide Additions

Prior to addition of substrate and NO, the initial *Av* MDO concentration used for EPR experiments was assayed at ~550 μM in ferrous iron. Multiple EPR samples were prepared by varying the ratio of the substrate (***3mpa***, ***cys***, and ***ca***) to ferrous iron from 0.5 to 25 molar equiv. However, in all instances, the intensity of $\{FeNO\}^7$ signals observed by EPR was adversely affected at substrate concentrations exceeding 5 molar equiv. Therefore, all EPR samples presented utilize stoichiometric substrate per ferrous iron. Following addition of substrate, samples were allowed to equilibrate anaerobically in a glovebox for 10 min prior to being frozen for analysis. Stoichiometric additions of nitric oxide were made by addition of a NO-saturated buffer as previously described.[74] Following addition of NO and substrate solutions, the final concentration of *Av* MDO in EPR samples is 385 μM.

Results

Purification of *Av* MDO

The putative “Gln-type” enzyme from *A. vinelandii* (*Av* MDO) was purified and assayed for iron content as described in Materials and Methods. As indicated by the SDS–PAGE shown in Figure S1 of the Supporting Information, the IPTG inducible *Av* MDO protein [lanes 2 (−) and 3 (+)] exhibits an apparent molecular mass of ∼23 kDa. This is consistent with the value expected from the amino acid sequence (22696.51 Da). Fractions of *Av* MDO were pooled on the basis of enzymatic activity determined by thin layer chromatography [80] and SDS–PAGE. Pooled fractions were treated with thrombin overnight at 4 °C to remove the C-terminal $(His)_6$ tag (Figure S1, lane 5). Unlike its mammalian counterpart, *Av* MDO lacks the C93–Y157 post-transcriptional modification, and thus, a single band is observed for the isolated enzyme. The stoichiometry of iron per *Av* MDO protein was determined by TPTZ, Bradford assay, and UV–visible spectroscopy as described elsewhere.[74] In multiple enzyme preparations, the average iron content was 0.8 ± 0.1 mol of iron per *Av* MDO. Nearly all (83 ± 16%) of the iron observed in samples of *Av* MDO is in the catalytically relevant Fe(II) state when assayed immediately following purification. However, the Fe(II) site within *Av* MDO is more susceptible to autoxidation than that in *Mm* CDO.[74] The fraction of Fe(III) increases significantly with handling; thus, all assays described below were conducted immediately following purification.

Steady-State Kinetics of *Av* MDO-Catalyzed Reactions

Because the native substrate for the putative “Gln-type” enzyme is in question, the steady-state kinetics for *Av* MDO was measured using three likely substrates [3-mercaptopropionic acid (***3mpa***), l-cysteine (***cys***), and cysteamine (***ca***)]. For all steady-state assays, the observed initial rate was normalized by the concentration of ferrous iron in purified *Av* MDO (v_0/[E]). The results obtained for the two best substrates (***3mpa*** and ***cys***) are illustrated in Figure 2. For dioxygenase reactions, oxygen is a cosubstrate; therefore, in addition to measuring product formation (***3spa*** and ***csa***) by HPLC, the rate of O_2 consumption was measured using a calibrated Clarke-type O_2 electrode. These methods are described in detail in Materials and Methods and elsewhere.[58, 75] For each substrate, k_{cat}, K_M, and the errors associated with each value were obtained by fitting the data to the standard Michaelis–Menten equation at 25 ± 2 °C and pH 8.0.

As illustrated in Figure 2A, in assays using ***3mpa*** as a substrate, the values of k_{cat} (0.94 ± 0.04 s^{-1}) and K_M (13 ± 5 μM) were determined by measuring the initial rate of O_2 consumption (□). From these values, the catalytic efficiency (k_{cat}/K_M) of this enzyme is 72000 ± 9200 M^{-1} s^{-1}. Diode array detection of ***3spa*** is less sensitive than the Clarke electrode. Therefore, HPLC detection of the product is challenging in assays in which the substrate concentration is near or below the K_M value of *Av* MDO. Nevertheless, at a saturating substrate concentration, the maximal velocity determined from the initial rate of ***3spa*** formation ($k_{cat} = 0.96 \pm 0.06$ s^{-1}) is essentially stoichiometric with that obtained from the initial rate of O_2 consumption [Figure 2A (■)]. As k_{cat} represents the zero-order limit of an enzymatic reaction, the coupling efficiency can be obtained from the ratio of the k_{cat} as measured from product formation divided by the k_{cat} obtained from O_2 consumption. Therefore, in reactions using ***3mpa***, *Av* MDO is essentially fully coupled (102 ± 8%).

In reactions utilizing ***cys*** as a substrate (Figure 2B), k_{cat} and K_M values obtained from the initial rate of O_2 consumption (○) were determined to be 1.25 ± 0.04 s^{-1} and 8.6 ± 0.8 mM, respectively. Therefore, the k_{cat}/K_M for this enzyme is 150 ± 14 M^{-1} s^{-1} as determined by the rate of O_2 consumption. By comparison, for the initial rate for ***csa*** formation (●), k_{cat} and K_M were determined to be 1.21 ± 0.1 s^{-1} and 11.4 ± 0.9 mM, respectively ($k_{cat}/K_M = 110 \pm 20$ M^{-1} s^{-1}). Thus, reactions performed at saturating ***cys*** concentrations also exhibit stoichiometric (97 ± 6%) coupling efficiency.

Steady-state assays were also performed on *Av* MDO using cysteamine [2-aminoethanethiol (***ca***)] and mercaptosuccinic acid. As shown in Table 1, steady-state assays using ***ca*** as a substrate exhibit significantly lower k_{cat} (0.29 ± 0.08 s^{-1}) and k_{cat}/K_M values (11 ± 2 M^{-1} s^{-1}) relative to those of either ***3mpa*** or ***cys***. Furthermore, the coupling efficiency (40 ± 9%) of this reaction is significantly decreased relative to those of ***3mpa*** and ***cys***. No activity was observed with mercaptosuccinic acid. As previously mentioned, O_2 is a cosubstrate for this enzyme; therefore, it is important to verify that the atmospheric oxygen concentrations utilized in these experiments (∼230 μM) are sufficient to saturate steady-state kinetics for each substrate. To confirm this, the initial rate of enzymatic reactions was measured at fixed and saturating substrate concentrations [***3mpa*** (300 μM), ***cys*** (60 mM), and ***ca*** (60 mM)] while the O_2 concentration was varied by serial dilution at pH 8.0 and 25 °C. As shown in Figure S2 of the Supporting Information, no decrease was apparent in the initial rate at oxygen concentrations between 50 and 400 μM. Indeed, full O_2 saturation is observed for all substrates evaluated, even at the lowest O_2 concentration utilized (50 μM). This is consistent with previous reports for *Mm* CDO in reactions utilizing ***cys***.(28) This indicates that the apparent K_M^{02} is significantly lower (∼10 times) than the lowest value of oxygen utilized in these experiments. Thus, despite not being able to directly measure the apparent K_M^{02} for this enzyme, these results confirm that the atmospheric O_2 concentration is sufficient to fully saturate steady-state kinetics for all substrates utilized here.[75, 81]

Product formation (***3spa*** and ***csa***) was verified using multiple-reaction monitoring (MRM) as described in Materials and Methods. In these experiments, the $[M + H]^+$ molecular ion (***3spa***, *m*/*z* 138; ***csa***, *m*/*z* 154) was selected for secondary fragmentation. The optimized MRM method was used to verify sulfinic acid product by direct injection of enzymatic assays. The data obtained were then compared to those of standards to confirm product identity. In addition to the *m*/*z* 138 parent $[M + H]^+$ ion, three additional ions are observed at *m*/*z* 28, 65, and 92 for the ***3spa*** standard. The fragmentation pattern and relative intensities observed in enzymatic reactions (Figure 2, panel A2) exactly match those observed for the ***3spa*** standard (panel A1). Similarly, the ***csa*** molecular ion $[M + H]^+$ (*m*/*z* 154), matching fragmentation pattern, and relative intensities observed upon direct injection of enzymatic assays (*m*/*z* 44, 74, and 108) shown in panels B1 and B2 of Figure 2 confirm formation of the ***csa*** product.[60]

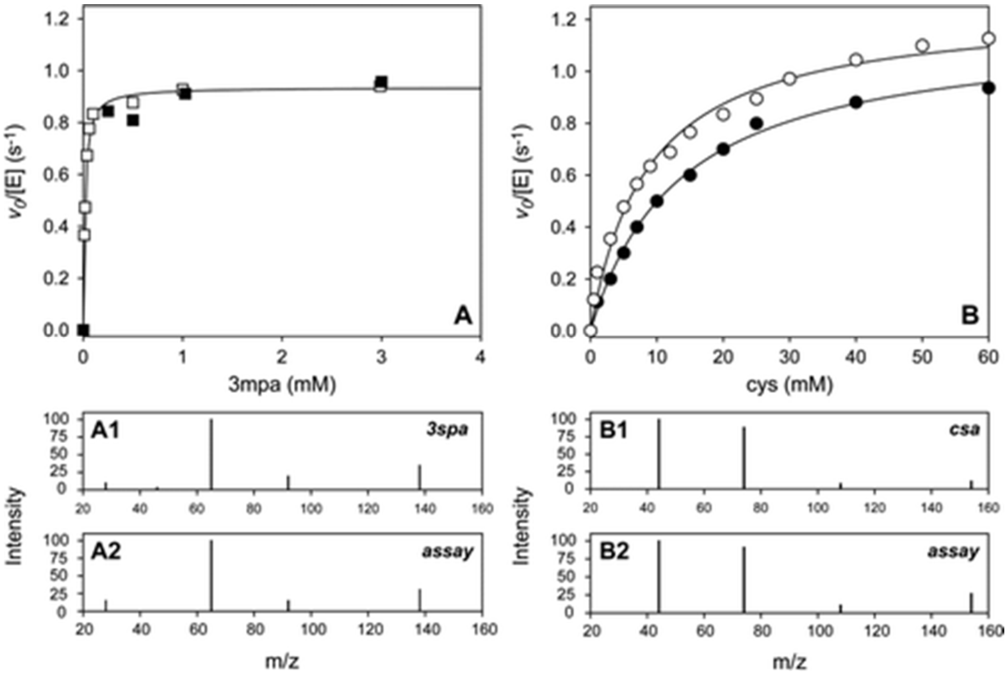

Figure 2-2. Steady-state kinetics of *Av* MDO-catalyzed ***3spa*** (A, squares) and ***csa*** (B, circle) formation. In both panels, the maximal velocities (k_{cat}) for O_2 consumption (white) and product formation (black) were determined by the best fit to the standard Michaelis–Menten equation to obtain the coupling efficiency. Assay conditions: 25 °C and pH 8.0. LC–MS/MS of ***3spa*** (A) and

csa (B) MRM transitions for standards (1, top) as compared to the direct injection of enzymatic reactions (2, bottom).

Table 2-1. Comparison of Steady-State Kinetic Parameters Determined for the Thiol Dioxygenases, *Av* MDO and *Mm* CDO

enzyme	**kinetic parameter**	***cys***	***3mpa***	***ca***	**ref**
Av MDO (25 °C)	k_{cat} (s^{-1})	1.2 ± 0.1	1.0 ± 0.1	0.29 ± 0.08	this study
	K_M (mM)	11.4 ± 0.9	0.013 ± 0.005	26 ± 5	
	k_{cat}/K_M (M^{-1} s^{-1})	110 ± 20	72000 ± 9200	11 ± 2	
	coupling (%)	92 ± 6	102 ± 6	not determined	
	log(k_{cat})				
	pK_{a1}	5.6 ± 0.1	6.9 ± 0.1	6.6 ± 0.2	
	pK_{a2}	9.9 ± 0.1	9.5 ± 0.1	–	
	log(k_{cat}/K_M)				
	pK_{a1}	5.1 ± 0.1	7.6 ± 0.2	6.0 ± 0.1	
	pK_{a2}	9.7 ± 0.1	8.2 ± 0.2	9.9 ± 0.1	
Mm CDO (20 °C)	k_{cat} (s^{-1})	0.6 ± 0.1	not detected	not observed[a]	19, 28
	K_M (mM)	2.3 ± 0.3	–	not observed[a]	
	k_{cat}/K_M (M^{-1} s^{-1})	260 ± 30	–	<0.01	
	coupling (%)	76 ± 7	–	<1	
	log(k_{cat})				
	pK_{a1}	7.42 ± 0.1	–	–	
	pK_{a2}	10.30 ± 0.08	–	–	
	log(k_{cat}/K_M)				
	pK_{a1}	8.0 ± 0.2	–	–	
	pK_{a2}	not observed	–	–	

Full substrate saturation was not observed for *Mm* CDO steady-state assays at ***ca*** concentrations ranging from 25 to 100mM. As a result, k_{cat} and K_M values could not be directly obtained. However, the pseudo-second-order rate constant (approximately k_{cat}/K_M) was obtained from the best fit to the linear portion of the saturation curve.[60]

pH Effects

Additional mechanistic insight into ionizable groups involved in catalysis can be obtained from the pH dependence on both k_{cat} and k_{cat}/K_M. The influence of pH on *Av* MDO catalysis was measured for all substrates over the accessible pH range of the enzyme (5–10). Figure 3 illustrates the log(k_{cat})–pH (A) and log(k_{cat}/K_M)–pH profiles (B) obtained from the initial rate data of *Av* MDO reactions using ***3mpa*** as a substrate. Each point within these data sets (Figure 3A,B) was obtained by fitting the steady-state kinetic results observed at a fixed pH value to the standard Michaelis–Menten equation. The error in each kinetic parameter obtained (k_{cat} and k_{cat}/K_M) from these fits is graphically indicated in Figure 3. As with the steady-state curve shown in Figure 2, full coupling was observed over the entire pH range assayed.

In reactions using ***3mpa***, both pH profiles (k_{cat}–pH and k_{cat}/K_M–pH) exhibit a skewed "bell-shaped" curve with two apparent pK_a values. Within the acidic branch of this profile (pH 5–8), both k_{cat} and k_{cat}/K_M follow sigmoidal behavior with limiting values at high and low pH. While the data within the acidic branch of this pH profile can be fit to eq 2 (dashed line), the pK_{a1} value obtained is shifted more basic because of the presence of a second ionizable group (pK_{a2}). Beyond pH 8.25, both k_{cat} and k_{cat}/K_M data decrease. Given that pK_{a1} and pK_{a2} are fairly close together, data within the inverted bell curve region (pH 7–10) were fit using equation 1 to obtain the apparent pK_a values (and error) for each ionizable group.[82] Kinetic data obtained from pH 5 to 6.5 were omitted from these fits. From this analysis, two apparent pK_a values were obtained (6.91 ± 0.10 and 9.52 ± 0.06) from the k_{cat}–pH profile in ***3mpa*** reactions. The maximal k_{cat} value obtained from fitting was 0.98 ± 0.06 s^{-1} at pH 8.25. Using the same fitting procedure, two pK_a values were obtained from the k_{cat}/K_M–pH data (7.6 ± 0.2 and 8.2 ± 0.2). Here, the maximal value of k_{cat}/K_M (72000 ± 9200 M^{-1} s^{-1}) was observed at pH 7.9.

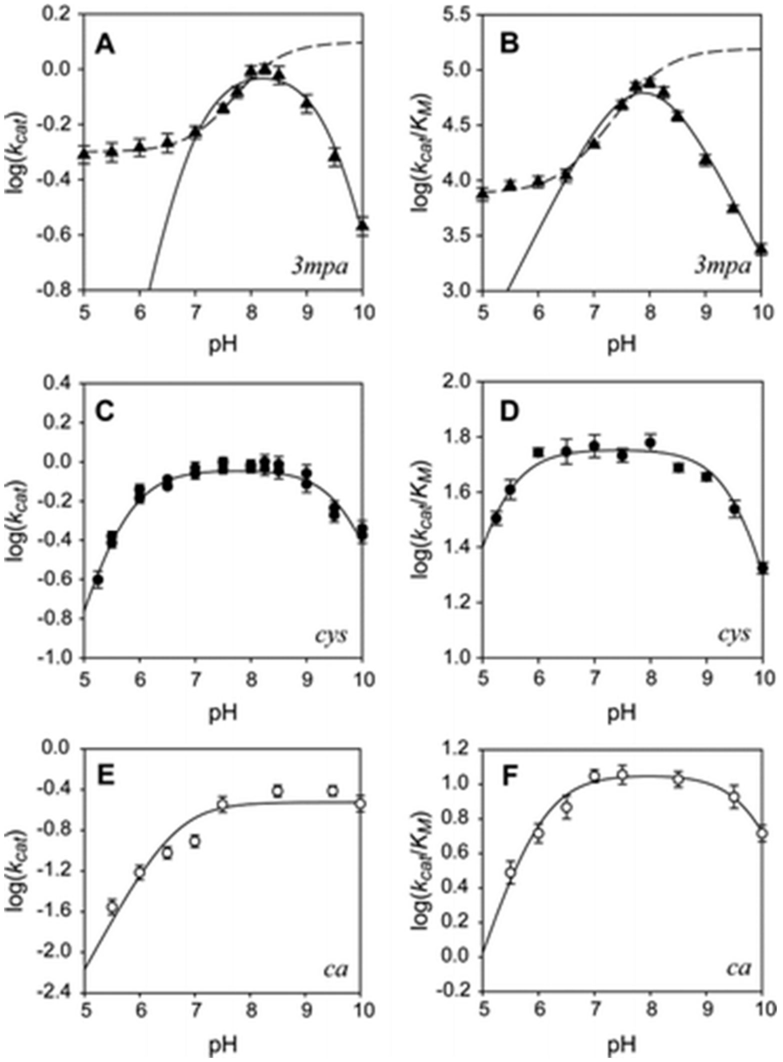

Figure 2-3. pH dependence of k_{cat} and $k_{\mathrm{cat}}/K_{\mathrm{M}}$ for *Av* MDO-catalyzed reactions with ***3mpa*** (A and B), ***cys*** (C and D), and ***ca*** (E and F) at 25 °C. The error indicated graphically is obtained by fitting kinetic results obtined at each pH value to the standard Michaelis–Menten equation. The pK_{a} values obtained from k_{cat}–pH and $k_{\mathrm{cat}}/K_{\mathrm{M}}$–pH profiles were determined by a best fit of pH-dependent kinetic results to eqs 1–3. A summary of steady-state kinetic parameters determined for *Av* MDO and *Mm* CDO is provided in Table 1.

The pH profiles for *Av* MDO in reactions using ***cys*** as a substrate were also determined for comparison. As illustrated in Figure 3 (panels C and D), both k_{cat}–pH and $k_{\mathrm{cat}}/K_{\mathrm{M}}$–pH data obtained with ***cys*** exhibit a “bell-shaped” curve with two resolved pK_a values. Both data sets were well fit using eq 1 (solid lines). Two pK_a values (5.64 ± 0.06 and 9.86 ± 0.06) were obtained from fitting the k_{cat}–pH result for reactions with ***cys*** at 25 °C. Similarly, two apparent pK_a values were obtained from fitting the k_{cat}/K_M–pH data (5.11 ± 0.07 and 9.74 ± 0.07).

Steady-state enzymatic reactions utilizing ***ca*** as a substrate exhibit decreased k_{cat} and k_{cat}/K_M values as compared to those of reactions conducted with ***3mpa***. Regardless, both k_{cat}–pH and k_{cat}/K_M–pH profiles were collected and analyzed as described above (Figure 3E,F). Unlike the results obtained in ***3mpa*** and ***cys*** reactions, only one ionizable group (pK_a = 6.6 ± 0.2) was observed in the k_{cat}–pH data set using ***ca*** as a substrate. As the rate of catalysis decreases only at low pH, these results were fit to equations 3 (solid line). Alternatively, the k_{cat}/K_M–pH data exhibited a “bell-shaped” curve similar to that of ***cys***, and thus, the results were fit to equation 1. A summary of the all pH-dependent kinetic results is provided in Table 1.

The influence of temperature on the maximal rate of *Av* MDO was also measured. These results are presented in Figure S3 of the Supporting Information.

EPR Spectroscopy of the Substrate-Bound *Av* MDO Iron-Nitrosyl Active Site (*Av* ES-NO)

Among non-heme mononuclear iron enzymes, a general mechanism for catalysis has emerged on the basis of extensive mechanistic, spectroscopic, and crystallographic characterization.[83, 84, 85] Typically, the monoanionic iron site contains a six-coordinate ferrous iron with solvent molecules serving as the nonprotein ligands. In most instances, the reduced active site is mostly unreactive toward O_2 until the substrate and/or cofactor is bound.[85] Thus, activation of O_2 occurs only following the ordered binding of the substrate and/or cofactor. Historically, experiments using nitric oxide (NO) as a spectroscopic probe for O_2 binding have been employed to verify this obligate-ordered reactivity. The assumption inherent in these experiments is that NO and O_2 bind similarly to the mononuclear Fe site. Assuming NO binds to only the substrate-bound complex, an additional advantage of these experiments is that quantitative EPR measurements can be made to explore the relative binding affinity of multiple substrates within the active site.

Addition of NO to a substrate-bound mononuclear non-heme iron center typically results in the formation of an $\{FeNO\}^7$ ($S = {}^3/_2$) species characterized by an axial EPR spectrum ($g_{x,y,z} \sim 4, 4, 2$). According to the Feltham–Enemark notation, the ground-state $S = {}^3/_2$ spin manifold can be described by an antiferromagnetic coupling between a high-spin Fe^{III} ($S = {}^5/_2$) and a bound NO^- anion ($S = 1$).[86, 8, 7]

Samples of the free enzyme and substrate-bound *Av* MDO (*Av* **ES**) were treated anaerobically with NO to determine if the "Gln-type" enzyme exhibits an obligate-ordered addition of substrate (***3mpa***) prior to NO. In the absence of ***3mpa***, no $\{FeNO\}^7$ ($S = {}^3/_2$) signals were observed by EPR upon stoichiometric addition of NO. Therefore, the ferrous iron active site of *Av* MDO is unable to bind NO in the absence of the substrate. As noted above, this behavior is quite typical among non-heme mononuclear iron enzymes and is consistent with reports for *Mm* CDO.[74] By contrast, addition of stoichiometric NO to samples containing an equimolar mixture of *Av* MDO and ***3mpa*** produces the EPR spectrum (***1***) shown in Figure 4A. The near axial $S = {}^3/_2$ EPR signal for the substrate-bound $\{FeNO\}^7$ *Av* MDO (*Av* **ES**-NO) has observable g values at 4.06, 3.96, and 2.0. This signal is produced only upon addition of NO to samples of enzyme precomplexed with ***3mpa***. The temperature-normalized signal intensity for ***1a*** decreases with increasing temperature, indicating that the $m_s = \pm{}^1/_2$ doublet is the ground state within the $S = {}^3/_2$ spin system. The magnitude of the zero-field splitting parameter ($D = 10 \pm 2$ cm^{-1}) was determined by plotting the EPR signal intensity of this signal versus $1/T$ and fitting the data to a Boltzmann population distribution for a two-level system. This value is in good agreement with those reported for other $\{FeNO\}^7$ ($S = {}^3/_2$) species.[6, 87] The EPR simulation (dashed lines) for ***1a*** shown in Figure 4 was calculated using this D value. For analytical purposes, all data were recorded below the microwave power necessary for half-saturation of the $\{FeNO\}^7$ $S = {}^3/_2$ signal at 10 K ($P_{1/2} = 300 \pm 50$ mW). Spin quantification of ***1a*** accounts for 380 μM (99% of the total ferrous iron within the sample). Analogous *Av* **ES**-NO samples were prepared using equimolar ***cys*** and *Av* MDO to explore the relative substrate binding affinity for this enzyme. As with ***3mpa***, pre-equilibration of *Av* MDO with ***cys*** induced NO binding at the enzymatic Fe site. As shown in Figure 4B (spectrum 2), addition of stoichiometric NO to the ***cys***-bound *Av* MDO produces two spectroscopically distinct $\{FeNO\}^7$ ($S = {}^3/_2$) species as indicated by the two sets of observable g values at (***2a***; 4.06, 3.96, and 2.0) and (***2b***; 4.31, 3.75, and 2.0). These species differ in their rhombicity (E/D values), 0.01 and 0.05, respectively. For the sake of clarity, the $g \sim 2$ region was omitted from Figure 4B. As with ***1a***, the temperature-normalized signal intensity for both ***2a*** and ***2b*** decreases with increasing temperature confirming that the $m_s = \pm{}^1/_2$ doublet is the ground state for both observable species. Spectra at elevated temperatures exhibit increased electronic relaxation rates resulting in broader EPR spectra. This effect can distort the baseline and decrease the accuracy of D values determined by Boltzmann fits. Therefore, additional corroboration of the zero-field splitting term was obtained by simultaneous simulation of EPR ($n = 6$) spectra collected at temperatures ranging from 4 to 40 K. Across this temperature range, all simulations accurately reproduce the relative intensity of ***2a*** and ***2b*** using a D of 10 ± 2 cm^{-1}. Thus, both $\{FeNO\}^7$ species ***2a*** and ***2b*** appear to have equivalent zero-field splittings. With the magnitude of the D value validated, quantitative simulations of each species (Figure 4B, dashed lines) were calculated to determine their relative distribution [60% (***2a***) to 40% (***2b***)]. Relative to the starting ferrous iron concentration, species ***2a*** (22%) and ***2b*** (13%)

account for ~35% of the iron in the sample. Thus, following stoichiometric addition of ***cys***, 65% of the enzyme is not substrate-bound and is therefore unreactive toward NO. This indicates that the relative binding affinity of ***3mpa*** within the *Av* MDO active site is significantly higher than that of ***cys***.

EPR spectra ***1a*** and ***2a*** exhibit identical *g* values, temperature dependence, and power saturation behavior ($P_{1/2}$); therefore, it is likely that the coordinating ligands and geometry within the first coordination sphere of both species are equivalent. By contrast, the microwave power necessary for half-saturation of the ***2b*** signal ($P_{1/2}$ = 650 ± 50 mW at 10 K) is significantly higher than that observed for ***1a*** or ***2a***. The increased relaxation ($P_{1/2}$) and rhombicity (E/D) observed suggest that the geometry of the ***2b*** first coordination sphere is significantly perturbed relative to those of ***1a*** and ***2a***. Potentially, the ***1a*** and ***2a*** signal reflects the catalytically relevant binding mode for this enzyme, whereas the distorted ***2b*** signal is attributed to an alternative (perhaps noncatalytic) substrate-bound configuration. A summary of the EPR parameters used to simulate the $\{FeNO\}^7$ ($S = {}^3/_2$) *Av* MDO signal is provided in Table 2.

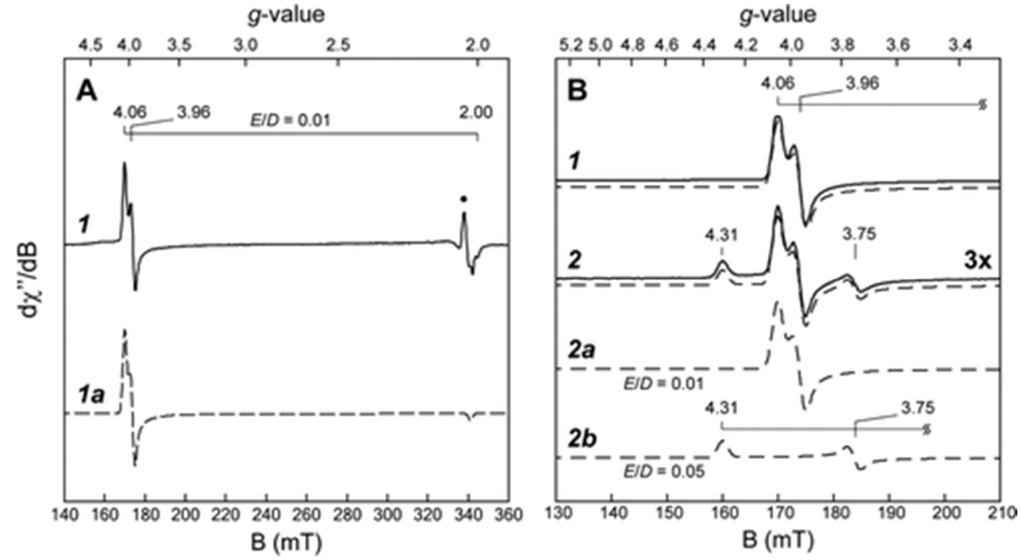

Figure 2-4. X-Band EPR spectra of *Av* **ES**-NO $\{FeNO\}^7$ ($S = {}^3/_2$) species. (A) Trace 1 illustrates the full $S = {}^3/_2$ spectrum produced upon addition of NO to enzyme precomplexed with ***3mpa***. A quantitative simulation (***1a***, dashed line) for this species is provided for comparison. The sharp g_{ave} ~ 2.03 signal designated by ● is attributed to minor dinitrosyl iron species, a common contaminant produced by addition of NO to Fe-containing enzymes.[88, 89, 90, 91, 46] An expansion of the g ~ 4 region (panel B) illustrates the perturbation to the obtained spectra upon substitution of an equal concentration of ***3mpa*** (***1***) for ***cys*** (***2***). The intensity of the *Av* **ES**-NO sample prepared with ***cys*** is multiplied by 3-fold for the sake of clarity. A two-component simulation for ***2a*** and ***2b*** is overlaid on spectra **2**. Spectroscopic parameters determined by Boltzmann temperature-dependent fits and spectroscopic simulations are listed in Table 2. Instrumental parameters: microwave frequency, 9.643 GHz; microwave power, 20 μW; modulation amplitude, 0.9 mT; temperature, 10 K.

Table 2-2. Simulation Parameters for *Av* MDO $\{FeNO\}^7$ Species

sample	signal	[Fe] (%)	g_1	g_2	σg_1	σg_2	D (cm^{-1})	E/D	σ_B (mT)
3mpa	***1a***	99	1.994	2.015	0.001	0.001	10 ± 2	0.005	0.5
cys	***2a***	22	1.995	2.014	0.001	0.001	10 ± 2	0.005	0.5
	2b	13	2.025	2.011	0.008	0.001	10 ± 2	0.048	0.5
eth	***3a***	20	1.996	2.032	0.037	0.037	10 ± 2	0.010	0.5
	3b	16	2.026	2.009	0.009	0.001	10 ± 2	0.049	0.5
ca	***4a***	4	1.997	2.031	0.036	0.037	10 ± 2	0.010	0.5
	4b	3	2.026	2.010	0.009	0.001	10 ± 2	0.048	0.5

In addition to the thiol, both ***3mpa*** and ***cys*** have a carboxylate functional group. Therefore, an obvious question to address is whether the substrate carboxylate group is directly coordinated to the ferrous iron site. To explore this possibility, equivalent EPR NO addition samples were prepared using stoichiometric ethanethiol (***et***) and cysteamine (***ca***). Figure 5 compares the $S = {}^3/_2$ signals observed for the ***et***-, ***ca***-, and ***cys***-bound *Av* **ES**-NO. As with samples prepared with ***cys***, both ***et***- and ***ca***-bound samples exhibit two spectroscopically distinct species. Except where specifically noted below, the observed *g* values and zero field splitting parameters are essentially equivalent to values reported for *Av* **ES**-NO prepared with ***cys***. For the sake of consistency, the two species are designated as "***a***-type" and "***b***-type" on the basis of their spectroscopic similarities to ***2a*** and ***2b***.

The most striking difference observed for the ***et***-bound (Figure 5, trace ***3***) and ***ca***-bound (trace ***4***) $\{FeNO\}^7$ ($S = {}^3/_2$) spectra is that they are significantly broader than those observed for the ***cys***-bound *Av* **ES**-NO (trace ***2***). This increased line width is attributed to structural distributions resulting in distributed *g* values along each principal axis of the tensor (*g* strain).[58, 88 ,89]The *g* strain in magnetic resonance measurements is analogous to the Debye–Waller factors (*B* factors) reported in crystallography. Simulations for spectra ***3*** and ***4*** include distributions of *g* values (σ_g) to account for their increased line width. As shown in Table 2, *Av* **ES**-NO samples prepared using ***et*** and ***ca*** have *g* strain ($\sigma g_{1,2} = 0.037$) significantly higher than that of samples prepared with ***cys*** ($\sigma g_{1,2} = 0.001$). Thus, the increased *g* strain observed for ***et***- and ***ca***-bound *Av* ES-NO species indicates a greater co-ordinational flexibility within the active site. By contrast, the ***cys***- and ***3mpa***-bound *Av* ES-NO appear to be much more structurally rigid.

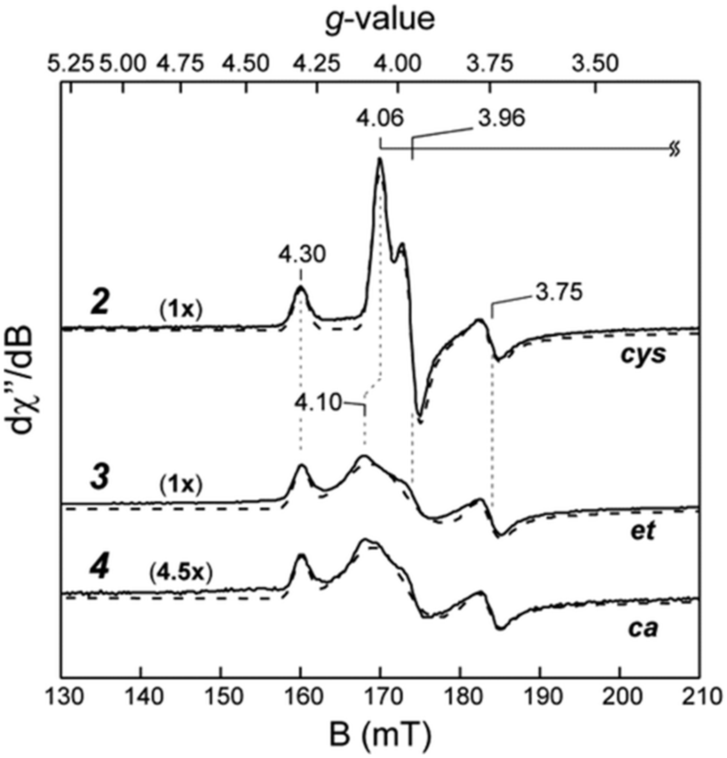

Figure 2-5. X-Band EPR spectra of *Av* **ES**-NO {FeNO}^{7} (S = $^3/_2$) species produced using l-cysteine (***2***, ***cys***), ethanethiol (***3***, ***et***), and cysteamine (***4***, ***ca***) as a substrate for MDO. All spectra are normalized for concentration, and scaling factors are indicated for each spectrum in parentheses. Parameters used for analytical simulations (dashed lines) are provided in Table 2. Instrumental parameters: microwave frequency, 9.643 GHz; microwave power, 200 μW; modulation amplitude, 0.9 mT; temperature, 10 K.

The concentration of ***et***-bound *Av* **ES**-NO species ***3a*** (20%) and ***3b*** (16%) determined by simulations (36% of total iron) indicates that the affinity for ***et*** within the *Av* MDO active site is essentially equivalent to that for ***cys***. Alternatively, samples prepared with ***ca*** exhibit a substantially lower yield (7% of the total iron) of ***4a*** (4%) and ***4b*** (3%) under identical conditions. Collectively, these experiments suggest the following order of preference within the *Av* MDO active site: ***3mpa*** > ***cys*** ~ ***et*** > ***ca***. This trend in relative substrate affinity, as well as the heterogeneity of EPR signals observed in samples prepared with ***cys*** and ***ca***, explains the higher K_M values obtained for ***cys*** and ***ca*** in steady-state assays.

A subtle shift in the lowest-field g value (g_1) from 4.06 to 4.10 is also observed in *Av* **ES**-NO samples prepared with ***et*** and ***ca***. This shift is observed only along the g_1 axis for species ***3a*** and ***4a***; all other g values are invariant. The alteration in the resonance frequency is due to a slight increase in rhombicity (E/D) from 0.005 to 0.010 in samples prepared with ***et*** and ***ca***. Both the increased g strain and the shift in active site rhombicity suggest that the substrate carboxylate group is involved in stabilizing interactions within the active site. However, given the small magnitude of the change, it is unlikely that the substrate carboxlate group is directly coordinated to the Fe site.

Discussion

The results presented here support the conclusion suggested by Driggers et al.[48] that the "Gln-type" *Av* MDO is more appropriately designated as a 3-mercaptopropionic acid dioxygenase (MDO) rather than a subclass of CDO enzymes. Beyond this, the results presented here also imply that "Gln-type" enzymes may serve as promiscuous thiol dioxygenases, capable of accommodating a variety of thiol-bearing substrates. By all metrics explored, the *Av* MDO exhibits distinct deviations in its behavior relative to that of mammalian CDO.

One of the most remarkable features of the "Gln-type" *Av* MDO enzyme is its relaxed substrate specificity. While it has been reported that *Mm* CDO is capable of catalyzing dioxygenations utilizing multiple thiol substrates (l-Cys, d-Cys, l-homocysteine, and l-penicillamine), no activity was observed in reactions using ***3mpa*** or mercaptosuccinate.[60] Furthermore, catalytic (k_{cat}/K_M) and coupling efficiencies for all *Mm* CDO reactions utilizing non-native substrates are exceedingly poor. For instance, in assays utilizing ***ca***, *Mm* CDO exhibits a k_{cat}/K_M ~4 orders of magnitude lower than that obtained in ***cys*** reactions. Furthermore, only ~1% of the O_2 consumed is converted into the hypotaurine product.[60] Presumably, these vastly uncoupled reactions result in the release of reactive oxygen species such as H_2O_2, $O_2^{\bullet-}$, and $^{\bullet}OH$. By contrast, *Av* MDO reactions with ***3mpa*** and ***cys*** are fully coupled; only in reactions with ***ca*** is the coupling efficiency significantly decreased (40 ± 9%). For perspective, the k_{cat}/K_M values obtained in *Av* MDO reactions with ***ca*** are ~1000-fold greater than those of equivalent reactions with *Mm* CDO. For all substrates utilized in *Av* MDO steady-state assays, the reaction rate at saturating substrate concentrations is independent of oxygen concentration within the range of 50–400 μM. This indicates that the apparent K_M^{02} (for all substrates) must be substantially lower (~10 times) than the lowest value of oxygen used (50 μM).[92] Therefore, the differential activity exhibited by *Av* MDO in reactions using ***3mpa***, ***cys***, and ***ca*** cannot be attributed to incomplete O_2 saturation.

An obvious question is whether *Av* MDO functions as a CDO physiologically. Both enzymes exhibit comparable k_{cat} values (0.6–1.2 s^{-1}) and enzymatic efficiencies (110 ± 20 M^{-1} s^{-1} $< k_{cat}/K_M < 260 \pm 30$ M^{-1} s^{-1}) in reactions with ***cys***. Therefore, even with the higher K_M value exhibited by *Av* MDO, it is possible that this enzyme serves as CDO *in vivo*. This speculation is strengthened by the absence of any other putative CDO enzyme identified by a NCBI BLAST search within the *A. vinelandii* (taxid 354) genome. However, the vastly higher k_{cat}/K_M value observed in reactions with ***3mpa*** establishes a clear preference for this substrate. This suggests that *Av* MDO could function to produce ***csa*** only in the absence of ***3mpa***. By the same logic, it is not expected that *Av* MDO would contribute significant ADO functionality in the presence appreciable ***3mpa*** or ***cys*** concentrations.

Another important distinction between *Av* MDO and *Mm* CDO catalysis is illustrated by comparing the kinetics obtained in reactions using ***3mpa***, ***cys***, and ***ca*** as substrates for the "Gln-type" enzyme. The ~3-fold decrease in k_{cat} (0.29 ± 0.08 s^{-1}) obtained in ***ca*** reactions (relative to ***3mpa*** and ***cys*** reactions) suggests that the substrate carboxylate group (absent in ***ca***) represents an important (but not required) point of interaction within the *Av* MDO active site. By contrast, the bidentate coordination of ***cys*** within the *Mm* CDO active site mandates that all potential substrates must contain both thiol and amine functional groups.[60, 74] This implies that substrate binding at the *Av* MDO Fe site occurs solely by thiolate coordination rather than bidentate as is the case of *Mm* CDO.

Additional mechanistic insight into *Av* MDO can be obtained by inspection of the k_{cat}–pH and k_{cat}/K_M–pH profiles. For example, the basic pK_a values obtained in k_{cat}–pH profiles generated using ***3mpa*** (9.5 ± 0.1) and ***cys*** (9.9 ± 0.1) are quite similar. It could be argued that the decreased activity observed in both k_{cat}–pH profiles is simply attributed to contributions from denatured enzyme. However, several observations suggest otherwise. First, for each substrate, the slopes of tangent lines drawn within the increasing and decreasing arms of the inverted bell curve approach unity. This behavior is consistent with a single protonation event associated with an ionizable group. Second, the basic pK_a value is absent in the k_{cat}–pH profile obtained for reactions of *Av* MDO with ***ca***. This observation suggests that the basic ionizable groups observed in reactions with ***3mpa*** and ***cys*** are catalytically relevant. As the basic pK_a values observed in k_{cat}–pH profiles for ***3mpa*** and ***cys*** reactions are close to those typically associated with tyrosine (pK_a ~ 10), it is tempting to speculate that this ionizable group is associated with the conserved tyrosine residue (Y164) directly adjacent (4.15 Å)[48] to the *Av* MDO Fe site. The absence of this feature in reactions using ***ca*** implies that the basic ionizable group participates in hydrogen bonding with the substrate carboxylate group. It has been previously demonstrated in steady-state assays with active site variants and spectroscopically validated computational studies that the hydroxyl group of Y157 within the *Mm* CDO active site interacts with the carboxylate group of the Fe-bound substrate (***cys***).[58] Moreover, *Mm* CDO exhibits a similar basic pK_a value (10.30 ± 0.08) in pH-dependent steady-state ***cys*** reactions. [75] Clearly, additional studies are necessary before the unambiguous assignment of this ionizable group to a specific residue within the active site.

The second, more acidic ionizable group is observed near neutral pH ($5.6 < pK_a < 6.9$) for all k_{cat}–pH substrate profiles. This pK_a value is comparable to those typically associated with deprotonation of a histidine imidazole ring ($pK_a \sim 6.0$). It is therefore worth considering the possibility that this ionizable group is associated with one of the conserved histidine residues within the *Av* MDO active site (H84, H86, H147, and H162). Because protonation of the 3-His facial triad ligands (H84, H86, and H147) would result in loss of Fe coordination, it is expected that enzymatic activity would be abolished below this pK_a value if it was associated with any facial triad residues. Instead, k_{cat} decreases sigmoidally to a finite but non-zero value. Therefore, this ionizable group cannot be associated with any of the Fe-coordinating His residues. This leaves only H162 to consider further.

A recent report detailing the spectroscopic and computational modeling of a *Mm* CDO H155A variant (equivalent to *Av* MDO H162) provides an intriguing hypothesis.[90] In this study, it was proposed that the role of H155 is to act as a hydrogen bond donor for the Y157 phenol group. It was argued that this interaction serves to optimally position the Y157 phenol group (of the C93–Y157 pair) to donate a hydrogen bond to the Fe-bound ***cys*** carboxylate group. An additional benefit of this interaction is that it positions the C93–Y157 pair such that solvent access to the Fe site is restricted.[90] By analogy to this model, it is reasonable to assume that H162 within the *Av* MDO active site provides a similar interaction with Y164 to stabilize hydrogen bonding with the ***3mpa*** carboxylate group as illustrated in Scheme 2. This model also presents an attractive explanation for the role of the "catalytic triad" of conserved Ser, His, and Tyr residues, largely conserved among CDO enzymes.[91] In principle, the S160 hydroxyl group of serves as a hydrogen bond donor to the N_ε atom of H162. This in turn aligns the opposite N_δ atom within the imidazole ring for donation of a hydrogen bond to the phenol group of Y164. Protonation of H162 would disrupt the Ser-His-Try hydrogen bond network, resulting in a decreased level of substrate stabilization as observed experimentally. Furthermore, because the ***cys*** carboxylate group ($pK_a \sim 1.9$) is more acidic than that of ***3mpa*** (4.34), a hydrogen bond network between the substrate carboxylate group and the "catalytic triad" would explain the acidic shift of pK_{a1} ($\Delta pK_{a1} \sim -1.3$) observed in the ***cys*** k_{cat}–pH profile relative to that of ***3mpa***. Additional studies are in progress to corroborate this hypothesis.

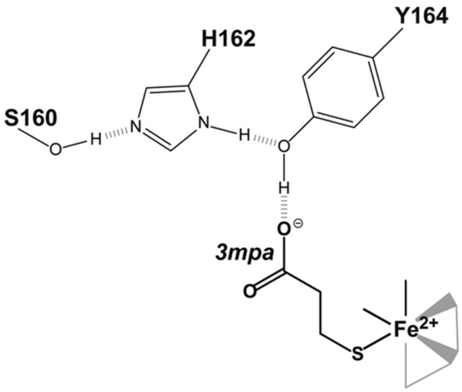

Scheme 2-2. Proposed Coordination of Substrate-Bound Active Site for *Av* MDO

In reactions utilizing NO as a surrogate for O_2 binding, it was verified that *Av* MDO exhibits an obligate ordered addition of substrate prior to NO. As demonstrated here, this property can be exploited to quantify the amount of substrate-bound enzyme by EPR spectroscopy. Using this method, the relative binding affinities of thiol substrates (***3mpa***, ***cys***, and ***ca***) were determined to supplement kinetic results. The quantitative yield and homogeneity of $\{FeNO\}^7$ ($S = {}^3/_2$) EPR spectra obtained for *Av* **ES**-NO samples prepared with ***3mpa*** clearly indicate a strong preference for this substrate. Both the decreased yield of *Av* **ES**-NO produced and the spectroscopic heterogeneity of $\{FeNO\}^7$ ($S = {}^3/_2$) species observed in samples prepared with ***cys*** indicate a decreased affinity for this substrate relative to that for ***3mpa***.

For substrates lacking a carboxylate functional group (ethanethiol and cysteamine), the most pronounced change to the *Av* **ES**-NO EPR spectra is the increased line width due to *g* strain (σ_g). In fact, the value of σ_g increases by nearly 40-fold for these substrates relative to those for ***3mpa*** and ***cys***. Although steady-state kinetics using ethanethiol were not performed, [46] quantification of *Av* **ES**-NO samples prepared with ***et*** produces yields nearly equivalent to those prepared with ***cys***. This observation clearly demonstrates that only the substrate thiol functional group is required to initiate NO binding at the *Av* MDO active site. Moreover, because quantification of the ***ca***-bound $\{FeNO\}^7$ ($S = {}^3/_2$) signal shows it is ~5-fold lower than those of equivalent samples prepared with ***et***, we can conclude that the amine functional group on ***ca*** (and ***cys***) significantly inhibits binding within the active site. Overall, the trend in relative substrate binding affinities (***3mpa*** > ***cys*** > ***ca***) determined by analytical EPR is largely consistent with the K_M values obtained from steady-state results.

In addition to the increased line width for *Av* **ES**-NO species produced with ***et*** and ***ca***, there is also a slight increase in rhombicity ($\Delta_{E/D} = +0.005$) for the "***a***-type" $\{FeNO\}^7$ spectra [***3a*** (***et***-bound) and ***4a*** (***ca***-bound)]. This perturbation to the EPR spectra is observed for only substrates lacking a carboxyl functional group. Energetically, this effect is too weak to represent a significant change in the Fe coordination-sphere ligands. Therefore, we postulate that this is due to a minor geometric change at the substrate-bound $\{FeNO\}^7$ site. Taken together with the increased *g* strain and kinetic results, it is reasonable to conclude that these perturbations in the EPR spectra reflect the absence of stabilizing hydrogen bonding interactions with the substrate carboxylate group as illustrated in Scheme 2.

An argument can be made for bidentate coordination of ***3mpa*** and ***cys*** via thiolate and carboxylate groups. Indeed, sufficient space is available within the active site cavity to accommodate this configuration. [48] However, both ***et***- and ***cys***-bound $\{FeNO\}^7$ species are produced in comparable yields under equivalent conditions. This observation indicates the absence of a chelate effect for ***cys***, which would be anticipated for bidentate coordination. Moreover, steady-state kinetics utilizing ***ca*** clearly demonstrate that a substrate carboxylate group is not required for catalysis. Bidentate coordination of ***cys*** or ***ca*** via neutral amine and thiolate can also be ruled out as this would be expected to produce a low-spin $\{FeNO\}^7$ ($S = {}^1/_2$) species as previously demonstrated for *Mm* **ES**-NO and inorganic model complexes of this enzyme.[74, 93, 94] Given all of the results presented here, we can conclude that substrate binding to the *Av* MDO Fe site is solely through thiolate ligation.

The origin of the more rhombic "***b***-type" signal (***2-4b***) observed (*g* values of 4.31, 3.75, and 2.0; $E/D = 0.05$) in samples prepared using ***cys***, ***et***, and ***ca*** is not clear but suggests an alternative binding mode is possible for these substrates. For example, these signals may reflect a mixture of substrate binding *trans* to H94 (displacing W2) and *trans* to H96 as postulated for ***3mpa*** (Figure 1B). Alternatively, they could reflect a difference in Fe coordination number (loss of W2) or Fe-bound solvent protonation state (^{-}OH versus H_2O). Clearly, additional structural and spectroscopic investigations of the "Gln-type" enzymes are necessary to understand the origin of this substrate binding heterogeneity.

While the crystal structure for the substrate-bound *Av* MDO has not been determined, structural comparisons can be made to the *Ra. eutropha* “Gln-type” MDO (PDB entry 4QMA) shown in Figure 1B. [48] Of note, a putative Fe-bound oxygen molecule is modeled into this structure *trans* to H147. All known $\{FeNO\}^7$ ($S = {}^3/_2$) synthetic complexes exhibit end-on NO coordination via the N atom with an average Fe–N–O bond angle and an Fe–NO bond distance of 162 ± 11° and 1.74 ± 0.04 Å, respectively.[95] Therefore, assuming NO binds end-on at the same position as the putative oxygen in Figure 1B, substrate binding would be expected to displace one or more of the Fe-coordinated solvent waters (designated W1 and W2). On the basis of the ***cys***-bound *Mm* CDO structure (Figure 1A), it is reasonable to expect the ***3mpa*** thiolate to coordinate to the ferrous iron site *trans* H96. This would place the ***3mpa*** carboxylate group in a favorable position for hydrogen bonding with the “catalytic triad” as illustrated in Scheme 2.

By analogy to mechanisms proposed for CDO,[74 3, 96, 97, 98] two reaction pathways (Scheme 3) can be considered for *Av* MDO that ultimately lead to the production of 3-sulfinopropionic acid (***spa***) and a ferrous iron resting state for the enzyme. In the first step, reversible binding of the ***3mpa*** substrate (***A***) via thiolate coordination precedes O_2 binding at the substrate-bound ferrous active site (***B***).

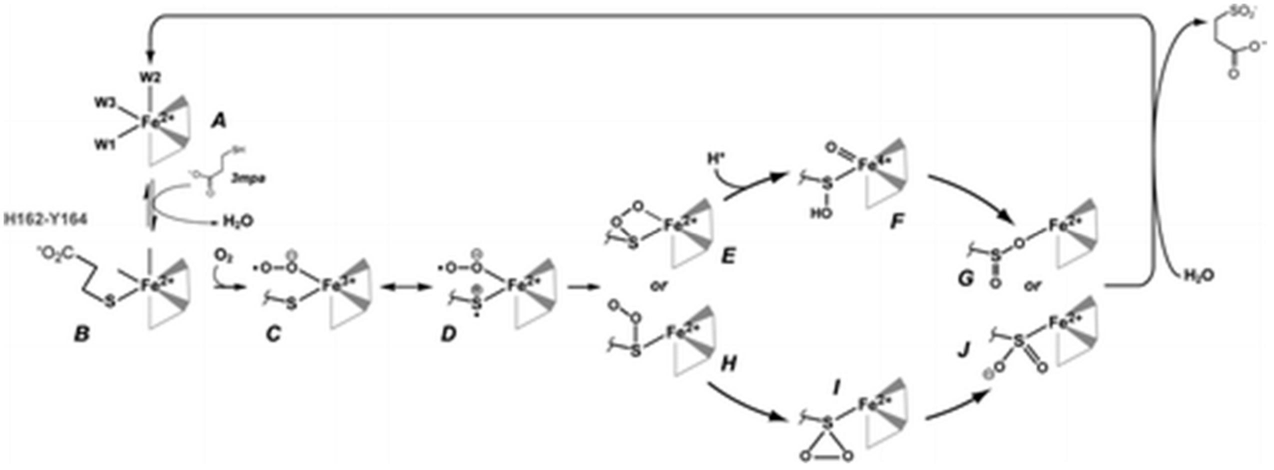

Scheme 2-3. Summary of Possible Catalytic Reaction Mechanisms for *Av* MDO

Oxidative addition of O_2 to the ferrous iron is expected to occur via an internal electron transfer to yield a short-lived ferric–superoxo [Fe^{III}–$O_2^{\bullet-}$] species (***C***). Resonance charge transfer between the ferric iron and the bound ***3mpa*** thiolate could impart transient radical character on the S atom (***D***), resulting in rapid recombination of bound superoxide and thiol radicals. Previous spectroscopic studies identified a putative Fe^{III}–superoxide intermediate generated in *Mm* CDO chemical-rescue experiments.[80] However, while the decay of this intermediate was kinetically matched to product formation, its rate was significantly slower than the rate of steady-state turnover for *Mm* CDO. It is therefore not clear if this represents a catalytically relevant intermediate.

At this point, the reaction mechanism diverges to support formation of two potential intermediates. Recombination of the Fe-distal O atom with the S radical cation is predicted to produce the cyclic four-membered Fe–O–O–S ring structure (***E***). Several computational studies support the formation of this structure.[3,96, 97] Heterolytic cleavage of the O–O bond (upper pathway) is expected to produce a transient Fe^{IV}–oxo species (***F***) analogous to those observed in other non-heme iron dioxygenases [taurine α-ketoglutarate (αKG)-dependent dioxygenase (TauD) and prolyl-4-hydroxylase (P4H)]. [99, 100, 101, 102, 103] Computational results also suggest rapid rearrangement of (***F***) to favor direct coordination of the cysteine sulfenate O atom that directly precedes final Fe^{IV}–oxo rebound to generate a ferrous iron-bound ***csa*** (***G***).[3, 96, 97]This mechanism predicts direct O atom coordination of the ***spa*** product to the ferrous iron site (***G***). While supported computationally, no experimental evidence of this mechanism has been reported.

An alternative model for thiol oxidation has been proposed on the basis of a putative ferrous iron-bound persulfenate intermediate identified in crystallographic studies with CDO.[71, 98] In this mechanism (lower pathway), nucleophilic attack of the Fe-proximal O atom on the Fe-bound thiolate S atom would result in the formation of a substrate persulfenate species (***H***). This could potentially produce a thiadioxirane intermediate (***I***) and, following heterolytic cleavage of the thiadioxirane O–O bond, ultimately result in formation of the ***spa*** product and a resting ferrous enzyme (***J***). In this reaction pathway, it is expected that the ***spa*** S atom is directly coordinated to the ferrous iron site (***J***). Interestingly, the direct coordination of the S atom to the Fe site is more consistent with inorganic model complexes containing metal-bound sulfinates derived from oxidation of thiolate ligands. [104, 105] Finally, release of product from ***G*** or ***J*** cycles the enzyme back to the resting state (***A***).

Chapter 3: Non-chemical proton-dependent steps prior to O_2-activaiton limit *Azotobacter vinelandii* 3-mercaptopropionic acid dioxygenase (MDO) catalysis[†]

Introduction

Thiol dioxygenase enzymes utilize a mononuclear non-heme iron site to catalyze the O_2-dependent oxidation of thiol bearing substrates without the need for an external reductant. Among this class of enzymes, the mammalian cysteine dioxygenase (CDO) is the best characterized.[51, 56, 61, 106, 107] Enzymes involved in sulfur-oxidation and transfer are increasingly being recognized as potential drug targets for development of antimicrobials, therapies for cancer and inflammatory disease.[63, 64, 65, 66] Imbalances in *L*-cysteine (***cys***) metabolism have also been identified in a variety of neurological disease states (motor neuron, Parkinson and Alzheimer).[56, 67, 68]These observations suggest a potential correlation between impaired sulfur metabolism, oxidative stress and neurodegenerative disease.[69, 70]

Multiple high-resolution crystal structures have been solved highlighting the conserved Fe-coordination sphere among confirmed thiol dioxygenase enzymes. The typical non-heme mononuclear oxidase/oxygenase iron coordination sphere is comprised of two protein-derived neutral His residues and one monoanionic carboxylate ligand provided by either an Asp or Glu residue. By contrast, the mononuclear iron site in all known thiol dioxygenase enzymes is coordinated by three protein derived histidine residues resulting in a 3-His facial triad.

Structural comparison of annotated bacterial thiol dioxygenase enzymes suggests at least two subclasses of enzymes, which differ in a single outer Fe-coordination sphere residue (Arg or Asn).[57] To illustrate, **Figure 1** shows the active site coordination for the 'Arg-type' bacterial cysteine dioxygenase (CDO) isolated form *Bacillus subtilis* (PDB code 4QM8) as compared to the

'Gln-type' enzyme cloned from *Pseudomonas aeruginosa* (PDB code 4TLF).[108] Of note, the 3-His facial triad motif in both enzymes is conserved; however, the outer-sphere Arg-residue (R50) involved in electrostatic stabilization of the ***cys*** substrate is replaced by Gln (Q62). The spatial orientations of all other conserved residues (S137, H139 and Y141) within the active site remain invariant. The primary difference between the eukaryotic and bacterial 'Arg-type' CDO enzymes is a post-translational modification adjacent (3.3 Å) to the mononuclear Fe-site in which spatially adjacent Cys93 and Tyr157 residues are covalently cross linked to produce a C93-Y157 pair. This feature is unique to eukaryotic enzymes.[74, 109]

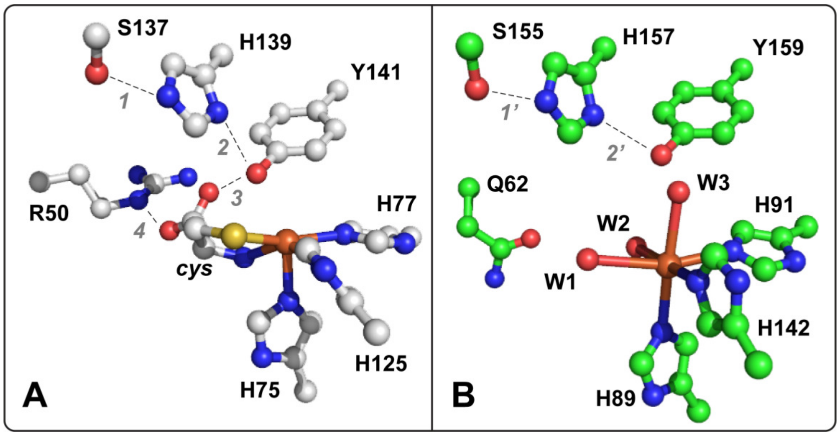

Figure 3- 1: Crystal structure of the substrate-bound 'Arg-type' *Bacillus subtilis* active site (**A**, PDB code 4QM8) as compared to the annotated 'Gln-type' MDO isolated from *Pseudomonas aeruginosa* (**B**, PDB code 4TLF).[57, 108] Solvent waters are designated **W1-W3**. Selected distances **A**: ***1*** (2.59 Å); ***2*** (3.30 Å); ***3*** (2.14 Å); ***4*** (2.65 Å); **B**: ***1'*** (2.56 Å); ***2'*** (2.95 Å)

Previously, both 'Arg-' and 'Gln-type' enzymes were annotated as bacterial CDO enzymes.[57] However, recent spectroscopic and kinetic investigations performed independently demonstrated that the 'Gln-type' class of thiol dioxygenase enzymes are more accurately designated as a 3-

mercaptopropionic acid dioxygenase (MDO).[108, 110] Remarkably, these 'Gln-type' enzymes have vastly relaxed substrate-specificity as compared to CDO. Indeed, MDO isolated from the soil bacteria *Azotobacter vinelandii* (*Av* MDO) demonstrated comparable activity (k_{cat}) toward three different thiol-bearing substrates [3-mercaptopropionic acid (***3mpa***), *L*-cysteine (***cys***) and cysteamine (***ca***)]. Despite similar maximal velocities, the 'Gln-type' *Av* MDO exhibits a catalytic efficiency (k_{cat}/K_M) for ***3mpa*** nearly two orders of magnitude greater than ***cys*** and ***ca***. [110] Thus, ***3mpa*** appears to be the preferred substrate for this enzyme. Similar behavior was reported for the 'Gln-type' enzyme isolated from *Pseudomonas aeruginosa*.[108]

While the mammalian 'Arg-type' CDO isolated from *Mus musculus* (*Mm* CDO) has been extensively characterized, no information is available regarding the relative timing of chemical and non-chemical steps in 'Gln-type' MDO catalyzed reactions. Comparing the kinetic mechanisms for various thiol dioxygenase enzymes is critical to identifying common mechanistic behavior among this class of enzymes. To this end, the influence of pH, solvent isotope and viscosity effects were evaluated for MDO steady-state kinetic parameters (k_{cat} and k_{cat}/K_M) obtained using two different substrates (***3mpa*** and ***cys***). Proton-inventory experiments were performed to determine the number of exchangeable protons in flight during chemical steps. The relative timing of diffusional steps was investigated by measuring the influence of solvent viscosity on enzyme kinetics. Collectively, these results provide greater insight into the role of conserved outer Fe-coordination sphere residues and the nature of substrate coordination to the mononuclear iron active site.

Materials and Methods

Expression and Purification of Av MDO

The isopropyl β-D-1-thiogalactopyranoside (IPTG) inducible T7 vector for *Av MDO* (designated pRP42), was a generous gift from Professor Tim Larson (Virginia Tech, Department of Biochemistry). Sequence verification of the plasmid was performed by Sequetech (Mountain View, CA, http://sequetech.com/). The pRP42 vector was transformed into chemically competent BL21(DE3) *E. coli* (Novagen Cat. no. 70236-4) by heat-shock [42 °C for 45 seconds] and grown overnight at 37 °C on a lysogeny broth (LB)[111] agar plate in the presence of 100 mg/L ampicillin (Amp). The following day, a single colony was selected for growth in liquid LB (Amp) media for training on antibiotic prior to inoculation of 10-L BF-110 fermentor (New Brunswick Scientific) at 37 °C. Cell growth was followed by optical density at 600 nm (OD_{600}). Induction was initiated by addition of 1.0 g IPTG, 78 mg ferrous ammonium sulfate and 20 g casamino acids at an OD_{600} ~4. At the time of induction, the temperature of the bioreactor was decreased from 37 °C to 25 °C and agitation was set to maintain an O_2 concentration of 20% relative to air-saturated media. After 4 hours, the cells were harvested and pelleted by centrifugation (Beckman-Coulter Avanti J-E, JA 10.5 rotor) at 18,600 × g for 15 min. The resulting cell paste was stored at -80 °C.

In a typical purification, ~20 g frozen cell paste was added to 150 mL extraction buffer (20 mM HEPES, 50 mM NaCl, pH 8.0). Lysosyme, ribonuclease and deoxyribonuclease were added to the slurry for a final concentration of 10 µg/mL each and stirred slowly on ice for 30 minutes. The resulting suspension was pulse sonicated (Bronson Digital 250/450) for 15 seconds on/off at 60% amplitude for a total time of 15 minutes. The insoluble debris was removed from the cell free extract by centrifugation at 48,000 x g for 1 hour at 4 °C. The supernatant was diluted 1:1 with extraction buffer and then loaded onto a DEAE sepharose fast flow anion exchange column [7cm W x 20 cm L] (GE Life Sciences #17070901) pre-equilibrated with 20 mM HEPES, 50 mM NaCl, pH 8.0. The column was washed with three column volumes of extraction buffer prior to elution in a linear NaCl gradient (50 mM – 350 mM). Fractions (~10 mL) were collected overnight and pooled based on enzymatic activity as described elsewhere.[76, 110] SDS PAGE was also used to verify the presence of the recombinant protein (~23 kDa) within each fraction. Broad range protein molecular weight markers utilized in SDS PAGE experiments were purchased from Promega (Madison, WI) Cat. No. V8491. The pooled fractions were concentrated to approximately 5-10 mL using an Amicon stir cell equipped with an YM-10 ultrafiltration membrane. Thrombin protease (Biopharma Laboratories) was added to cleave the C-terminal His-tag from *Av* MDO. In a typical reaction, ~0.3 molar equivalents of thrombin per *Av* MDO (based on UV-visible absorbance at 280 nm) was added to batches of purified protein for overnight cleavage at 4 °C in HEPES buffer. The remaining thrombin and free $(His)_6$-tag was removed from *Av* MDO by size exclusion chromatography using a sephacryl S100 column. For all batches of *Av* MDO used in these experiments, spectrophotometric determination of ferrous and ferric iron content was measured using 2,4,6-tripyridyl-s-triazine (TPTZ) as described elsewhere.[76, 110] For clarity, the concentrations reported in enzymatic assays reflect the concentration of ferrous iron within samples of *Av* MDO (Fe^{II}-MDO). Protein content was determined by Bio-Rad protein assay.

Enzyme assays

3-sulfinopropionic acid (***3spa***), cysteine sulfinic acid (***csa***) and hypotaurine (***ht***) were assayed using the HPLC method described previously.[78, 110, 112] Instrumental conditions: column, Phenomenex C18 (100 mm x 4.6 mm); mobile phase, 20 mM sodium acetate, 0.6 % methanol, 1 % (v/v) heptaflurobutyric acid, pH 2.0. Analytes were detected spectrophotometrically at 218 nm. Reactions (1 mL) were prepared in a buffered solution at the desired pH to obtain a final concentration from 0.1 to 10 mM ***3mpa*** (0.1 - 60 mM ***cys***). Each reaction was initiated by addition of *Av* MDO (typically 0.5 - 1.0 µM) at 20 ± 2 °C. Sample aliquots (250 µL) were removed from the reaction vial at selected time points and quenched by addition of 10 µL 1 N HCl (final pH 2.0). Prior to HPLC analysis, each sample was spin-filtered through a 0.22 µm cellulose acetate membrane (Corning, Spin-X). Product concentration was determined by comparison to calibration curves as described elsewhere.[109, 110] The rate of dioxygen consumption in activity assays was determined polarographically using a standard Clark electrode (Hansatech Instruments, Norfolk, England) in a jacketed 2.5 mL cell. Calibration of O_2-electrode is described in detail elsewhere.[78, 79] All reactions were initiated by addition of 1.0 µM *Av* MDO under identical buffer conditions as described for HPLC assays. Reaction temperatures were maintained at 20 ± 2 °C by circulating water bath (ThermoFlex 900, Thermo Scientific).

Synthesis of dianionic 3-sulfinopropionic acid

The salt of 3-sulfinopropionic acid (***3spa***) was prepared by saponification of the commercially available methyl ester [sodium 1-methyl 3-sulfinopropanoate; Sigma Aldrich 778168]. Briefly, sodium 1-methyl-3-sulfinopropanoate (100 mg, 0.57 mmol) was dissolved in 5 mL of deionized water. To this solution, LiOH (70 mg, 2.9 mmol) was added and then heated in an oil bath to reflux (~110 ºC) and stirred overnight. The solution was then cooled to ~4 ºC, filtered and the filtrate was dried by rotary evaporation. The resulting solid was dissolved in 2 mL of cold ethanol and the mixture was filtered to remove inorganic salts. Evaporation of the ethanol filtrate gave the desired compound as a white solid (68 mg, 0.45 mmol, 79%). Both ^{1}H and $^{13}C\ \{^{1}H\}$ NMR were measured to verify the identity and relative purity of the ***3spa*** product. ^{1}H NMR (500 MHz, D_2O) δ 2.49 (t, J = 7.8 Hz, 2H), 2.37 (t, J = 7.8 Hz, 2H). $^{13}C\ \{^{1}H\}$ NMR (126 MHz, D_2O) δ 181.2, 57.3, 30.1 ppm. Additional confirmation of ***3spa*** standard was performed by mass spectrometry as described elsewhere[110] with instrumentation from the Shimadzu Center for Advanced Analytical Chemistry (The University of Texas Arlington).

Solvent kinetic isotope effects and proton inventory

For pH/D-profiles (collectively pL) and solvent isotope studies, the buffer components were prepared directly in D_2O and adjusted by direct addition of NaOD. Each pD value was obtained from the pH-electrode reading using the relationship [pD = pH + 0.4]. The composition of reaction buffers for all pL-profile experiments consisted of 20 mM Good's buffer and 50 mM NaCl. 2-(*N*-morpholino)ethanesulfonic acid (MES) was used to buffer reactions over the pL range of 5.5 - 6.9, 2-[4-(2-hydroxyethyl)piperazin-1-yl]ethanesulfonic acid (HEPES) was used to buffer reactions over the pH/D range of 7.0 - 8.4 and 2-(cyclohexylamino)-ethanesulfonic acid (CHES) was used to buffer reactions over the pL range of 8.5 - 10. For proton inventory experiments, the mole fraction of D_2O (n) was calculated based on combining appropriate ratios of buffer prepared in D_2O and H_2O.

Viscosity studies

For solvent viscosity studies the steady-state kinetic parameters (k_{cat} and k_{cat}/K_M) were determined for *Av* MDO catalysis using both oxygen electrode and HPLC at pH 8.0 (20 °C) as described above. Sucrose was used as the viscogen to increase the buffer viscosity within reaction mixtures. The viscosity (η) of buffers containing sucrose were measured using an Ostwald viscometer relative to 20 mM HEPES, 50 mM NaCl, pH 8.2 (20 °C). The values obtained represent the average of triplicate measurements. In these experiments, addition of sucrose up to 35% (*w*/*v*) was used to increase the relative viscosity of the buffer (η_{rel}) up to ~3-times that of the control buffer.

Data Analysis

Steady-state kinetic parameters were determined by fitting data to the Michaelis-Menten equation using the program SigmaPlot ver. 11.0 (Systat Software Inc., Chicago, IL). From this analysis, both the kinetic parameters (k_{cat} and K_M) and error associated with each value were obtained by non-linear regression. For reactions where k_{cat}- or k_{cat}/K_M-pH profiles approaches limiting values (Y_L and Y_H) at low and high pH, the results were fit to equation (**1**). Here, Y is defined by either k_{cat} or k_{cat}/K_M, and the variables [H], K_1, and K_2 represent the hydrogen ion concentration and the two observable dissociation constants for ionizable groups involved in catalysis, respectively.

Equation **1**. $$\log Y = log\left(\frac{Y_L + Y_H \cdot \frac{K_1}{[H]}}{1 + \frac{K_1}{[H]}}\right)$$

Alternatively, for reactions where the pH-dependences of steady state kinetic parameters is ‘bell shaped’ in that they decrease at both low and high pH values, data were fit to equation (**2**).[80, 92, 113] This expression is scaled by a constant scalar quantity (C) which represent the maximum kinetic rate (k_{cat} or k_{cat}/K_M).

Equation **2**. $$\log Y = log\left(\frac{C}{\left(1+\frac{[H]}{K_1}\right)\left(1+\frac{K_2}{[H]}\right)}\right)$$

Table 3-1: Summary of pL-dependent steady-state kinetic parameters determined for MDO in reactions utilizing 3-mercaptopropionic acid and L-cysteine.

Av MDO kinetic parameter	**Substrate**			
	3mpa		***cys***	
	H_2O	D_2O	H_2O	D_2O
log(k_{cat})-pL				
maximum k_{cat} (s^{-1})	0.44 + 0.05	0.42 + 0.02	0.28 ± 0.02	0.26 ± 0.02
pK_{a1}	7.7 ± 0.1	7.7 ± 0.1	6.3 ± 0.1	7.1 ± 0.1
pK_{a2}	9.3 ± 0.5	9.3 ± 0.5	10.0 ± 0.1	10.5 ± 0.2
SKIE	1.05 ± 0.12		1.08 ± 0.10	
log(k_{cat}/K_M)-pL				
maximum k_{cat}/K_M ($M^{-1}s^{-1}$)	25,500 ± 240	9,000 ± 130	41.5 ± 0.7	40.8 ±0.5
pK_{a1}	6.9 ± 0.2	7.4 ± 0.2	6.3 ± 0.1	7.3 ± 0.1
pK_{a2}	9.2 ± 0.1	9.3 ± 0.1	9.5 ± 0.1	10.0 ± 0.1
SKIE	2.82 ± 0.11		1.02 ± 0.09	
proton inventory				
pL 6.0	$y > 1$		*n/a*	
pL = 8.2	$y > 1$		*n/a*	

Proton inventory results were fit to equation (**3**) where *n* is the mol fraction of D_2O in the reaction chamber and E_0 and E_n are the kinetic parameters (either k_{cat} or k_{cat}/K_M) in H_2O and the mol fraction of D_2O, respectively. The measured solvent kinetic isotope effect is defined as SKIE and the integer value *y* describes the number of protons that contribute to the isotope effect.

Equation **3**.

$$\frac{E_n}{E_0} = \left(1 - n + \left(\frac{n}{SKIE}\right)\right)^{y}$$

The effect of solvent viscosity on the steady-state parameters were fit using equation (**4**). In this equation, Y_0 represents each kinetic parameter determined in the absence of viscogen whereas Y_η is the value obtained at each specific relative viscosity measured. All viscosities measured are normalized to reaction buffer in the absence of viscogen (η_{rel}). The slope of the line (*m*) represents the extent of diffusion limitation.

Equation **4**. $$\frac{Y_0}{Y_\eta} = 1 + m \cdot \eta_{rel}$$

Results

1. Solvent kinetic isotope effects

It has been previously observed that *Av MDO* catalyzes the O_2-dependent oxidation of multiple thiol-bearing substrates 3-mercaptopropionic acid (***3mpa***), *L*-cysteine (***cys***) and cysteamine (***ca***) to yield the corresponding sulfinic acid products 3-sulfinopropionic acid (***3spa***), cysteine sulfinic acid (***csa***) and hypotaurine (***ht***), respectively.[110] In order to probe the rate-limiting chemical and non-chemical steps in *Av* MDO catalysis, the pH/D-dependent solvent kinetic isotope effects (SKIE) for these reactions were interrogated. However, before these experiments can be presented, it is necessary to discuss some fundamental control experiments first.

For dioxygenase reactions, oxygen is a co-substrate and thus it is important to verify that atmospheric O_2-concentration is sufficient to saturate enzyme kinetics for all substrates utilized in solvent isotope experiments. Fortunately, this experiment has already been performed for the above substrates (***3mpa***, ***cys*** and ***ca***).[110] In this work, it was demonstrated that the steady-state reaction rate for *Av* MDO at saturating substrate concentration is independent of oxygen within the range of 50-400 μM. This indicates that the apparent K_M^{O2} (for all substrates) must be substantially lower (~10x) than the lowest value of oxygen used (50 μM).[86, 112] Therefore, any differences observed in *Av* MDO reactivity cannot be attributed to incomplete O_2-saturation. This also means that the reaction of the substrate-bound *Av* MDO with oxygen can be considered irreversible.

An additional factor to consider is the '*coupling efficiency*' of the enzyme. The efficiency at which an oxygenase enzyme incorporates one mole of O_2 into the product is commonly referred to as '*coupling*'. As k_{cat} represents the zero-order limit of catalysis, the coupling efficiency for a dioxygenase can be obtained from the ratio of the k_{cat} as measured from product formation divided by the k_{cat} obtained from O_2-consumption. It was previously reported that *Av* MDO reactions using either ***3mpa*** (102 ± 8%) or ***cys*** (97 ± 6%) as a substrate were nearly fully coupled over the accessible pH range of the enzyme [$6 < pH < 9$].[110] By contrast, reactions utilizing ***ca*** as a substrate exhibited significantly lower coupling (40 ± 9 %). Regardless of substrate, the coupling efficiency of *Av* MDO was not influenced by D_2O. Uncoupled reactions can result in the promiscuous release of reactive oxygen species such as H_2O_2, $O_2^{\bullet -}$, and $^{\bullet}OH$, which can complicate interpretation of these experiments. For this reason, the pH/D-dependent solvent isotope studies are focused on *Av* MDO substrates ***3mpa*** and ***cys***, which exhibit stoichiometric coupling.

Insight into ionizable groups involved in catalysis can be obtained by measuring solvent isotope effects on the pH/D-dependence of both k_{cat} and k_{cat}/K_M. The influence of pH on *Av* MDO catalysis was measured over the accessible pH range of the enzyme ($6 < pH < 9$). **Figure 2** illustrates the log(k_{cat})-pH (**A**) and log(k_{cat}/K_M)-pH profiles (**B**) obtained from the initial rate data of *Av* MDO reactions using ***3mpa*** (H_2O, *white circle*) as a substrate. For comparison the log(k_{cat})-pD and log(k_{cat}/K_M)-pD profiles obtained for ***3mpa*** reactions are also included (*black circles*). Each point within these data sets was obtained by fitting the steady-state kinetic results observed at a fixed pL-value to the standard Michaelis-Menten equation. The error in each kinetic parameter obtained (k_{cat} and k_{cat}/K_M) from these fits is indicated graphically using error bars.

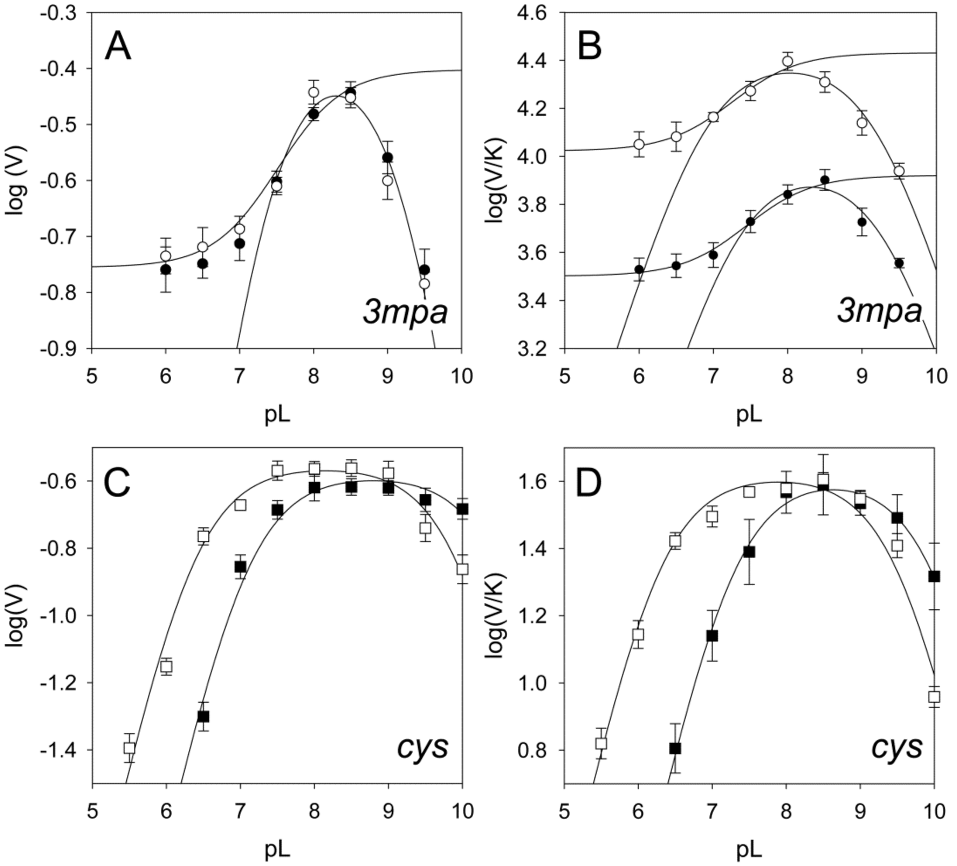

Figure 3-2: pL-dependence of steady-state kinetic parameters of MDO using 3-mercaptopropionic acid (circle, **A/B**) and *L*-cysteine (square, **C/D**) as substrates. For both substrates, log(*V*) and log(*V*/*K*) pL-profiles were collected in H_2O (*white*) and D_2O (*black*) and fit to **eq**. **1** and/or **eq**. **2**. A summary of the results obtained from these fits are summarized in **Table 1**.

In reactions using ***3mpa*** as substrate, both pH-profiles [k_{cat}-pH and k_{cat}/K_M-pH] exhibit a skewed 'bell shaped' curve with two apparent pKa values. Within the acidic branch of this profile [6 < pH < 8], both k_{cat} and k_{cat}/K_M follow sigmoidal behavior with limiting values at high and low pH. In this pH range, each data set can be reasonably fit to equation **1** (*solid line*). The limiting values of k_{cat} spans 0.19 ± 0.02 s^{-1} (Y_L) to 0.44 ± 0.05 s^{-1} (Y_H) at 20 °C. Likewise, the limiting values for k_{cat}/K_M within the sigmoidal region lie between 9,000 ± 180 $M^{-1}\cdot s^{-1}$ and 25,500 ± 240

$M^{-1}\cdot s^{-1}$, respectively. Relative to H_2O reactions, the observed k_{cat} values are unaffected for *Av* MDO assays carried out in D_2O (**Fig**. **2**, **A**). By contrast, a significant decrease in k_{cat}/K_M is observed for ***3mpa*** reactions carried out in D_2O (**Fig**. **2**, **B**). The sigmoidal limits of k_{cat}/K_M-values in D_2O lie between 3,500 ± 110 $M^{-1}\cdot s^{-1}$ and 9,000 ± 130 $M^{-1}\cdot s^{-1}$, respectively.

If the acidic branch of the curve is omitted, both ionizable groups (pKa_1 and pKa_2) can be obtained by fitting data within the inverted bell curve region [$7 < pH < 9$] to equation **2** as described elsewhere. [110] From this analysis, the pKa values (pKa_1, 7.7 ± 0.1) and (pKa_2, 9.3 ± 0.5) were obtained from the ***3mpa*** k_{cat}-pH profile in H_2O. Similarly, two pKa values (pKa_1, 6.9 ± 0.2) and (pKa_2, 9.2 ± 0.1) were obtained from the ***3mpa*** k_{cat}/K_M–pH profile. As with H_2O reactions, two ionizable groups are also observed in *Av* MDO D_2O assays using ***3mpa*** as a substrate. In fact, the log(k_{cat})-pD profile obtained is essentially super imposable with the results obtained in H_2O. Thus, the presence of D_2O has no influence on the pKa-values obtained from k_{cat} data. By contrast, both pKa values (pKa_1, 7.4 ± 0.2) and (pKa_2, 9.3 ± 0.1) obtained from log(k_{cat}/K_M)-pD fits are shifted more basic by $\Delta pKa_1 = + 0.5$ and $\Delta pKa_2 = + 0.1$, respectively. This behavior is typically observed for ionizable groups involved with catalysis.[97, 98]

The pL-profile for *Av* MDO catalyzed reactions utilizing ***cys*** as substrate (**Fig**. **2**, **C** and **D**) exhibit a clear '*bell shaped*' behavior, which can be fit by equation **2**. In ***cys*** reactions carried out in H_2O, two pKa values (pKa_1, 6.3 ± 0.1) and (pKa_2, 10.0 ± 0.1) were obtained from log(k_{cat})-pH fits. As with ***3mpa*** reactions, no significant perturbation is observed in the value of k_{cat} in H_2O (0.28 ± 0.02 s^{-1}) as compared to that obtained in D_2O (0.26 ± 0.02 s^{-1}). However, the pKa-values are shifted up to 7.1 ± 0.1 ($\Delta pKa_1 = +0.8$) and 10.5 ± 0.2 ($\Delta pKa_2 = +0.5$) in D_2O. Similarly, log(k_{cat}/K_M)-pH fits of *Av* MDO catalyzed ***cys*** reactions carried out in H_2O yield two pKa values (pKa_1, 6.3 ± 0.1) and (pKa_2, 9.5 ± 0.1) with no disenable solvent isotope effect. The observed pKa-values obtained from log(k_{cat}/K_M)-pD fits of ***cys*** reactions are also shifted upward to (7.3 ± 0.1, $\Delta pKa_1 = +1.0$) and (10.0 ± 0.2, $\Delta pKa_2 = +0.5$) in D_2O. A summary of the all pH/D-dependent kinetic results is provided in **Table 1**.

For each substrate utilized (***3mpa*** and ***cys***), the solvent kinetic isotope effect (SKIE) on each steady-state kinetic parameters (k_{cat} and k_{cat}/K_M) was determined within the pH/D-independent region of each pL-profile. For example, the k_{cat}/K_M-pL-profile for ***3mpa*** (**Fig**. **2B**) exhibits two pH-independent regions (pL ~ 6.0 and 8.2), both of which exhibit a solvent kinetic isotope effect of 2.82 ± 0.11. This value is significantly larger than possible if solely attributed to differences in the relative viscosity of a D_2O solution as compared to H_2O. Nevertheless, additional viscosity experiments are presented below to determine if the attenuation of the k_{cat}/K_M-values obtained in ***3mpa*** reactions carried out in D_2O has contributions from viscosity effects. Alternatively, as illustrated in **Fig**. **2C** and **D**, neither k_{cat}-pL nor k_{cat}/K_M-pL profiles for *Av* MDO catalyzed ***cys*** reactions exhibit solvent isotope effects beyond experimental error. Similarly, while the full pD-dependence was not determined for *Av* MDO catalyzed ***ca*** reactions; solvent isotope effects were not observed for either k_{cat} or k_{cat}/K_M in assays using ***ca*** as a substrate at pL 6.0 or 8.2.

Proton inventories

Proton inventory experiments were performed to provide greater insight into the observed solvent isotope effect on k_{cat}/K_M for *Av* MDO catalyzed ***3mpa*** reactions. In these experiments, both steady-state kinetic parameters (k_{cat} and k_{cat}/K_M) were determined for various molar ratios of H_2O and D_2O at both pH/D-independent points (pL ~ 6.0 and 8.2). For each mole fraction of D_2O measured, the value of k_{cat}/K_M observed ($[V/K]_n$) is normalized for the value obtained in pure H_2O ($[V/K]_0$). As illustrated in Fig. 3, the relative change in k_{cat}/K_M ($[V/K]_0/[V/K]_n$) decreases with increasing D_2O mole fraction. Proton inventory experiments performed at pL 6.0 (*black triangles*) and pL 8.2

(*white triangles*) exhibit nearly equivalent behavior indicating that there is no change in the number of rate limiting protonation steps at either the low or high branch of the pL-profile. Assuming a single proton in flight (*solid line*, $y = 1$), the best fit the observed proton inventory data to equation (3) was obtained for a solvent isotope effect of 2.63 ± 0.68 ($R^2 = 0.96_6$). Within error, this is in good agreement with the value determined from the k_{cat}/K_M-pL profile (2.7 ± 0.4). This observation suggests a single solvent exchangeable proton is in flight prior to the first irreversible step. Further, the equivalence of proton inventories within each pL-independent limb (6.0 and 8.2) implies that the ionizable group associated with pKa_1 is not the source of the rate-limiting proton.

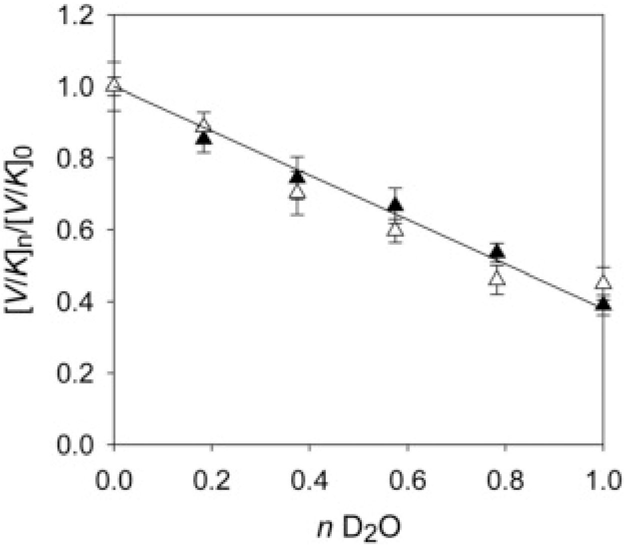

Fig.3-3: Proton inventory of MDO catalyzed formation at pL 6.0 (*black triangle*) and 8.2 (*white triangle*). Plot of normalized *V*/*K* ($[V/K]_n/[V/K]_0$) versus mole fraction D_2O (n). Experimentally determined SKIE values for k_{cat}/K_M were used to fit data to equation (3). Proton inventory data were fit assuming a single proton in flight (*solid line*, $y = 1$). Fitting results: ${}^{D2O}V/K = 2.63 \pm 0.68$, $y = 1$, $R^2 = 0.96_6$.

3.3. Viscosity effects

The possibility that diffusion controlled events such as substrate and/or product movement into and out of the active site limit the rate of catalysis was evaluated by measuring the perturbation of steady-state parameters (k_{cat} and k_{cat}/K_M) as a function of solvent viscosity. Measurements were made at pH 8.2 as described in *Material and Methods*. For each assay, sucrose was added to increase the relative viscosity of the reaction buffer and the results were fit to equation (4). Fig. 4 illustrates the relative perturbation to k_{cat} (or k_{cat}/K_M) obtained for reactions in the absence of viscosigen (k_0) normalized for the values obtained at selected relative viscosities (k_n). Assays using ***3mpa*** and ***cys*** as a substrate for *Av* MDO are shown in Fig. 4 panels **A** and **B**, respectively. The dashed lines represent the theoretical limits of this experiment. A positive slope of 1.0 is expected if catalysis is fully diffusion-limited by non-chemical steps in catalysis. Alternatively, the horizontal line represents the expected result in the absence of any diffusional limitation. The absence of any appreciable influence of solvent viscosity on k_{cat} or k_{cat}/K_M for either substrate (***3mpa*** or ***cys***) clearly demonstrates that *Av* MDO catalysis is not limited by either substrate binding or product release. Moreover, this result verifies that the increased viscosity of D_2O buffers does not contribute to the observed SKIE for *Av* MDO k_{cat}/K_M data obtained in ***3mpa*** reactions.

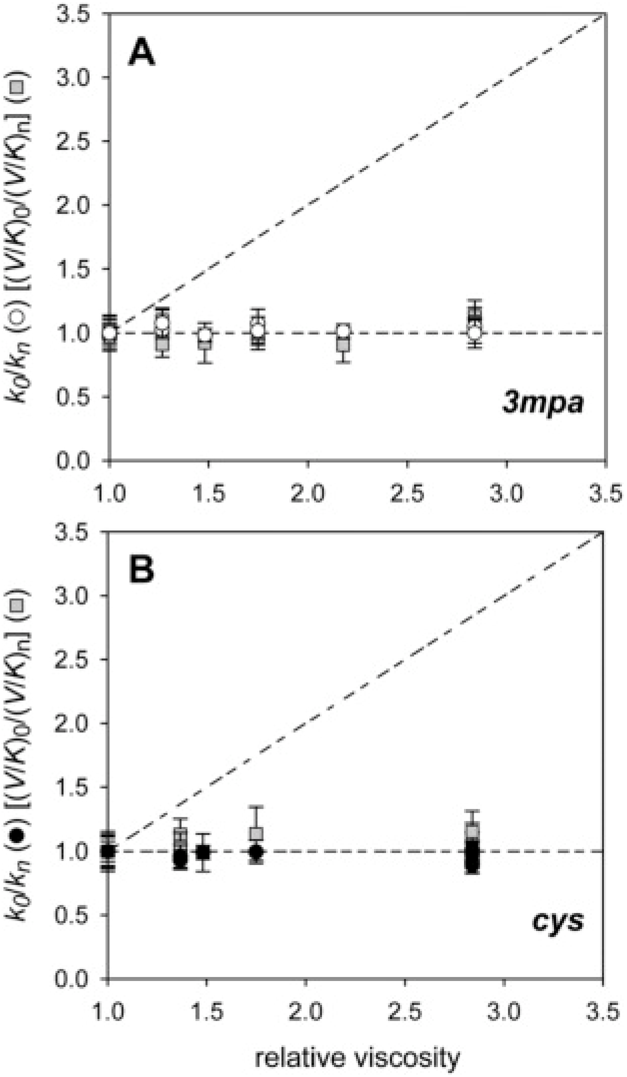

Fig. 3-4: Effect of solvent viscosity on the maximal rate (v_0/[E]) of MDO catalyzed ***3spa*** and ***csa*** formation. **A**. The effect of solvent viscosity on k_{cat} (k_0/k_n) and k_{cat}/K_M [$(V/K)_0/(V/K)_n$] for ***3spa*** formation is designated by circles (*white*) and squares (*gray*), respectively. **B**. For comparison, the effect of solvent viscosity on k_{cat} [(k_0/k_n), *black circle*] and [$(V/K)_0/(V/K]_n$, *gray square*) for ***csa*** formation was also measured as a function of viscosity. The dashed lines represent the theoretical limits for diffusion-limited product release.

4. Discussion

Among thiol dioxygenase enzymes, the mammalian 'Arg-type' CDO has been extensively characterized spectroscopically,[53, 76, 114, 115] crystallographically,[60, 71, 116] and kinetically.[73, 79, 82]However, almost no information is available regarding the relative timing of chemical and non-chemical steps in 'Gln-type' MDO catalyzed reactions. A significant point of divergence between CDO and MDO is with respect to substrate coordination to the mononuclear Fe-site. EPR spectroscopic studies indicate that substrate coordination to the *Av* MDO Fe-site is via thiolate-only.[110] By contrast, all known 'Arg-type' CDO enzymes bind ***cys*** via bidentate coordination of substrate-thiolate and neutral amine. This difference in Fe-coordination likely explains the relaxed substrate specificity reported among 'Gln-type' thiol dioxygenase enzymes.[108, 110] Therefore, this subset of enzymes offers a unique point of comparison to better understand the significance of the first- and outer Fe-coordination sphere on catalysis and substrate-specificity among thiol dioxygenase enzymes.

For diffusion-controlled reactions in which product release is rate-limiting, k_{cat} would be attenuated by increased solvent viscosity. Since addition of D_2O to reaction buffers increases the relative viscosity of reaction mixtures, it is possible that viscosity effects contribute to the apparent solvent isotope effect. However, the results shown in Fig. 4 clearly demonstrate that, regardless of substrate, solvent viscosity has no impact on either k_{cat} or k_{cat}/K_M. These experiments verify that non-chemical diffusional steps (*product release* and/or *substrate binding*) are not rate-limiting for *Av* MDO catalyzed reactions with ***3mpa*** or ***cys***. By contrast, product release in *Mm* CDO is partially rate-limiting.[85] However, substrate (*and potentially product*) coordination for CDO is bidentate, the resulting chelate effect likely stabilizes both the **ES-** and **EP**-complex. By contrast, substrate binding to the *Av* MDO Fe-site is believed to be via thiolate only, and thus product release is expected to be faster by comparison.

Within the experimental pH range of $6 < \text{pH} < 8.5$, both k_{cat}- and k_{cat}/K_M-pH profiles for *Av* MDO reactions using ***3mpa*** as a substrate exhibit nonzero limiting values. Only at pH values beyond ~9 does the activity of *Av* MDO decrease linearly toward zero. By contrast, both k_{cat}-pH profiles for enzymatic reactions using substrates bearing an amino functional group (***cys*** and ***ca***) decrease to zero within the acidic limb of the profile.[110]These observations are key to the development of a MDO kinetic model.

The pH-dependent behavior observed in ***3mpa*** reactions can be rationalized assuming a diprotic model in which three ionic forms of the enzyme are present but only two of them are catalytically active.[99, 117] As illustrated in Scheme 1, three ionic forms of the enzyme are produced by either protonation of the neutral enzyme (designated $\mathbf{E^{z}}$) to form the cationic $\mathbf{E^{(z+1)}}$ enzyme or deprotonation to yield the anionic $\mathbf{E^{(z-1)}}$ form. The pH-dependent profile for ***3mpa*** reactions suggest that both $\mathbf{E^{z}}$ and $\mathbf{E^{(z+1)}}$ are catalytically active with rates reflected by the asymptotic limits of k_{cat} within the acidic branch of the pH-profile (27,000 and 10,000 $M^{-1}\ s^{-1}$, respectively). However, the doubly deprotonated enzyme is either unable to bind ***3mpa*** or cannot reductively activate oxygen to generate product. Either way, the $\mathbf{E^{(z-1)}}$ ionic form is catalytically inactive in ***3mpa*** assays.

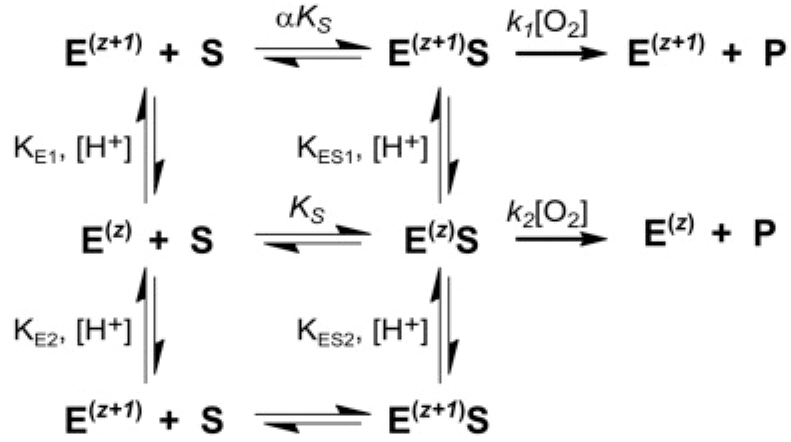

Scheme 3-1. Proposed kinetic mechanism for *Av* MDO catalyzed ***3mpa*** reaction.

In the context of the reaction scheme proposed, the observed pKa values in k_{cat}- [pKa$_1$ = 7.4 ± 0.2; pKa$_2$ = 9.1 ± 0.1] and k_{cat}/K_M-pH profiles [pKa$_1$ = 7.8 ± 0.2; pKa$_2$ = 9.2 ± 0.1] are attributed to catalytically essential ionizable amino acids within the free enzyme[86]. Further, the significant solvent isotope effect (2.7 ± 0.4) observed for ***3mpa***k_{cat}/K_M data suggests that proton-dependent steps play an important role in the initial reversible steps leading up to O_2 binding.

Unambiguous identification of the specific ionizing amino acid residue associated with each pKa-value is not possible without direct comparison to *Av* MDO active site variants. While such experiments are currently ongoing, a reasonable mechanistic hypothesis can be formulated based on: (**1**) the pKa-values observed in k_{cat}- and k_{cat}/K_M-data, (**2**) steady-state results obtained previously for H155A and Y157F *Mm* CDO variants, (**3**) and computationally validated EPR and CD/MCD studies.[72, 118]

The crystal structure for *Av* MDO is not available; however, structural comparisons can be made to the *Pseudomonas aeruginosa* ‘Gln-type’ MDO (PDB code 4TLF) which shares 69.5% sequence identity (84.8% *similarity*) with *Av* MDO.[108] As noted previously, the active site of *Mm* CDO is essentially equivalent to MDO with the notable exception of the C93-Y157 pair and R60 (replaced by Q62 in MDO). The pKa-values observed in ***3mpa***k_{cat}- and k_{cat}/K_M-pL profiles (7.4–7.8), along with the ΔpKa (+0.4) observed in D_2O reactions, is consistent with values reported for catalytically essential histidine residues. As illustrated in Fig. 1, all known thiol dioxygenase enzymes have four conserved histidine residues within the active site. Three of which compose the Fe-coordination site (H89, H91 and H142 for *Pa* MDO, Fig. 1B). Protonation of any of these residues would result in loss of iron and inactivation of the enzyme. Since activity is not abolished below pKa_1 in ***3mpa*** reactions, it can be concluded that these residues are not protonated. This leaves only the conserved His-residue (H157) for further consideration.

The hypothesis that pKa_1 corresponds to H157 is attractive since it has been demonstrated previously that the equivalent residue in *Mm* CDO (H155) is critical for enzymatic activity. Indeed, despite comparable ferrous iron incorporation, the specific activity of the H155A *Mm* CDO variant is decreased by ~ 2-orders of magnitude relative to the wild-type enzyme.[78] Furthermore, recent spectroscopic (CD/MCD), crystallographic and computational studies of the *Mm* CDO H155A variant suggests that H155 serves as a hydrogen bond donor for the Y157 phenol group, thereby positioning the Y157 hydroxyl group of the C93-Y157 pair optimally to donate a hydrogen bond to the Fe-bound ***cys***-carboxylate.[98, 118] Assuming a similar function in the bacterial enzyme, the conserved H157 residue in *Pa* MDO would be expected to donate a hydrogen bond to the O-atom of the Y159 hydroxyl group to promote interaction with the substrate-carboxylate. This hypothesis presents an attractive explanation for the role of the '*catalytic triad*' of Ser-His-Tyr residues universally conserved among thiol dioxygenases.[118] In this model, the hydroxyl group of S155 donates a hydrogen bond to the N_ε-atom of H157 to align the opposite N_δ-atom for hydrogen bond donation to the O-atom of the Y159 phenol group. Protonation of H159 would disrupt this hydrogen bond network and result in formation of a positive charge within the enzymatic active site pocket resulting in attenuation of enzymatic activity below pKa_1.

By extension, the basic pKa_2-value observed in ***3mpa*** reactions is close to values typically associated with tyrosine residues (pKa ~10). Furthermore, despite stabilizing a ferrous iron resting state, the Y157F (equivalent to Y159 of *Pa* MDO) variant of *Mm* CDO is catalytically inactive, thereby establishing that this residue is also essential for native catalysis.[78] Computational studies validated by EPR spectroscopy confirm that the hydroxyl-group of Y157 within the *Mm* CDO active site directly interacts with the carboxylate-group of the Fe-bound substrate (***cys***).[82] It is therefore reasonable to expect that Y159 of MDO is the second ionizable group observed in ***3mpa*** pL-profiles. A schematic representation summarizing the proposed substrate-bound ionic enzymes forms [$\mathbf{E^{(z+1)}S}$, $\mathbf{E^{z}S}$ and $\mathbf{E^{(z-1)}S}$] is shown in Scheme 2.

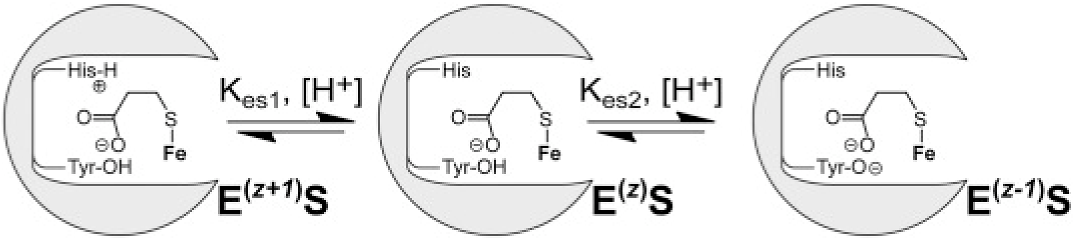

Scheme 3-2. Proposed substrate-bound ionic enzymes forms [$\mathbf{E^{(z+1)}S}$, $\mathbf{E^{z}S}$ and $\mathbf{E^{(z-1)}S}$].

Since both pKa-values are observed in k_{cat}- and k_{cat}/K_M-pH profiles, it can also be argued that a proton-dependent step is involved in the chemical steps.[86] However, this can also be rationalized in the context of the proposed ionic enzyme forms produced as a function of pH.

As with most non-heme oxidase/oxygenase enzymes, binding and reductive activation of molecular oxygen is gated by substrate coordination to the Fe-site.[110] While the precise mechanism remains a matter of considerable debate, it has been proposed that the coordination of substrate to the Fe-site alters the Fe^{II}/Fe^{III} redox couple and/or induces key conformational changes that facilitate direct O_2-coordination and activation.[7, 6, 8] Thus, charge stabilization and geometry of the substrate-bound Fe-site are critical for enzymatic activity.

In the doubly deprotonated $\mathbf{E^{(z-1)}}$ form, electrostatic repulsion between the Y159-tyrosinate and ***3mpa*-**carboxylate group would significantly inhibit substrate binding to the opposite face of the 3-His facial triad. For perspective, the distance separating Y159 O-atom and the Fe-bound solvent **W3** is 2.67 Å [Fig. 1B]. The short distance separating two negative charges would produce a significant columbic force, likely resulting in both geometric and electrostatic distortions at the substrate-bound Fe-site. Whether the anionic $\mathbf{E^{(z-1)}}$ form cannot bind ***3mpa*** or the $\mathbf{E^{(z-1)}S}$ complex is unable to activate oxygen; the result is the same, abolishment of enzymatic activity beyond pKa_2. This hypothesis also provides an explanation for the absence of a basic pKa in k_{cat}-pH profiles obtained in assays using ***ca*** as a substrate.[110] Unlike ***3mpa*** and ***cys***, cysteamine lacks a carboxylate group. Since there is no electrostatic repulsion between the substrate and the anionic $\mathbf{E^{(z-1)}}$ enzyme, neither substrate-binding nor subsequent O_2-activation are attenuated under basic conditions. Furthermore, the retention of $\mathbf{E^{(z-1)}}$ activity in reactions utilizing ***ca*** demonstrates that the second protonation step does not irreversibly inactivate MDO.

Similarly, the differential pH-dependent behavior exhibited within the acidic limb of ***3mpa*** reactions as compared to substrates bearing a positively charged quaternary amine (***cys*** and ***ca***) can also be explained by this kinetic mechanism. As noted previously, both k_{cat} and k_{cat}/K_M decrease for *Av* MDO catalyzed ***3mpa*** reactions, but activity is not abolished within the acidic limb of the pH profile. Conversely, steady-state parameters approach zero for ***cys*** and ***ca*** enzymatic reactions below pKa_1. Protonation of H157 would produce a cationic $\mathbf{E}^{(z+1)}$ enzyme form. The positive charged imidazole ring of H157 is positioned along the substrate-binding face of the 3-His facial triad (3.90 Å distance from the Fe-bound solvent molecule **W3**). Therefore, cationic substrates such as ***cys*** and ***ca*** would experience considerable electrostatic repulsion under acidic conditions. Finally, the zwitterionic ***cys*** substrate has both amine- and carboxylate-groups, thus only the neutral $\mathbf{E}^{z}$ enzyme form retains activity, whereas the ionic $\mathbf{E}^{(z+1)}$ and $\mathbf{E}^{(z-1)}$ forms are inactive. As expected, this results in an inverted '*bell shaped'* curve in k_{cat}-pH profiles.

Chapter 4

Formation of benzothiazoles from 2-mercaptoaniline and oxygen-dependent oxidation of primary alcohols by Thiol dioxygenase enzymes

Introduction

Cysteine dioxygenase is a non-heme mononuclear iron enzyme that catalyzes the O_2-dependent oxidation of *L*-cysteine (***cys***) to produce cysteine sulfinic acid (***csa***). Only two mammalian thiol dioxygenases have been identified to date, cysteine dioxygenase (CDO) and cysteamine (2-aminoethanethiol) dioxygenase (ADO). Among these, CDO is the best characterized.[51, 56, 61, 106, 107] Intracellular ***cys*** concentration is limiting in glutathione synthesis, therefore the activity of CDO directly competes with cellular redox buffering under conditions of low ***cys*** availability and oxidative stress.[119] Abnormal ***cys*** metabolism has been observed in patients suffering from a variety of neurological diseases,[56, 67, 68] suggesting a correlation between impaired sulfur metabolism, oxidative stress, and neurodegenerative disease.[69,70] Consequently, enzymes involved in sulfur-oxidation and transfer are increasingly being recognized as potential drug targets for development of antimicrobials, therapies for cancer and inflammatory disease.[63, 64, 65, 66]

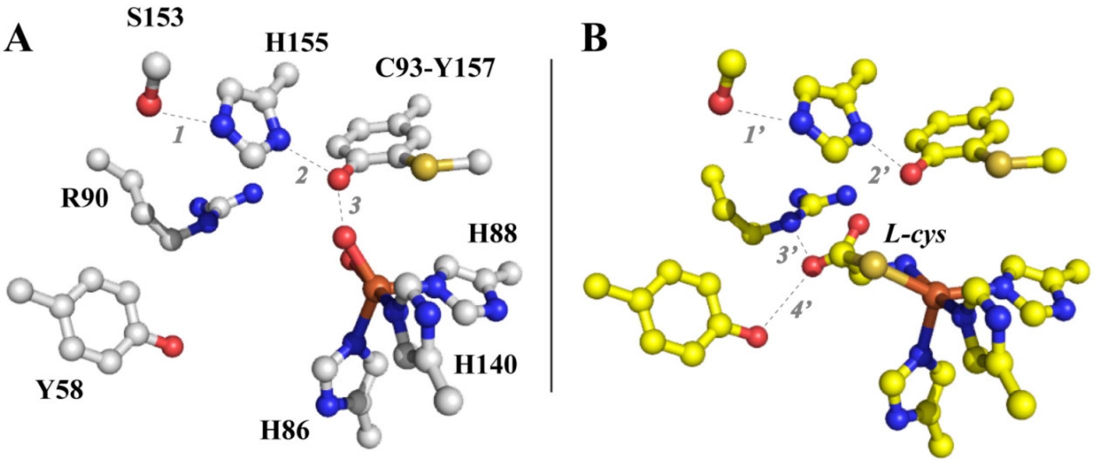

Figure 4-1. Crystal structure of the *Rattus norvegicus* CDO active site (**A**, pdb code 4IEV) as compared to the substrate-bound enzyme (**B**, pdb code 4IEZ).[120] Selected distances **A**: ***1*** (2.63 Å); ***2*** (2.73 Å); ***3*** (2.72 Å); **B**: ***1'*** (2.78 Å); ***2'*** (2.82 Å); ***3'*** (2.91 Å); and ***4'*** (3.10 Å).

Shown in **Figure 4-1** is the crystal structure for the *Rattus norvegicus* CDO (pdb code 4IEV) active site.[120] The iron first coordination sphere is comprised of iron ligated along one octahedral face by the N_ε-atoms of H86, H88, and H140. Prior to the addition of O_2, ***cys*** coordinates to the mononuclear ferrous site of CDO in a bidentate fashion through a thiolate and neutral amine.[53, 60, 76] As illustrated in **Fig**. **1B**, ligation of the ***cys*** thiol-group within the trigonal plane opposite H86 and H88 positions the carboxylate group of ***cys*** favorably for charge stabilization by the R60 guanidinium group.

It was previously demonstrated that the catalytic cycle of CDO can be '*primed*' by 1-electron through chemical oxidation to produce CDO with ferric iron in the active site.[54] While catalytically inactive, the substrate-bound form of Fe^{III}-CDO is more amenable to interrogation by UV-visible and EPR spectroscopy than the '*as-isolated*' Fe^{II}-CDO enzyme. Chemical-rescue experiments were performed in which superoxide ($O_2^{\bullet-}$) was introduced to the substrate-bound Fe^{III}-CDO to produce and characterize by EPR and UV-visible spectroscopy a transient intermediate kinetically matched to ***csa*** formation. This intermediate was tentatively assigned as a substrate-bound Fe^{III}-superoxide species similar to that spectroscopically observed for the extradiol cleaving catechol dioxygenase, homoprotocatechuate 2, 3-dioxygenase, (2, 3-HPCD).[16, 19] While the decay of this intermediate was kinetically matched to the formation of product, the rate of ***csa*** produced was significantly slower than the steady-state turnover for *Mm* CDO. It is therefore not clear if this represents a catalytically relevant intermediate. More recently, stopped-flow UV-visible studies identified a transient species upon rapid mixing of the substrate-bound CDO with saturating oxygen. Supporting computational modeling of the transient UV-visible spectra suggest that this transient species is consistent with a cyclic [Fe-O-O-S_{Cys}]-structure with a quintet (S = 2) spin state. However, rapid freeze-quench Mössbauer experiments were unable to corroborate this assignment.[121] Therefore, direct spectroscopic validation of the transient intermediate produced during native catalysis is absent.

Catechol dioxygenases are key metabolic enzymes found within soil bacteria having the capacity to degrade aromatic compounds, which can be utilized as a carbon source.[122, 123] These enzymes are classified into two primary families based on the position of substrate ring cleavage and oxidation state of the catalytically essential iron within the non-heme active site. For instance, intradiol dioxygenase enzymes such as catechol 1, 2-dioxygenase (CTD) and protocatechuate 3, 4-dioxygenase (3, 4-PCD) catalyze the O_2-dependent carbon-carbon bond cleavage between the substrate phenolic hydroxyl groups to yield a dicarboxylic acid muconate product. This class of enzymes stabilizes a ferric iron (Fe^{III}) resting state, which activates the substrate for electrophilic attack by oxygen. It has been proposed that the high activation barrier for direct O_2-attack on the substrate is overcome by resonance delocalization of unpaired spin-density onto the substrate from the substrate-bound high-spin ferric site to facilitate a spin-allowed reaction with triplet O_2.[19, 122]

Alternatively, extradiol dioxygenases such as the aforementioned 2, 3-HCPD cleave the carbon-carbon bond adjacent to the ortho-hydroxyl groups to yield 5-carboxymethyl-2-hydroxymuconic semialdehyde. These enzymes stabilize a resting ferrous iron (Fe^{II}), or in rare instances Mn^{II}, in the active site to activate molecular oxygen for subsequent attack on the substrate.[124] For these enzymes, reversible binding of the catechol substrate precedes O_2-binding at the substrate-bound ferrous active site. Oxidative addition of O_2 to the ferrous iron yields a short-lived ferric-superoxo [Fe^{III}-$O_2^{\bullet-}$] species ultimately responsible for nucleophilic attack on the aromatic substrate.[125]

Assuming both 2, 3-HPCD and CDO produce a Fe^{III}-superoxo intermediate prior to substrate oxidation, it is possible that additional mechanistic parallels exist in reactions utilizing aromatic substrates. Steady-state specificity experiments with the *Mus musculus* CDO (*Mm* CDO) demonstrated that the minimal substrate for CDO must contain both amine and thiol functional groups, and that optimal activity and efficiency is observed when these groups are separated by two carbon units.[109] With this in mind, 2-mercaptoaniline (***2ma***) could provide an interesting comparison to the aforementioned catechol dioxygenase class of non-heme mononuclear iron enzymes. It should be noted that the bonds separating the thiol and amine functional groups in the aromatic ***2ma*** substrate are sp^2 hybridized. As these bonds cannot be rotated to the extent of aliphatic thiols, the ***2ma***-bound Fe-site geometry is expected to be significantly perturbed relative to the native **ES**-complex. Another factor to consider is the differential reactivity of aromatic versus aliphatic thiols. Potentially, these deviations may result in unique reactivity.

Neglecting potential hydrolysis, cyclization, or tautomerisation, **Scheme 1** illustrates the expected reaction products for analogous *thiol dioxygenase, extradiol-, or intradiol* cleaving activity.

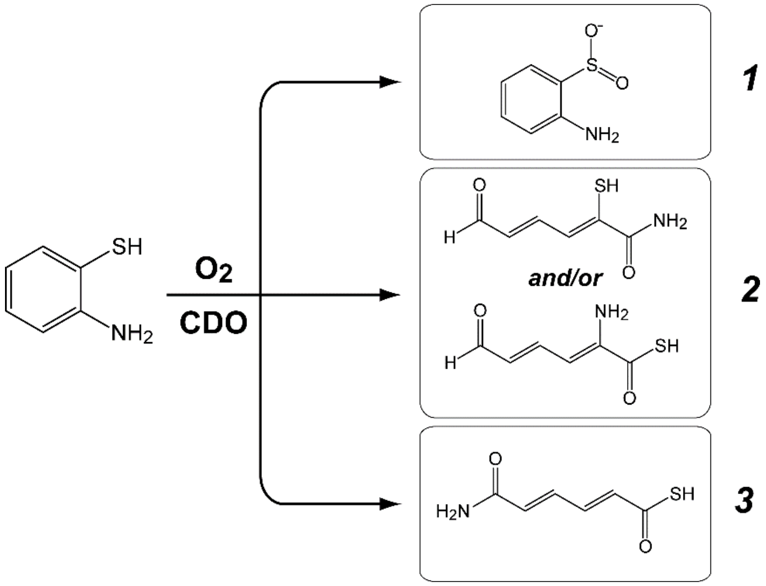

Scheme 4- 1: Potential reaction products for O_2-dependent ***2ma*** oxidation catalyzed by *Mm* CDO assuming (***1***) thiol dioxygenase [aminobenzenesulfinic acid], (**2**) extradiol dioxygenase- [2-mercapto-6-oxohexa-2, 4-dienamide or 2-amino-6-oxohexa-2, 4-dienethioic S-acid], or (***3***) intradiol dioxygenase cleaving activity [6-amino-6-oxohexa-2, 4-dienethioic S-acid].

Presented here are the results of O_2-dependent ***2ma*** reaction using two different thiol dioxygenase enzymes [*Mm* CDO and 3-mercaptopropionic acid dioxygenase isolated from *Azotobacter vinelandii* (*Av* MDO)]. These enzymes bind substrates bidentate[53, 60, 76] and monodentate,[110, 118] respectively and thus may exhibit differential reactivity.

Materials and Methods

Enzyme purification.

Recombinant *Mus musculus* cysteine dioxygenase *(Mm CDO) and Azotobacter vinelandii* 3-mercaptopropionic acid dioxygenase (*Av* MDO) were expressed, purified, and activity verified as described previously.[79,110] For all batches of enzyme used in these experiments, spectrophotometric determination of ferrous and ferric iron content was measured using 2, 4, 6-tripyridyl-s-triazine (TPTZ). A detailed description of this method is presented elsewhere.[76, 110] For clarity, the concentrations reported in enzymatic assays reflect the concentration of ferrous iron within enzyme samples. The protein content in each sample was determined by Bio-Rad protein assay. Steady-state kinetic parameters observed at 20 ° C for *Mm* CDO and *Av* MDO were consistent with previously published values (*Mm* CDO; k_{cat}, 0.7 ± 0.1 s^{-1}; K_M, 2.1 ± 0.3 mM; k_{cat}/K_M, 330 ± 50 M^{-1} s^{-1}; *Av* MDO; k_{cat}, 0.5 ± 0.1 s^{-1}; K_M, 18 ± 2 μM; k_{cat}/K_M, 28,000 ± 3000 M^{-1} s^{-1}).[110, 118]

Reagents and stock solutions.

2-mercaptoaniline (***2ma***) (99%) was purchased from Sigma-Aldrich (cat. no. 274240) and stored under argon within an anaerobic chamber to prevent disulfide formation. Stock solutions of ***2ma*** (0.75 mM) were prepared anaerobically in ethanol (95%, ACROS) prior to subsequent dilution in aqueous buffer (10mM HEPES, 50 mM NaCl, and pH 8.5) for enzymatic assays. The benzothiazole (***bt***) [96%, cat. no. 101338] and 2-methylbenzothiazole (***2m-bt***) [99%, cat. no. 112143] standards used for spike assays and LC-MS/MS (MRM) verification of products were purchased from Sigma-Aldrich and used without further purification. However, 2-phenybenzothiazole (***2p-bt***) was synthesized as described below. All standards were prepared by serial dilution of a *ca*. 5 mM stock solution in 80:20 (buffer:ethanol). Spike assays were performed by serial dilution of the stock solution to 1-5 μM prior to HPLC analysis.

Synthesis of 2-phenybenzothiazole (2p-bt).

Synthesis of 2-phenylbenzothiazole was performed as described elsewhere.[126] Briefly, 2-mercaptoaniline (250 mg, 2 mmol), benzaldehyde (212 mg, 2 mmol) and excess acetic acid were heated for 4 hours at reflux temperature. After cooling it to room temperature, the reaction mixture was added into an ice water mixture. The solid precipitated out was collected by suction filtration. The crude solid was crystallized from ethanol/water to give 345 mg of ***2p-bt*** in 82% yield as colorless solid.

Characterization of ***2p-bt*** product was performed by 500 MHz ^{1}H and 125 MHz ^{13}C NMR experiments performed on a JOEL Eclipse Plus 500 NMR spectrometer. Chemical shifts were recorded in reference to residual solvent peaks ($CDCl_3$ = 7.26 ppm). FT-IR spectra were recorded on a Bruker Alpha-P FT-IR Spectrometer by attenuated total reflectance on a diamond sample plate. **^{1}H NMR** (500 MHz, $CDCl_3$) δ 8.13 – 8.09 (m, 3H), 7.89 (ddd, *J* = 8.0, 1.2, 0.6 Hz, 1H), 7.53 – 7.47 (m, 4H), 7.40 – 7.36 ppm (m, 1H); **^{13}C NMR** (126 MHz, $CDCl_3$) δ 168.1, 154.2, 135.1, 133.7, 131.0, 129.1, 127.6, 126.4, 125.3, 123.3, 121.7; **IR** (Neat): 3064, 3018, 1477, 1432, 1312, 1224, 962, 757, 729. Melting point (113-114 °C) was obtained in capillary tubes on a Mel-Temp II apparatus, and the thermometer was uncorrected. These values are in agreement with those reported in the literature.[127]

UV-visible experiments.

UV-visible measurements were performed on an Agilent 8453 photo diode array spectrometer (Santa Clara, CA). Sample temperature was held constant by a 13L circulating water bath and an Agilent thermostatble cell holder (89054A) with magnetic stirrer. All measurements were made in ES Quartz cuvettes (NSG Precision Cells, Farmingdale, NY). For time dependent assays, a baseline correction at 900 nm was used. Spectra collected in kinetic mode used a 4-second interval between measurements for the first 3-minutes. Beyond this point, time intervals were increased by 5% up to 15 minutes.

In a typical UV-visible experiment, an O_2-saturated buffer [10mM HEPES, pH 8.5 at 20 °C] was diluted with anaerobic buffer and ethanol to obtain the desired O_2 concentration and 20% (*v*/*v*) ethanol (1.0 mL final volume). This solution was used to blank the UV-visible spectrometer. The stock ***2ma*** solution was then added to obtain substrate concentrations ranging from ca. 30-130 μM. Reactions were initiated by injection of enzyme (final concentration, 2 μM).

Oxygen Electrode.

Consumption of molecular oxygen was verified polarographically using a standard Clark electrode (Hansatech Instruments, Norfolk, England) in a jacketed 2.5 mL cell. Calibration of O_2-electrode is described in detail elsewhere.[79, 82] All reactions were initiated by addition of 2.0 μM enzyme (*Mm* CDO or *Av* MDO) under identical buffer conditions as described for UV-visible experiments. Reaction temperatures were maintained at 20 ± 2 °C by circulating water bath (ThermoFlex 900, Thermo Scientific).

HPLC sample preparation.

Samples were prepared for select reaction time points ranging from 1-30 minutes by removing an aliquot of the reaction (180 μL) and quenching by addition of 5 μL 2N HCl. Samples were purified by 0.22 μM cellulose acetate membrane filtration (Corning, Spin-X) prior to analysis. As a control, a zero-point sample was prepared by substituting heat-denatured enzyme in the above reaction. Unless otherwise noted, the concentration of ***2ma***, oxygen, and alcohol in reaction buffers was fixed at 150 μM, 420 μM (35% saturated), and 20% (*v*/*v*), respectively.

***HPLC instrumentation and analysis*.**

HPLC samples were analyzed using a Dionex UltiMate 3000 HPLC equipped with a 3000-variable wavelength detector. Column, Phenomenex Luna (5 µm) C18 100 Å, column [250 x 4.6 mm] with accompanying C18 [4 x 3.0 mm] guard column; mobile phase, 35:65 HPLC grade H_2O: methanol; injection volume, 20 µL; isocratic flow rate, 0.5 mL/min; column temperature, 25 °C. UV-visible detection was monitored at 270 nm. Calibration curves for ***2ma***, ***bt***, ***2m-bt***, and ***2p-bt*** were prepared for determination of product concentration. Serial dilution of benzothiazole standards exhibited a linear response in concentrations ranging from 10-1100 µM.

***LC-MS/MS (multiple reaction monitoring*).**

Verification of enzymatic product was performed by multiple reaction monitoring (MRM) using a triple quadrupole LC-MS/MS [Shimadzu Scientific Instruments, LCMS 8040][128, 129, 130]. For each experiment, 10 µL of the benzothiazole standard (*described above*) was injected to determine the product ions and relative distribution for each ion. The molecular ion $[M\text{-}H]^+$ for each specific benzothiazole standard [***bt***, 136 m/z; ***2m-bt***, 150 m/z; and ***2p-bt***, 212 m/z] was selected for secondary fragmentation in positive ion mode.[131] MRM optimization was then employed to maximize transition intensity and sensitivity for each fragment allowing for quantitation of product ions. The optimized MRM method was used to verify the formation of specific benzothiazole product ions and their relative intensities in enzymatic reactions by direct injection of assays.

GC-MS/MS sample preparation.

A standard solution of benzaldehyde was prepared by dissolving 2 µL of benzaldehyde in 500 µL of dichloromethane. The same procedure was used for making standard solution of acetaldehyde. Detection of benzaldehyde in analyte samples was performed after extraction with 500 µL dichloromethane. Detection of acetaldehyde in analyte samples was performed with direct injection of the sample, without extracting with dichloromethane. **Note**: Acetaldehyde and benzaldehyde are highly volatile and therefore all extractions were performed in the sample vial using a Hamilton gas-tight syringe to prevent loss of volatiles.

GC-MS/MS Instrumentation and Method

GC-MS experiments were conducted in Shimadzu Scientific Instruments, GCMS-QP2010, using electron impact ionization (EI) at 150 eV and a mass selective detector. The method used for detecting acetaldehyde in the GC experiment represents 0.5 min @ 50 °C – 30 °C/ min – 7.5 min @ 260 °C with injection volume of 1µL. For benzaldehyde, the GC experiment represents 1.0 min @ 50 °C – 30 °C/ min – 8.0 min @ 260 °C with injection volume of 1 µL.

Results and Discussion

CDO catalyzes the O_2-dependent oxidation of a variety of substrates which contain both amine and thiol functional groups separated by two carbon atoms. Understandably, the catalytic efficiency (k_{cat}/K_M) for substrates other than ***cys*** is poor, nevertheless product formation is easily observed at concentrations amenable to HPLC, NMR, and LC-MS/MS analysis.[109] Kinetic experiments were performed on an Agilent photodiode array spectrometer as formation of the ***2ma***-sulfinic acid product (2-aminobenzensulfinate, ***2abs***) is expected to be red-shifted relative to the starting substrate. Given the low solubility of ***2ma***, ethanol was added to the enzymatic reactions to increase the upper limit of substrate concentration in solution. As a control, equivalent *Mm* CDO assays with ***cys*** were carried in the same buffer to verify that the addition of ethanol did not abolish enzymatic activity. In assays performed in 20% (*v*/*v*) ethanol, only a modest loss (10-20%) of *Mm* CDO specific activity was observed within the time scale of the experiments (10-20 minutes).

As illustrated in **Figure 2**, introduction of enzyme results in rapid change in the UV-visible spectrum ranging from 250 to 450 nm. A single isosbestic point at 318 nm confirms the presence of at least 2 species in reaction mixtures. As illustrated in **Fig**. **S1A**, kinetic flooding experiments at fixed *Mm* CDO (2 μM) and O_2 (420 μM) exhibit a linear increase in the observed rate (v_{obs}) with increasing ***2ma*** concentration. Similarly, **Fig**. **S1B** demonstrates that v_{obs} also increases linearly with increasing enzyme concentration at fixed ***2ma*** (125 μM) and O_2 (420 μM) concentration. Finally, a linear increase in v_{obs} is also observed with increasing O_2-concentration (**Fig**. **2**, *inset*). These experiments verify that the reaction is first-order with respect to all reactants (*Mm* CDO, O_2, and ***2ma***). However, full enzymatic saturation is not observed within the ***2ma*** (30-150 μM) or oxygen (50-900 μM) concentration range utilized in these experiments. Crucially, no change in the UV-visible data is observed upon addition of heat inactivated enzyme thus verifying that this reaction is not initiated by adventitious iron within enzyme samples.

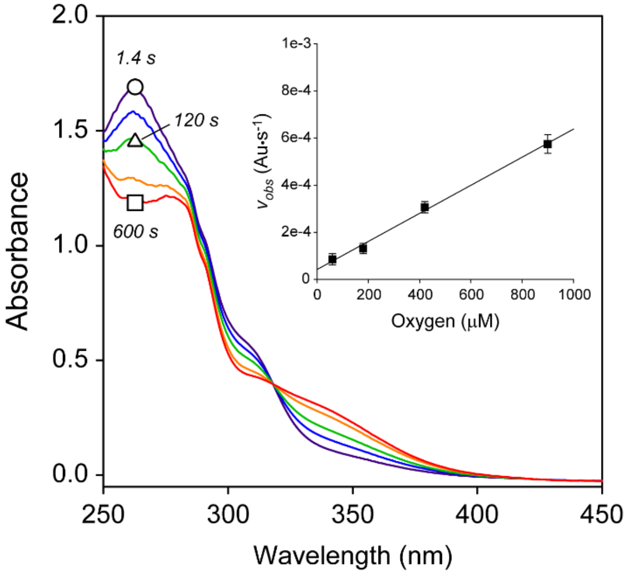

Figure 4-2. Representative UV-visible spectra illustrating the O_2-dependent reaction of 2-mercaptoaniline (***2ma***) catalyzed by *Mm* CDO. Selected time points: 1.4 s (purple trace, ○), 50 s, 120 s (green, Δ), 300 s and 600 s (red, □). Assay conditions: 2 μM *Mm* CDO, 420 μM O_2, 20% ethanol (*v*/*v*), 10 mM HEPES, pH 8.5 and 25 ± 2 °C. *Inset*. Pseudo first-order kinetics of initial rate (v_{obs}) as a function of oxygen concentration. The progress of the reaction at fixed and saturating ***2ma*** (130 μM) was monitored spectrophotometrically at 305 nm.

Consumption of oxygen was verified using a standard Clarke-type electrode. Representative O_2 electrode results are shown in *Supplementary Information* (**Figure S2**). In these studies, equivalent reactions as described above were initiated by injection of enzyme. As with UV-visible experiments, the rate of O_2-consumption increased linearly with increasing enzyme and ***2ma*** concentration. As an additional control, reactions were performed using benzenethiol as a substrate. However, neither CDO nor MDO exhibited any significant consumption of oxygen upon initiation of benzenethiol-reactions (*Supplemental Information, Figure S2*).

A translational benefit of this reaction is that ***2ma*** can be used to optically screen for thiol dioxygenase activity. As shown in **Fig**. **2**, enzymatic ***2ma***-reactions result in the formation of absorption features ~350 nm and thus a yellow color is apparent as the reaction progresses. While spectrophotometric and O_2-electrode results are useful for interrogation of the relative timing of chemical events, product analysis and assignment was performed using HPLC and LC-MS/MS as described in *Materials and Methods*. **Figure 3** shows selected HPLC traces (spectrophotometric detection at 305 nm) for reactions of *Mm* CDO with ***2ma*** in 20% (*v*/*v*) ethanol. Within this window, two peaks observed at retention times of 11.6 and 16.2 min show a clear time-dependent behavior. The 11.6 min peak decreases in intensity with time and can easily be identified as the starting ***2ma*** by the matching retention times observed in calibration curves. LC-MS (and LC-MS/MS) was run in positive detection mode using the same mobile phase, flow rate, and column to observed the molecular ion $[M-H]^+$ (150 m/z) of the species eluted with a retention time of 16.2 min. Since the expected mass for all dioxygenase products utilizing ***2ma*** is 157 Da, the 150 m/z $[M-H]^+$ species cannot be attributed to any of the reactions predicted in **Scheme 1**.

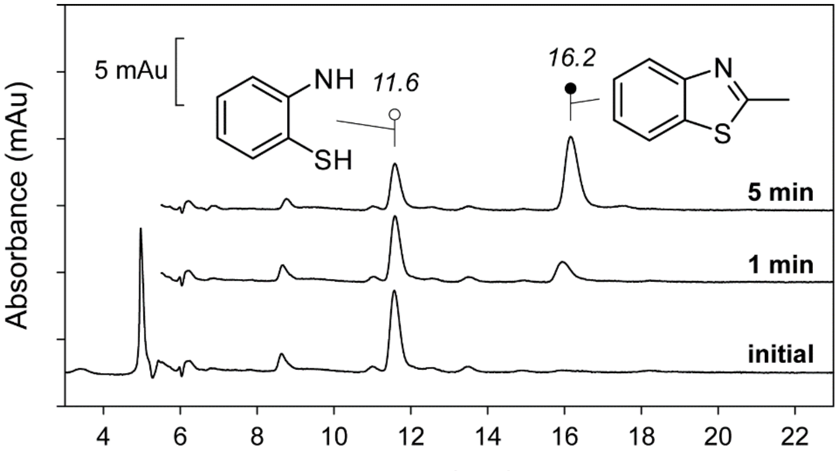

Figure 4-3. Representative HPLC chromatograms illustrating the change in analyte composition following introduction of enzyme. The initial composition of the reaction mixture is indicated by the bottom trace. The above chromatograms were quenched following 1- and 5-minutes reaction with *Mm* CDO. The peaks associated with ***2ma*** (*retention time*, 11.6 min) and ***2m-bt*** (*retention time*, 16.2 min) were verified by matching retention time with analytical standards, spike assays, and LC-MS/MS.

A fortuitous observation was made in equivalent reactions carried out where methanol was substituted for ethanol. In these reactions, the 16.2 min peak shifted to a lower retention time and the observed molecular ion $[M-H]^+$ decreased to 136 m/z. The -14 amu shift in the molecular ion clearly suggests the absence of a ($-CH_2-$) fragment in methanol reactions as compared to ethanol. Similarly, if benzyl alcohol is substituted for ethanol, a positive molecular ion peak of 212 m/z is observed (+76 amu shift relative to the product formed in methanol). In all cases, the size of the molecular ion $[M-H]^+$ can be calculated by the sum of ***2ma*** (125 amu) and primary alcohol molecular weight (methanol, 32 amu; ethanol, 46 amu; and benzyl alcohol, 108 amu) followed by subtraction of water (18 amu) and 3 hydrogen atoms. This observation indicates that the alcohol utilized in this reaction becomes directly incorporated into the oxidized product.

Based on similar reactivity reported for flavin mimics,[132] cytochrome P450,[133] and mononuclear iron model complexes,[134, 135, 136] we hypothesize that O_2-dependent $\mathbf{2e^-}$ oxidation of the solvent primary alcohol results in formation of aldehydes. Rapid and near quantitative condensation of an aldehyde with the ***2ma*** starting material is anticipated based on the well-established nucleophilic addition of amines. Following this step, it is reasonable to expect formation of a benzothiazole product as illustrated in **Scheme 2**.

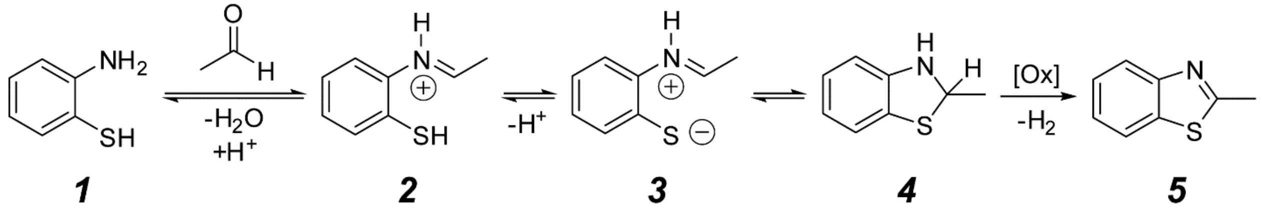

Scheme 4-2: **Proposed mechanism for benzothiazole formation.**

Many synthetic methods describe the oxidative formation of 2-substituted benzothiazoles from 2-aminothiophenol (**Scheme 2**, compound **1**) and aldehydes under various aerobic and dehydrogenative conditions.[132, 137, 138, 139] Generally, this transformation can be envisioned from the initial, reversible condensation of an aldehyde, e.g. acetaldehyde, with the amine to form iminium intermediate **2**. This species undergoes rapid intramolecular cyclization with the nucleophilic thiol. At the working pH and with the electron withdrawing iminium substituent, it is likely that the sulfur nucleophile can form a significant concentration of the thiolate intermediate, **3**, further favoring the cyclization reaction. After cyclization to benzothiazoline, **4**, dehydrogenative formation of the benzothiazole product (similar to NADPH oxidation) is quite facile with a variety of mild oxidants (designated [Ox] in **Scheme 2**).

This mechanistic model correctly predicts the resulting molecular ion size observed in the aforementioned reactions. Further corroboration for the proposed reaction can be taken tandem LC-MS/MS [multiple reaction monitoring (MRM)] results obtained for reaction mixtures. In these experiments, standard solutions (1 μM each) of benzothiazole (***bt***), 2-methylbenzothiazole (***2m-bt***), and 2-phenybenzothiazole (***2p-bt***) were prepared as described in *Materials and Methods* for direct injection. The $[M+H]^+$ molecular ion for each standard (***bt***, 136 m/z; ***2m-bt***, 150 m/z; and

2p-bt, 212 m/z) was selected for secondary fragmentation and MRM optimization was then employed to maximize transition intensity and sensitivity for each fragment allowing for quantitative analysis of product ions. The optimized MRM method was used to compare the product of each enzymatic reaction. For simplicity, all enzymatic reactions were quenched at 5 minutes after injection of enzyme (2 μL).

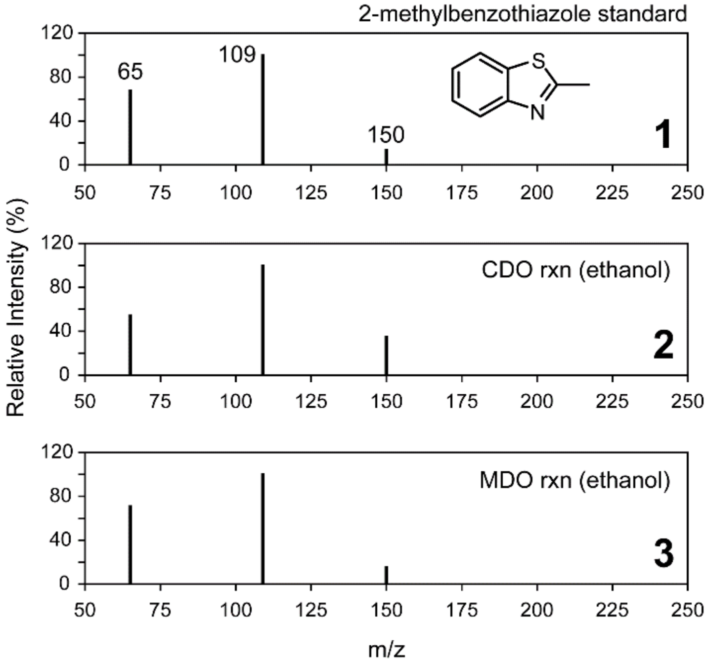

Figure 4-4: MRM spectrum of ***2m-bt*** compared to ***2ma***-reactions in ethanol.

Figure 4 (panel **1**) shows the MRM spectra for a standard solution of ***2m-bt*** in the same assay buffer used for kinetic experiments. In addition to the 150 m/z parent $[M+H]^+$ ion, two additional ions are observed at 65 and 109 m/z. For comparison, the direct injection of the *Mm* CDO catalyzed reaction with ***2ma*** shown in **Fig**. **4** (panel **2**) yields an identical fragmentation pattern. Both the matching fragmentation pattern and relative intensities verify that product generated in

O_2-dependent assays with *Mm* CDO is indeed 2-methylbenzothiazole. Final corroboration was obtained by spiking known quantities of ***2m-bt*** standards into enzymatic assays. As expected, ***2m-bt*** coelutes exactly with the 16.2 min peak observed in HPLC chromatograms. These observations identify ***2m-bt*** as the product of enzymatic reactions with ***2ma*** in the presence of ethanol. For comparison, **Figure 5** illustrates the same analysis used to verify formation of ***bt*** and ***2p-bt*** in reactions utilizing 20% (*v*/*v*) methanol and benzyl alcohol, respectively.

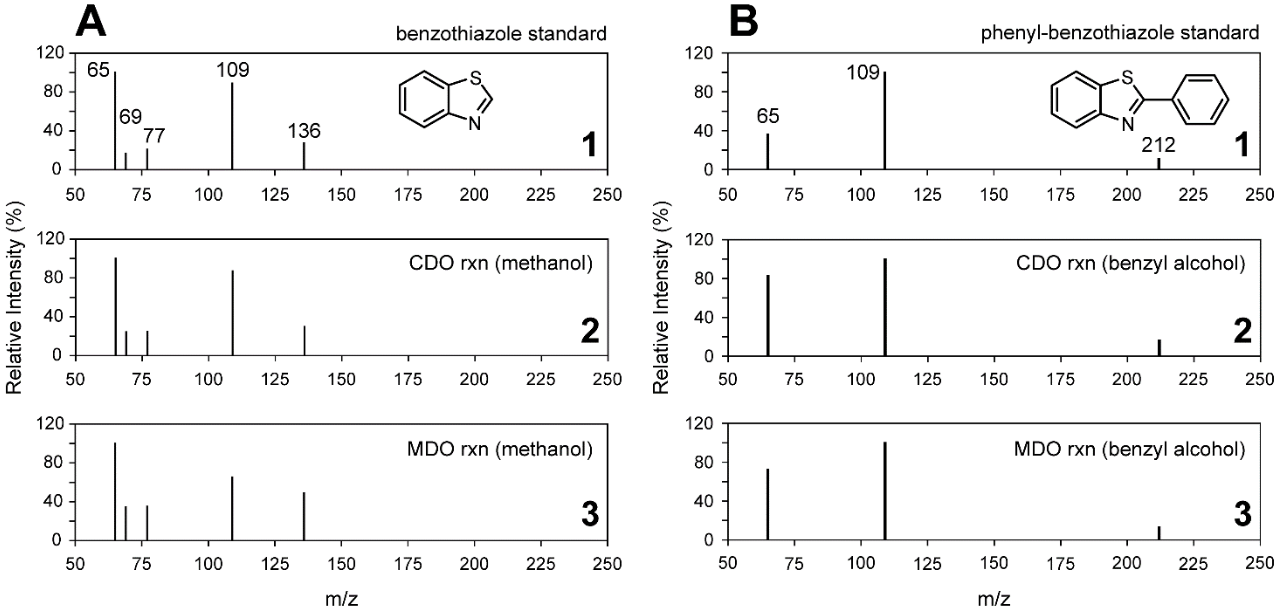

Figure 4-5: LC-MS/MS spectra of MRM $[M-H]^+$ ions observed for the benzothiazole (**A**, Mol. Wt., 135.19 Da) and phenyl-benzothiazole (**B**, Mol. Wt., 211.28 Da) standards are shown in panel **1**. Direct injection of the enzymatic assays carried out with *Mm* CDO in methanol (**A**) and benzyl alcohol (**B**) are shown in panel **2**. Equivalent *Av* MDO reactions are shown in panel **3**.

To this point, the evidence for aldehyde formation by enzymatic oxidation of primary alcohols has been largely inferred based on the products observed. Therefore, GC-MS analysis was performed on extracts of reactions mixtures to directly verify their presence and corroborate the proposed mechanism shown in **Scheme 2**. For this experiment, benzyl alcohol was selected as the co-solvent as its lower volatility (relative to formaldehyde and acetaldehyde) would decrease the possibility for loss during organic extraction. As shown in **Figure 6A** (*trace **1***), beyond the void volume peak at 1.94 min, a single peak is observed at a retention time of 2.94 minutes upon injection of a benzaldehyde standard. Enzymatic assays were performed identically to those described previously for LC-MS experiments. Reactions were initiated by addition of enzyme and allowed to turnover for 20 minutes prior to inactivation by spin-filtration (Corning, Spin-X) and extraction of organic components with dichloromethane. GC-MS chromatograms of reaction extracts exhibit a major peak at 3.33 minutes which corresponds to the benzyl alcohol solvent. While small relative to the benzyl alcohol peak, an additional peak matching the retention time of benzaldehyde (2.94 min) is readily observed in extracts of enzymatic reactions.

Shown in **Figure 6B** is the tandem mass spectrum (MRM) for the standard benzaldehyde peak compared to that observed for enzymatic reaction extracts. The molecular ion for benzaldehyde (106 m/z) was selected for secondary fragmentation and the optimized MRM analysis was run in positive detection mode. As illustrated in **Fig**. **6B** (*trace **1***), beyond the molecular ion, a number of additional fragmentation ions are observed for the benzaldehyde standard[133, 140] 105, 106, and 107 m/z). For comparison, the mass fragmentation and relative intensities of ions observed in reaction extracts (**Fig**. **6B**, *trace **2***) matches that of the benzaldehyde standard confirming the presence of benzaldehyde in reaction mixtures.

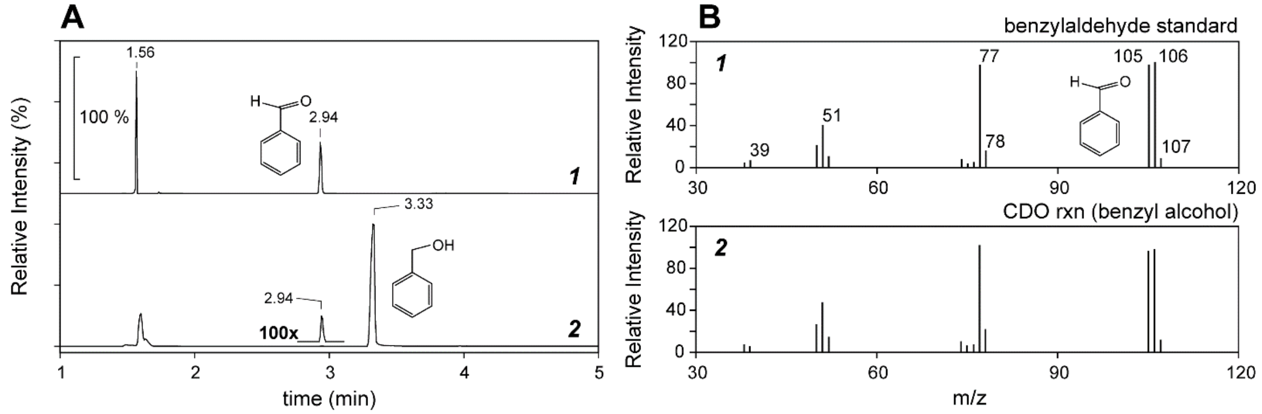

Figure 4-6: GC-MS/MS chromatogram (**A**) and MRM $[M\text{-}H]^+$ spectra (**B**) of enzymatic ***2ma***-reaction extracts. Panel **1** shows the secondary fragmentation pattern of the parent $[M\text{-}H]^+$ benzaldehyde ion (107 m/z) observed in standard reactions (retention time of 2.94 min). Panel **2** shows the comparative MRM spectra for the enzymatic (*Mm* CDO) ***2ma***-reaction dichloromethane extract.

Similarly, MRM spectra obtained by direct injection of reactions carried out in 20% (*v*/*v*) ethanol verify the formation of acetaldehyde in enzymatic ***2ma***-reactions (*Supporting Information*, **Figure S3**). As with reactions performed in benzyl alcohol, the secondary fragmentation pattern of reaction extracts carried out in ethanol match acetaldehyde standards. Most important, control reactions performed in ethanol containing enzyme but lacking the ***2ma*** substrate (**Fig. S3**, *trace 3*) exhibit a markedly different fragmentation pattern as either standards or enzymatic ***2ma***-reactions indicating that acetaldehyde is not present in the starting alcohol solvent and is only produced during enzymatic turnover with ***2ma***.

The scope of this chemistry was further investigated by substituting 20% (*v*/*v*) dimethyl sulfoxide (DMSO) rather than a primary alcohol as this solvent cannot form an aldehyde upon oxidation. As predicted by the proposed mechanism shown in **Scheme 2**, no benzothiazole products are observed in DMSO reactions. Moreover, no evidence for the formation of ***3abs*** [157 Da] was observed by LC-MS either. Similar results were obtained in reactions with dimethylformamide (DMF) as a co-solvent and in reactions lacking any primary alcohol co-solvent. Reactions were performed utilizing the secondary alcohol 2-propanol as well but these failed to produce the expected 2, 2-dimethylbenzothiazoline product. This result of this experiment is discussed in greater detail within the *Supplemental Information,* ***Scheme 1*** *and* ***Fig. S4***. Collectively, these results imply that the formation of benzothiazoles is limited to the use of primary alcohols.

With the identity of reaction products ***bt***, ***2m-bt***, ***2p-bt*** confirmed by overlapping HPLC retention time and LC-MS/MS MRM, analytical determination of product yield was conducted by HPLC by comparison to primary standards. Given the proposed reaction shown in **Scheme 2** it is not surprising that the product yield for these reactions is fairly low. For example, in reactions yielding ***2m-bt***, only 43 ± 8 μM product is observed within the first 5 minutes of the reaction. As enzyme concentration is 2 μM, this suggests ***2m-bt*** is produced over multiple enzymatic turnovers. Beyond 10 minutes, no appreciable increase in ***2m-bt*** concentration is observed. In fact, ***2m-bt*** concentration appears to decrease slightly suggesting either precipitation of the benzothiazole product or further decay. Likely the rapid inactivation of the enzyme can be explained by either the release of ROS or protein denaturation precipitated by the solvent alcohol. Reactions yielding ***bt*** and ***2p-bt*** follow a similar behavior but with attenuated product yields at 5 minutes (28 ± 6 and 3.5 ± 1.2 μM, respectively).

This reaction is first order with respect to oxygen concentration. However, from the perspective of mass balance, the absence of O-atom incorporation into the benzothiazole product (or oxidized 1°-alcohol solvents) indicates that this reaction is completely uncoupled with respect to oxygen;

suggesting that all O_2 consumed over the course of the reaction is released as reactive oxygen species (ROS; H_2O_2, $O_2^{\bullet -}$, $^{\bullet}OH$). Therefore, an obvious question is whether transient Fe-oxo intermediates produced during enzymatic turnover or ROS released by uncoupled catalysis are responsible for direct oxidation of the primary alcohols in solution. However, no decrease in ***2m-bt*** generated, nor its rate of formation was observed in reactions carried out in the presence of catalase, superoxide dismutase, or both (1 mg/mL each); in fact, ***2m-bt*** yields are slightly increased (~20%). This suggests that, if ROS are produced in O_2-dependent ***2ma***-reactions, they do not freely disassociate from the enzymatic active site. It is therefore more likely that a transient Fe-oxo species is responsible for the oxidation of 1°-alcohols. Potentially, ROS generated during the oxidation of the 1°-alcohols could act as an oxidant [Ox] for the dehydrogenation of benzothiazoline (**4**) to form the final benzothiazole product (**5**) shown in **Scheme 2**.

This uncoupled reactivity with oxygen reminiscent to what is observed for *Mm* CDO in reactions utilizing *L*-selenocysteine (***sec***) as a substrate. Despite modest spectroscopic perturbations from the increased polarizability of the Se-atom, both EPR and MCD spectroscopy indicate that the substrate-bound *Mm* CDO complex with ***cys*** and ***sec*** exhibit near equivalent coordination geometry and symmetry around the Fe-site.[54, 115] However, rapid mixing of O_2 with the ***sec***-bound enzyme produces no detectable dioxygenase products. Based on spectroscopically validated computational studies, it was proposed that the subtle electronic differences in the Fe-bound O_2-adduct produced in ***sec***-reactions differ substantially from the native reactions with ***cys*** resulting in an '*off-pathway*' reaction coordinate.[46] The results presented here suggest that the structural constraints and/or differential reactivity of the aromatic ***2ma*** substrate produce a similar effect on CDO and MDO.

The mononuclear non-heme iron site of *Mm* CDO binds substrate bidentate via neutral amine and thiolate coordination. By contrast, it has been demonstrated in both steady-state kinetic and EPR spectroscopic studies that the homologous 3-mercaptopropionic dioxygenase isolated from the soil bacteria *Azotobacter vinelandii* (*Av* MDO) binds substrate via thiolate coordination only.[110, 118] Given the change within the first coordination sphere of the enzyme-substrate complex for both thiol dioxygenase enzymes, it is possible that their reactivity with ***2ma*** could differ. However, as shown in **Fig**. **4** and **Fig**. **5** (panel **3**), identical benzothiazole products are produced in reactions utilizing *Av* MDO. Surprisingly, despite the monodentate substrate-coordination of MDO, no reactivity was observed toward benzenethiol (*Supplemental Information*, **Fig**. **S2**).

Regardless, these experiments clearly demonstrate that ***2ma*** is capable of initiating O_2-consumption for both *Mm* CDO and *Av* MDO. However, rather than the expected sulfinic acid, a benzothiazole product is generated following oxidation of 1°-alcohols in solution. Vastly decreased activities, specificity, and O_2-coupling efficiencies have been reported for CDO and active site variants utilizing non-native substrates.[109] Extensive x-ray crystallographic studies have also been performed highlighting crucial outer Fe-coordination sphere interactions which facilitate efficient catalysis.[141] In some instances, relatively minor or imperceptible structural perturbations within the active site can produce significant shifts in enzymatic activity.[49] While MDO substrate specificity is significantly more relaxed as compared to CDO, both activity and O_2-coupling efficiency are attenuated in reactions with cysteamine (***ca***) and cysteine (***cys***).[110, 142] However, to our knowledge, no crystallographic studies have been reported for the substrate-bound MDO and thus outer Fe-coordination sphere interactions facilitating efficient catalysis are poorly understood.

Although the dioxygenase product (***2abs***) is never observed in ***2ma***-reactions, direct consumption of molecular oxygen is observed with pseudo-first order kinetics dependence on O_2, ***2ma***, and enzyme concentration. It is therefore reasonable that an oxidized iron-oxo species is produced following substrate-gated O_2-activaiton. Based on a similar reports for a variety of model Fe-oxo compounds[134, 135, 136] and Compound I of CytP450,[133] it is reasonable to conclude that the substrate-oxidizing transient intermediate is similarly responsible for the oxidation of the 1°-alcohol in solution in ***2ma***-reactions. Among similar O_2-dependent oxidation of alcohols, H-atom abstraction is typically the rate limiting chemical step. This frequently results in kinetic isotope effects beyond the classical limit ($k_H/k_D \geq 7$).[25, 134, 135, 136, 140] By contrast, in *Mm* CDO O_2-saturated reactions with ***2ma***, a kinetic isotope effect of 1.54 ± 0.13 (n = 3) was observed in equivalent reactions where the 20% (*v*/*v*) ethanol buffer was prepared using 99.5% ethanol-d_6 [Sigma-Aldrich, 186414]. This suggests that H-atom abstraction from the alcohol is not the rate limiting step. However, saturation kinetics for ***2ma*** is not observed due to its limited aqueous solubility and therefore it is likely that non-chemical events such as substrate-binding limit the rate of this reaction. Finally, while the formal oxidation state of the catalytically relevant iron-oxo intermediate [Fe^{III}-superoxo or Fe^{IV}-oxo] remains unclear, it is expected that the structure and/or reactivity of the (**ES**:O_2) ternary complex is different for aromatic versus aliphatic thiols. Therefore, the transient Fe-oxo intermediate responsible for oxidizing 1°-alcohols may not be relevant to native catalysis.

Concluding Remarks

Based on extensive mechanistic, spectroscopic, and crystallographic characterization a general mechanism for catalysis has been developed for non-heme mononuclear iron enzymes.[6, 7, 8] Nearly universally the monoanionic Fe-site contains a 5/6-coordinate ferrous iron with solvent molecules serving as the non-protein ligands. As isolated, the reduced Fe-site is largely unreactive toward molecular oxygen until the substrate and/or cofactor are bound within the active site.[6] The obligate-ordered binding of thiol-substrate to the Fe-site prior to O_2-activation has been reported in previous

Mm CDO and *Av* MDO studies.[76, 110] It has also been noted that both CDO and MDO can catalyze thiol dioxygenase reactions for a number of aliphatic amine/thiol substrates and that optimal activity is observed when these groups are separated by two carbon units.[109] However, the bonds separating the thiol and amine functional groups in the aromatic ***2ma*** substrate are sp^2 hybridized and thus cannot be rotated. Therefore, the ***2ma***-bound Fe-site geometry of *Mm* CDO must be very different as compared to the native substrate **ES**-complex. Presumably, this is also true for *Av* MDO. Despite this obvious distinction, addition of ***2ma*** to CDO and/or MDO triggers the immediate consumption of oxygen (*Supplementary Information*, **Fig**. **S2**). This suggests that the steps leading up to O_2-activation are largely equivalent for reactions utilizing either aliphatic or aromatic thiols. Therefore, this '*off-pathway*' reactivity toward 1°-alcohols may be the result of geometric distortions within the substrate/O_2-bound (**ES**:O_2) ternary complex which prevent thiol-oxidation. Another factor to consider is the differential reactivity of aromatic versus aliphatic thiols. In either case, what can be concluded is that this reactivity is inconsistent with the fixed Fe(II)-oxidation state postulated for '*substrate-activating*' mechanisms. The unusual reactivity described here further illustrates the remarkable versatility in chemical reactivity exhibited by non-heme iron oxygenase/oxidases.

REFERENCES

.

1. Bruijnincx, P. C.; van Koten, G.; Gebbink, R. J. K., Mononuclear non-heme iron enzymes with the 2-His-1-carboxylate facial triad: recent developments in enzymology and modeling studies. *Chemical Society Reviews* **2008,** *37* (12), 2716-2744.

2. Brown, C. D.; Neidig, M. L.; Neibergall, M. B.; Lipscomb, J. D.; Solomon, E. I., VTVH-MCD and DFT Studies of Thiolate Bonding to {FeNO}7/{FeO2}8 Complexes of Isopenicillin N Synthase: Substrate Determination of Oxidase versus Oxygenase Activity in Nonheme Fe Enzymes. *J Am Chem Soc.* **2007,** *129* (23), 7427-7438.

3. Koehntop, K. D.; Emerson, J. P.; Que, L., The 2-His-1-carboxylate facial triad: a versatile platform for dioxygen activation by mononuclear non-heme iron (II) enzymes. *JBIC Journal of Biological Inorganic Chemistry* **2005,** *10* (2), 87-93.

4. Hegg, E. L.; Jr, L. Q., The 2-His-1-carboxylate facial triad—an emerging structural motif in mononuclear non-heme iron (II) enzymes. *European Journal of Biochemistry* **1997,** *250* (3), 625-629.

5. Straganz, G.; Nidetzky, B., Variations of the 2-His-1-carboxylate Theme in Mononuclear Non-Heme FeII Oxygenases. *ChemBioChem* **2006,** *7* (10), 1536-1548.

6. Costas, M.; Mehn, M. P.; Jensen, M. P.; Que, L. J., Diooxygen Activation at Mononuclear Nonheme Iron Active Sites: Enzymes, Models, and Intermediates. *Chem. Rev.* **2004,** *104* (2), 939-986.

7. Solomon, E. I.; Brunold, T. C.; Davis, M. I.; Kemsley, J. N.; Lee, S.-K.; Lehnert, N.; Neese, F.; Skulan, A. J.; Yang, Y.-S.; Zhou, J., Geometric and Electronic Structure/Function Correlations in Non-Heme Iron Enzymes. *Chem. Rev.* **2000,** *100* (1), 235-349.

8. Solomon, E. I.; Decker, A.; Lehnert, N., Non-heme iron enzymes: contrasts to heme catalysis. *Proc Natl Acad Sci USA.* **2003,** *100* (7), 3589-94.

9. Vaillancourt, F. H.; Bolin, J. T.; Eltis, L. D., The ins and outs of ring-cleaving dioxygenases. *Critical Reviews in Biochemistry and Molecular Biology* **2006,** *41* (4), 241-267.

10. Baldwin, J. E.; Bradley, M., Isopenicillin N synthase: mechanistic studies. *Chemical Reviews* **1990,** *90* (7), 1079-1088.

11. Neidig, M. L.; Solomon, E. I., Structure–function correlations in oxygen activating non-heme iron enzymes. *Chemical Communications* **2005,** (47), 5843-5863.

12. Price, J. C.; Barr, E. W.; Hoffart, L. M.; Krebs, C.; Bollinger, J. M., Kinetic dissection of the catalytic mechanism of taurine: α-ketoglutarate dioxygenase (TauD) from Escherichia coli. *Biochemistry* **2005,** *44* (22), 8138-8147.

13. Proshlyakov, D. A.; Henshaw, T. F.; Monterosso, G. R.; Ryle, M. J.; Hausinger, R. P., Direct detection of oxygen intermediates in the non-heme Fe enzyme taurine/α-ketoglutarate dioxygenase. *Journal of the American Chemical Society* **2004,** *126* (4), 1022-1023.

14. Hoffart, L. M.; Barr, E. W.; Guyer, R. B.; Bollinger, J. M.; Krebs, C., Direct spectroscopic detection of a CH-cleaving high-spin Fe (IV) complex in a prolyl-4-hydroxylase. *Proceedings of the National Academy of Sciences* **2006,** *103* (40), 14738-14743.

15. Galonić, D. P.; Barr, E. W.; Walsh, C. T.; Bollinger Jr, J. M.; Krebs, C., Two interconverting Fe (IV) intermediates in aliphatic chlorination by the halogenase CytC3. *Nature chemical biology* **2007,** *3* (2), 113.

16. Mbughuni, M. M.; Chakrabarti, M.; Hayden, J. A.; Bominaar, E. L.; Hendrich, M. P.; Münck, E.; Lipscomb, J. D., Trapping and spectroscopic characterization of an Fe^{III}-superoxo

intermediate from a nonheme mononuclear iron-containing enzyme. *Proc Natl Acad Sci USA.* **2010,** *107* (39), 16788-16793.

17. van der Donk, W. A.; Krebs, C.; Bollinger Jr, J. M., Substrate activation by iron superoxo intermediates. *Current opinion in structural biology* **2010,** *20* (6), 673-683.

18. Bollinger, J. M.; Price, J. C.; Hoffart, L. M.; Barr, E. W.; Krebs, C., Mechanism of Taurine: α-Ketoglutarate Dioxygenase (TauD) from Escherichia coli. *European journal of inorganic chemistry* **2005,** *2005* (21), 4245-4254.

19. Kovaleva, E. G.; Lipscomb, J. D., Crystal Structures of Fe^{2+} Dioxygenase Superoxo, Alkylperoxo, and Bound Product Intermediates. *Science* **2007,** *316* (5823), 453-457.

20. Pinto, A.; Tarasev, M.; Ballou, D. P., Substitutions of the “bridging” aspartate 178 result in profound changes in the reactivity of the Rieske center of phthalate dioxygenase. *Biochemistry* **2006,** *45* (30), 9032-9041.

21. Gibson, D.; Resnick, S.; Lee, K.; Brand, J.; Torok, D.; Wackett, L.; Schocken, M.; Haigler, B., Desaturation, dioxygenation, and monooxygenation reactions catalyzed by naphthalene dioxygenase from Pseudomonas sp. strain 9816-4. *Journal of bacteriology* **1995,** *177* (10), 2615-2621.

22. Lee, J.; Zhao, H., Mechanistic studies on the conversion of arylamines into arylnitro compounds by aminopyrrolnitrin oxygenase: Identification of intermediates and kinetic studies. *Angewandte Chemie International Edition* **2006,** *45* (4), 622-625.

23. Herman, P. L.; Behrens, M.; Chakraborty, S.; Chrastil, B. M.; Barycki, J.; Weeks, D. P., A three-component dicamba O-demethylase from Pseudomonas maltophilia, strain DI-6 gene isolation, characterization, and heterologous expression. *Journal of Biological Chemistry* **2005,** *280* (26), 24759-24767.

24. Ferraro, D. J.; Gakhar, L.; Ramaswamy, S., Rieske business: structure–function of Rieske non-heme oxygenases. *Biochemical and biophysical research communications* **2005,** *338* (1), 175-190.

25. Chen, K.; Que, L., Stereospecific Alkane Hydroxylation by Non-Heme Iron Catalysts: Mechanistic Evidence for an FeVO Active Species. *J Am Chem Soc.* **2001,** *123* (26), 6327-6337.

26. Boyd, D. R.; Bugg, T. D., Arene cis-dihydrodiol formation: from biology to application. *Organic & biomolecular chemistry* **2006,** *4* (2), 181-192.

27. Abu-Omar, M. M.; Loaiza, A.; Hontzeas, N., Reaction mechanisms of mononuclear non-heme iron oxygenases. *Chemical reviews* **2005,** *105* (6), 2227-2252.

28. Clifton, I. J.; McDonough, M. A.; Ehrismann, D.; Kershaw, N. J.; Granatino, N.; Schofield, C. J., Structural studies on 2-oxoglutarate oxygenases and related double-stranded β-helix fold proteins. *Journal of inorganic biochemistry* **2006,** *100* (4), 644-669.

29. Pavel, E. G.; Zhou, J.; Busby, R. W.; Gunsior, M.; Townsend, C. A.; Solomon, E. I., Circular dichroism and magnetic circular dichroism spectroscopic studies of the non-heme ferrous active site in clavaminate synthase and its interaction with α-ketoglutarate cosubstrate. *Journal of the American Chemical Society* **1998,** *120* (4), 743-753.

30. Elkins, J. M.; Ryle, M. J.; Clifton, I. J.; Dunning Hotopp, J. C.; Lloyd, J. S.; Burzlaff, N. I.; Baldwin, J. E.; Hausinger, R. P.; Roach, P. L., X-ray crystal structure of Escherichia coli taurine/α-ketoglutarate dioxygenase complexed to ferrous iron and substrates. *Biochemistry* **2002,** *41* (16), 5185-5192.

31. Riggs-Gelasco, P. J.; Price, J. C.; Guyer, R. B.; Brehm, J. H.; Barr, E. W.; Bollinger, J. M.; Krebs, C., EXAFS spectroscopic evidence for an Fe O unit in the Fe (IV) intermediate observed

during oxygen activation by taurine: α-ketoglutarate dioxygenase. *Journal of the American Chemical Society* **2004,** *126* (26), 8108-8109.

32. Price, J. C.; Barr, E. W.; Glass, T. E.; Krebs, C.; Bollinger, J. M., Evidence for hydrogen abstraction from C1 of taurine by the high-spin Fe (IV) intermediate detected during oxygen activation by taurine: α-ketoglutarate dioxygenase (TauD). *Journal of the American Chemical Society* **2003,** *125* (43), 13008-13009.

33. Andersen, O. A.; Flatmark, T.; Hough, E., High resolution crystal structures of the catalytic domain of human phenylalanine hydroxylase in its catalytically active Fe (II) form and binary complex with tetrahydrobiopterin1. *Journal of molecular biology* **2001,** *314* (2), 279-291.

34. Erlandsen, H.; Kim, J. Y.; Patch, M. G.; Han, A.; Volner, A.; Abu-Omar, M. M.; Stevens, R. C., Structural comparison of bacterial and human iron-dependent phenylalanine hydroxylases: similar fold, different stability and reaction rates. *Journal of molecular biology* **2002,** *320* (3), 645-661.

35. Pavon, J. A.; Fitzpatrick, P. F., Insights into the catalytic mechanisms of phenylalanine and tryptophan hydroxylase from kinetic isotope effects on aromatic hydroxylation. *Biochemistry* **2006,** *45* (36), 11030-11037.

36. Pavon, J. A.; Fitzpatrick, P. F., Intrinsic isotope effects on benzylic hydroxylation by the aromatic amino acid hydroxylases: evidence for hydrogen tunneling, coupled motion, and similar reactivities. *Journal of the American Chemical Society* **2005,** *127* (47), 16414-16415.

37. Moran, G. R.; Derecskei-Kovacs, A.; Hillas, P. J.; Fitzpatrick, P. F., On the catalytic mechanism of tryptophan hydroxylase. *Journal of the American Chemical Society* **2000,** *122* (19), 4535-4541.

38. Hillas, P. J.; Fitzpatrick, P. F., A mechanism for hydroxylation by tyrosine hydroxylase based on partitioning of substituted phenylalanines. *Biochemistry* **1996,** *35* (22), 6969-6975.

39. Roach, P. L.; Clifton, I. J.; Hensgens, C. M.; Shibata, N.; Schofield, C. J.; Hajdu, J.; Baldwin, J. E., Structure of isopenicillinN synthase complexed with substrate and the mechanism ofpenicillin formation. *Nature* **1997,** *387* (6635), 827.

40. Roach, P. L.; Clifton, I. J.; Fülöp, V.; Harlos, K.; Barton, G. J.; Hajdu, J.; Andersson, I.; Schofield, C. J.; Baldwin, J. E., Crystal structure of isopenicillin N synthase is the first from a new structural family of enzymes. *Nature* **1995,** *375* (6533), 700.

41. Burzlaff, N. I.; Rutledge, P. J.; Clifton, I. J.; Hensgens, C. M.; Pickford, M.; Adlington, R. M.; Roach, P. L.; Baldwin, J. E., The reaction cycle of isopenicillin N synthase observed by X-ray diffraction. *Nature* **1999,** *401* (6754), 721.

42. Rocklin, A. M.; Kato, K.; Liu, H.-w.; Que, L.; Lipscomb, J. D., Mechanistic studies of 1-aminocyclopropane-1-carboxylic acid oxidase: single turnover reaction. *JBIC Journal of Biological Inorganic Chemistry* **2004,** *9* (2), 171-182.

43. Zhou, J.; Rocklin, A. M.; Lipscomb, J. D.; Que, L.; Solomon, E. I., Spectroscopic studies of 1-aminocyclopropane-1-carboxylic acid oxidase: molecular mechanism and CO2 activation in the biosynthesis of ethylene. *Journal of the American Chemical Society* **2002,** *124* (17), 4602-4609.

44. Tierney, D. L.; Rocklin, A. M.; Lipscomb, J. D.; Que, L.; Hoffman, B. M., ENDOR studies of the ligation and structure of the non-heme iron site in ACC oxidase. *Journal of the American Chemical Society* **2005,** *127* (19), 7005-7013.

45. Lindskog, S., Structure and mechanism of carbonic anhydrase. *Pharmacology & therapeutics* **1997,** *74* (1), 1-20.

46. Blaesi, E. J.; Gardner, J. D.; Fox, B. G.; Brunold, T. C., Spectroscopic and Computational Characterization of the NO Adduct of Substrate-Bound Fe(II) Cysteine Dioxygenase: Insights into the Mechanism of O2 Activation. *Biochemistry* **2013,** *52* (35), 6040-6051.

47. Diebold, A. R.; Neidig, M. L.; Moran, G. R.; Straganz, G. D.; Solomon, E. I., The three-his triad in Dke1: comparisons to the classical facial triad. *Biochemistry* **2010,** *49* (32), 6945-6952.

48. Adams, M. A.; Singh, V. K.; Keller, B. O.; Jia, Z., Structural and biochemical characterization of gentisate 1, 2-dioxygenase from Escherichia coli O157: H7. *Molecular microbiology* **2006,** *61* (6), 1469-1484.

49. Davies, C. G.; Fellner, M.; Tchesnokov, E. P.; Wilbanks, S. M.; Jameson, G. N. L., The Cys-Tyr Cross-Link of Cysteine Dioxygenase Changes the Optimal pH of the Reaction without a Structural Change. *Biochemistry* **2014,** *53* (50), 7961-7968.

50. Simmons, C. R.; Krishnamoorthy, K.; Granett, S. L.; Schuller, D. J.; Dominy, J. E.; Begley, T. P.; Stipanuk, M. H.; Karplus, P. A., A Putative Fe^{2+}-Bound Persulfenate Intermediate in Cysteine Dioxygenase. *Biochemistry* **2008,** *47* (44), 11390-11392.

51. Stipanuk, M. H., Sulfur Amino Acid Metabolism: Pathways for Production and Removal of Homocysteine and Cysteine. *Annu Rev Nutr.* **2004,** *24*, 539-77.

52. Parsons, R.; Waring, R.; Ramsden, D.; Williams, A., In vitro effect of the cysteine metabolites homocysteic acid, homocysteine and cysteic acid upon human neuronal cell lines. *Neurotoxicology* **1998,** *19* (4-5), 599-603.

53. McCoy, J. G.; Bailey, L. J.; Bitto, E.; Bingman, C. A.; Aceti, D. J.; Fox, B. G.; Phillips, G. N., Jr., Structure and mechanism of mouse cysteine dioxygenase. *Proc Natl Acad Sci USA.* **2006,** *103* (9), 3084-3089.

54. Crawford, J. A.; Li, W.; Pierce, B. S., Single turnover of substrate-bound ferric cysteine dioxygenase (CDO) with superoxide anion: enzymatic reactivation, product formation, and a transient intermediate. *Biochemistry* **2011,** *50* (47), 10241-10253.

55. Pierce, B. S.; Gardner, J. D.; Bailey, L. J.; Brunold, T. C.; Fox, B. G., Characterization of the nitrosyl adduct of substrate-bound mouse cysteine dioxygenase by electron paramagnetic resonance: electronic structure of the active site and mechanistic implications. *Biochemistry* **2007,** *46* (29), 8569-8578.

56. Dominy, J. E., Jr.; Simmons, C. R.; Karplus, P. A.; Gehring, A. M.; Stipanuk, M. H., Identification and Characterization of Bacterial Cysteine Dioxygenases: a New Route of Cysteine Degradation for Eubacteria. *J Bacteriol.* **2006,** *188* (15), 5561-5569.

57. Driggers, C. M.; Hartman, S. J.; Karplus, P. A., Structures of Arg- and Gln-type bacterial cysteine dioxygenase homologs. *Protein Science* **2015,** *24* (1), 154-161.

58. Bruland, N.; Wübbeler, J. H.; Steinbüchel, A., 3-Mercaptopropionate dioxygenase, a cysteine dioxygenase homologue, catalyzes the initial step of 3-mercaptopropionate catabolism in the 3, 3-thiodipropionic acid-degrading bacterium Variovorax paradoxus. *Journal of Biological Chemistry* **2009,** *284* (1), 660-672.

59. Simmons, C. R.; Liu, Q.; Huang, Q.; Hao, Q.; Begley, T. P.; Karplus, P. A.; Stipanuk, M. H., Crystal Structure of Mammalian Cysteine Dioxygenase. *J Biol Chem.* **2006,** *281* (27), 18723-18733.

60. Ye, S.; Wu, X. a.; Wei, L.; Tang, D.; Sun, P.; Bartlam, M.; Rao, Z., An Insight into the Mechanism of Human Cysteine Dioxygenase: Key Roles of the Thioether-Bonded Tyrosine-Cysteine Cofactor. *J Biol Chem.* **2007,** *282* (5), 3391-3402.

61. Lombardini, J. B.; Singer, T. P.; Boyer, P. D., Cysteine Oxygenase. *J Biol Chem.* **1969,** *244* (5), 1172-1175.

62. Bruland, N.; Wubbeler, J. H.; Steinbuchel, A., 3-mercaptopropionate dioxygenase, a cysteine dioxygenase homologue, catalyzes the initial step of 3-mercaptopropionate catabolism in the 3,3-thiodipropionic acid-degrading bacterium variovorax paradoxus. *The Journal of biological chemistry* **2009,** *284* (1), 660-72.

63. Winyard, P. G.; Moody, C. J.; Jacob, C., Oxidative activation of antioxidant defence. *Trends Biochem Sci.* **2005,** *30* (8), 453-461.

64. Reddie, K. G.; Carroll, K. S., Expanding the functional diversity of proteins through cysteine oxidation. *Curr Opin Chem Biol.* **2008,** *12* (6), 746-754.

65. Trachootham, D.; Alexandre, J.; Huang, P., Targeting cancer cells by ROS-mediated mechanisms: a radical therapeutic approach? *Nat Rev Drug Discov* **2009,** *8* (7), 579-591.

66. Behave, D. P.; Muse, W. B.; Carroll, K. S., Drug Targets in Mycobacterial Sulfur Metabolism. *Infect Disord Drug Targets.* **2007,** *7*, 140-158.

67. Gordon, C.; Emery, P.; Bradley, H.; Waring, H., Abnormal sulfur oxidation in systemic lupus erythematosus. *Lancett* **1992,** *229* (8784), 25-6.

68. Heafield, M. T.; Fearn, S.; Steventon, G. B.; Waring, R. H.; Williams, A. C.; Sturman, S. G., Plasma cysteine and sulfate levels in patients with motor neurone, Parkinson's and Alzheimer's disease. *Neurosci Lett.* **1990,** *110* (1-2), 216-220.

69. James, S. J.; Cutler, P.; Melnyk, S.; Jernigan, S.; Janak, L.; Gaylor, D. W.; Neubrander, J. A., Metabolic biomarkers of increased oxidative stress and impaired methylation capacity in children with autism. *Am J Clin Nutr.* **2004,** *80* (6), 1611-1617.

70. Deth, R.; Muratore, C.; Benzecry, J.; Power-Charnitsky, V.-A.; Waly, M., How environmental and genetic factors combine to cause autism: A redox/methylation hypothesis. *NeuroToxicology* **2008,** *29* (1), 190-201.

71. Driggers, C. M.; Cooley, R. B.; Sankaran, B.; Hirschberger, L. L.; Stipanuk, M. H.; Karplus, P. A., Cysteine Dioxygenase Structures from pH 4 to 9: Consistent Cys-Persulfenate Formation at Intermediate pH and a Cys-Bound Enzyme at Higher pH. *Mol Microbiol.* **2013,** *425* (17), 3121-3136.

72. Simmons, C. R.; Liu, Q.; Huang, Q.; Hao, Q.; Begley, T. P.; Karplus, P. A.; Stipanuk, M. H., Crystal Structure of Mammalian Cysteine Dioxygenase A NOVEL MONONUCLEAR IRON CENTER FOR CYSTEINE THIOL OXIDATION. *Journal of Biological Chemistry* **2006,** *281* (27), 18723-18733.

73. Li, W.; Pierce, B. S., Steady-state substrate specificity and O_2-coupling efficiency of mouse cysteine dioxygenase. *Arch Biochem Biophys.* **2015,** *565*, 49-56.

74. Easson, L. H.; Stedman, E., Studies on the relationship between chemical constitution and physiological action: Molecular dissymmetry and physiological activity. *The Biochemical journal* **1933,** *27* (4), 1257-66.

75. Kiene, R. P.; Taylor, B. F., Biotransformations of organosulphur compounds in sediments via 3-mercaptopropionate. *Nature* **1988,** *332* (6160), 148.

76. Pierce, B. S.; Gardner, J. D.; Bailey, L. J.; Brunold, T. C.; Fox, B. G., Characterization of the nitrosyl adduct of substrate-bound mouse cysteine dioxygenase by electron paramagnetic resonance: electronic structure of the active site and mechanistic implications. *Biochemistry* **2007,** *46* (29), 8569-78.

77. Collins, P. F.; Diehl, H.; Smith, G. F., 2, 4, 6-Tripyridyl-s-triazine as reagent for iron. Determination of iron in limestone, silicates, and refractories. *Analytical Chemistry* **1959,** *31* (11), 1862-1867.

78. Li, W.; Blaesi, E. J.; Pecore, M. D.; Crowell, J. K.; Pierce, B. S., Second-sphere interactions between the C93-Y157 cross-link and the substrate-bound Fe site influence the O(2) coupling efficiency in mouse cysteine dioxygenase. *Biochemistry* **2013,** *52* (51), 9104-19.

79. Crowell, J. K.; Li, W.; Pierce, B. S., Oxidative uncoupling in cysteine dioxygenase is gated by a proton-sensitive intermediate. *Biochemistry* **2014,** *53* (48), 7541-8.

80. Denu, J. M.; Fitzpatrick, P. F., pH and kinetic isotope effects on the oxidative half-reaction of D-amino-acid oxidase. *J Biol Chem.* **1994,** *269* (21), 15054-15059.

81. Cleland, W. W., [22] The use of pH studies to determine chemical mechanisms of enzyme-catalyzed reactions. In *Methods in enzymology*, Elsevier: 1982; Vol. 87, pp 390-405.

82. Li, W.; Blaesi, E. J.; Pecore, M. D.; Crowell, J. K.; Pierce, B. S., Second-Sphere Interactions between the C93–Y157 Cross-Link and the Substrate-Bound Fe Site Influence the O_2 Coupling Efficiency in Mouse Cysteine Dioxygenase. *Biochemistry* **2013,** *52* (51), 9104-9119.

83. Cook, P.; Cleland, W. W., *Enzyme kinetics and mechanism*. Garland Science: 2007.

84. Abragam, A.; Bleaney, B., EPR of transition ions. Clarendon Press, Oxford: 1970.

85. Crawford, J. A.; Li, W.; Pierce, B. S., Single turnover of substrate-bound ferric cysteine dioxygenase (CDO) with superoxide anion: enzymatic reactivation, product formation, and a transient intermediate. *Biochemistry* **2011,** *50* (47), 10241–10253.

86. Smitherman, C.; Gadda, G., Evidence for a Transient Peroxynitro Acid in the Reaction Catalyzed by Nitronate Monooxygenase with Propionate 3-Nitronate. *Biochemistry* **2013,** *52* (15), 2694-2704.

87. Wanat, A.; Schneppensieper, T.; Stochel, G.; van Eldik, R.; Bill, E.; Wieghardt, K., Kinetics, mechanism, and spectroscopy of the reversible binding of nitric oxide to aquated iron (II). An undergraduate text book reaction revisited. *Inorganic chemistry* **2002,** *41* (1), 4-10.

88. Li, M.; Bonnet, D.; Bill, E.; Neese, F.; Weyhermüller, T.; Blum, N.; Sellmann, D.; Wieghardt, K., Tuning the Electronic Structure of Octahedral Iron Complexes [FeL (X)](L= 1-Alkyl-4, 7-bis (4-tert-butyl-2-mercaptobenzyl)-1, 4, 7-triazacyclononane, X= Cl, CH3O, CN, NO). The S= 1/2⇌ S= 3/2 Spin Equilibrium of [FeLPr (NO)]. *Inorganic chemistry* **2002,** *41* (13), 3444-3456.

89. Sellmann, D.; Blum, N.; Heinemann, F. W.; Hess, B. A., Synthesis, reactivity, and structure of strictly homologous 18 and 19 valence electron iron nitrosyl complexes. *Chemistry–A European Journal* **2001,** *7* (9), 1874-1880.

90. Brown, C. D.; Neidig, M. L.; Neibergall, M. B.; Lipscomb, J. D.; Solomon, E. I., VTVH-MCD and DFT studies of thiolate bonding to {FeNO} 7/{FeO2} 8 complexes of isopenicillin N synthase: substrate determination of oxidase versus oxygenase activity in nonheme Fe enzymes. *Journal of the American Chemical Society* **2007,** *129* (23), 7427-7438.

91. Clay, M. D.; Cosper, C. A.; Jenney, F. E.; Adams, M. W.; Johnson, M. K., Nitric oxide binding at the mononuclear active site of reduced Pyrococcus furiosus superoxide reductase. *Proceedings of the National Academy of Sciences* **2003,** *100* (7), 3796-3801.

92. Cleland, W. W., [22] The use of pH studies to determine chemical mechanisms of enzyme-catalyzed reactions. In *Methods Enzymol.* , Daniel, L. P., Ed. Academic Press: 1982; Vol. Volume 87, pp 390-405.

93. Dominy, J. E.; Hwang, J.; Guo, S.; Hirschberger, L. L.; Zhang, S.; Stipanuk, M. H., Synthesis of amino acid cofactor in cysteine dioxygenase is regulated by substrate and represents

a novel post-translational regulation of activity. *Journal of Biological Chemistry* **2008,** *283* (18), 12188-12201.

94. Siakkou, E.; Rutledge, M. T.; Wilbanks, S. M.; Jameson, G. N., Correlating crosslink formation with enzymatic activity in cysteine dioxygenase. *Biochimica et Biophysica Acta (BBA)-Proteins and Proteomics* **2011,** *1814* (12), 2003-2009.

95. Farquhar, E. R.; Koehntop, K. D.; Emerson, J. P.; Que Jr, L., Post-translational self-hydroxylation: A probe for oxygen activation mechanisms in non-heme iron enzymes. *Biochemical and biophysical research communications* **2005,** *338* (1), 230-239.

96. Ryle, M. J.; Koehntop, K. D.; Liu, A.; Que, L.; Hausinger, R. P., Interconversion of two oxidized forms of taurine/α-ketoglutarate dioxygenase, a non-heme iron hydroxylase: Evidence for bicarbonate binding. *Proceedings of the National Academy of Sciences* **2003,** *100* (7), 3790-3795.

97. Quinn, D. M.; Sutton, L. D., Theoretical basis and mechanistic utility of solvent isotope effects. In *Enzyme Mechanism from Isotope Effects*, Cook, P. F., Ed. CRC Press: 1991; pp 73-126.

98. Venkatasubban, K. S.; Schowen, R. L., The Proton Inventory Technique. *Critical Reviews in Biochemistry and Molecular Biology* **1984,** *17* (1), 1-44.

99. Schowen, K. B.; Schowen, R. L., [29] Solvent isotope effects on enzyme systems. In *Methods in enzymology*, Elsevier: 1982; Vol. 87, pp 551-606.

100. McQuilken, A. C.; Ha, Y.; Sutherlin, K. D.; Siegler, M. A.; Hodgson, K. O.; Hedman, B.; Solomon, E. I.; Jameson, G. N.; Goldberg, D. P., Preparation of Non-heme {FeNO} 7 Models of Cysteine Dioxygenase: Sulfur versus Nitrogen Ligation and Photorelease of Nitric Oxide. *Journal of the American Chemical Society* **2013,** *135* (38), 14024-14027.

101. Berto, T. C.; Speelman, A. L.; Zheng, S.; Lehnert, N., Mono-and dinuclear non-heme iron–nitrosyl complexes: Models for key intermediates in bacterial nitric oxide reductases. *Coordination Chemistry Reviews* **2013,** *257* (1), 244-259.

102. Reginato, N.; McCrory, C. T.; Pervitsky, D.; Li, L., Synthesis, X-ray crystal structure, and solution behavior of Fe (NO) 2 (1-MeIm) 2: implications for nitrosyl non-heme-iron complexes with g= 2.03. *Journal of the American Chemical Society* **1999,** *121* (43), 10217-10218.

103. Lu, S.; Libby, E.; Saleh, L.; Xing, G.; Bollinger, J. M.; Moënne-Loccoz, P., Characterization of NO adducts of the diiron center in protein R2 of Escherichia coli ribonucleotide reductase and site-directed variants; implications for the O 2 activation mechanism. *JBIC Journal of Biological Inorganic Chemistry* **2004,** *9* (7), 818-827.

104. Butler, A. R.; Megson, I. L., Non-heme iron nitrosyls in biology. *Chemical reviews* **2002,** *102* (4), 1155-1166.

105. Bryar, T. R.; Eaton, D. R., Electronic configuration and structure of paramagnetic iron dinitrosyl complexes. *Canadian Journal of Chemistry* **1992,** *70* (7), 1917-1926.

106. Ewetz, L.; Sorbo, B., Characteristics of the Cysteinesulfinate-Forming Enzyme System in Rat Liver. *Biochim Biophys Acta.* **1966,** *128*, 296-305.

107. Sorbo, B.; Ewetz, L., The Enzymatic Oxidation of Cysteine to Cysteinesulfinate in Rat Liver. *Biochem Biophys Res Commun.* **1965,** *18* (3), 359-363.

108. Tchesnokov, E. P.; Fellner, M.; Siakkou, E.; Kleffmann, T.; Martin, L. W.; Aloi, S.; Lamont, I. L.; Wilbanks, S. M.; Jameson, G. N. L., The Cysteine Dioxygenase Homologue from Pseudomonas aeruginosa is a 3-Mercaptopropionate Dioxygenase. *J Biol Chem.* **2015**.

109. Li, W.; Pierce, B. S., Steady-state substrate specificity and O_2-coupling efficiency of mouse cysteine dioxygenase. *Arch Biochem Biophys.* **2015,** *565*, 49-56.

110. Pierce, B. S.; Subedi, B. P.; Sardar, S.; Crowell, J. K., The "Gln-Type" Thiol Dioxygenase from Azotobacter vinelandii Is a 3-Mercaptopropionic Acid Dioxygenase. *Biochemistry* **2015,** *54* (51), 7477-7490.

111. Notomista, E.; Lahm, A.; Di Donato, A.; Tramontano, A., Evolution of Bacterial and Archaeal Multicomponent Monooxygenases. *J Mol Evol.* **2003,** *56* (4), 435-445.

112. Crawford, J. A.; Li, W.; Pierce, B. S., Single Turnover of Substrate-Bound Ferric Cysteine Dioxygenase with Superoxide Anion: Enzymatic Reactivation, Product Formation, and a Transient Intermediate. *Biochemistry* **2011,** *50* (47), 10241-10253.

113. Cook, P. F.; Cleland, W. W., *Enzyme Kinetics and Mechanisms*. Garland Science: New York, 2007.

114. Blaesi, E. J.; Fox, B. G.; Brunold, T. C., Spectroscopic and computational investigation of iron (III) cysteine dioxygenase: implications for the nature of the putative superoxo-Fe (III) intermediate. *Biochemistry* **2014,** *53* (36), 5759-5770.

115. Gardner, J. D.; Pierce, B. S.; Fox, B. G.; Brunold, T. C., Spectroscopic and Computational Characterization of Substrate-Bound Mouse Cysteine Dioxygenase: Nature of the Ferrous and Ferric Cysteine Adducts and Mechanistic Implications. *Biochemistry* **2010,** *49* (29), 6033-6041.

116. Cleland, W. W., The use of isotope effects to determine enzyme mechanisms. *Journal of Biological Chemistry* **2003,** *278* (52), 51975-51984.

117. Blaesi, E. J.; Fox, B. G.; Brunold, T. C., Spectroscopic and computational Investigation of the H155A variant of cysteine dioxygenase: Geometric and electronic consequences of a third-sphere amino acid substitution. *Biochemistry* **2015,** *54* (18), 2874-2884.

118. Crowell, J. K.; Sardar, S.; Hossain, M. S.; Foss Jr, F. W.; Pierce, B. S., Non-chemical proton-dependent steps prior to O_2-activation limit Azotobacter vinelandii 3-mercaptopropionic acid dioxygenase (MDO) catalysis. *Arch Biochem Biophys.* **2016,** *604*, 86-94.

119. Kabil, O.; Banerjee, R., Redox Biochemistry of Hydrogen Sulfide. *J Biol Chem.* **2010,** *285* (29), 21903-21907.

120. Driggers, C. M.; Cooley, R. B.; Sankaran, B.; Hirschberger, L. L.; Stipanuk, M. H.; Karplus, P. A., Cysteine Dioxygenase Structures from pH 4 to 9: Consistent Cys-Persulfenate Formation at Intermediate pH and a Cys-Bound Enzyme at Higher pH. *Mol Microbiol.* **2013,** *425* (17), 3121-3136.

121. Tchesnokov, E. P.; Faponle, A. S.; Davies, C. G.; Quesne, M. G.; Turner, R.; Fellner, M.; Souness, R. J.; Wilbanks, S. M.; de Visser, S. P.; Jameson, G. N. L., An iron-oxygen intermediate formed during the catalytic cycle of cysteine dioxygenase. *Chem Commun (Camb).* **2016,** *52* (57), 8814-8817.

122. Lipscomb, J. D., Mechanism of extradiol aromatic ring-cleaving dioxygenases. *Curr Opin Struct Biol.* **2008,** *18* (6), 644-649.

123. Broderick, J. B., Catechol dioxygenases. *Essays Biochem.* **1999,** *34*, 173-189.

124. Gunderson, W. A.; Zatsman, A. I.; Emerson, J. P.; Farquhar, E. R.; Que, L.; Lipscomb, J. D.; Hendrich, M. P., Electron Paramagnetic Resonance Detection of Intermediates in the Enzymatic Cycle of an Extradiol Dioxygenase. *J Am Chem Soc.* **2008,** *130* (44), 14465-14467.

125. Mbughuni, M. M.; Chakrabarti, M.; Hayden, J. A.; Bominaar, E. L.; Hendrich, M. P.; Münck, E.; Lipscomb, J. D., Trapping and spectroscopic characterization of an FeIII-superoxo intermediate from a nonheme mononuclear iron-containing enzyme. *Proc Natl Acad Sci U S A.* **2010,** *107* (39), 16788-16793.

126. Kenny, R. S.; Mashelkar, U. C., Synthesis of 2-aryl and coumarin substituted benzothiazole derivatives. *J Heterocycl Chem.* **2006,** *43* (5), 1367-1369.

127. Guntreddi, T.; Vanjari, R.; Singh, K. N., Elemental Sulfur Mediated Decarboxylative Redox Cyclization Reaction of o-Chloronitroarenes and Arylacetic Acids. *Organic Letters* **2015,** *17* (4), 976-978.

128. Corder, A. L.; Subedi, B. P.; Zhang, S.; Dark, A. M.; Foss, F. W.; Pierce, B. S., Peroxide-Shunt Substrate-Specificity for the *Salmonella typhimurium* O_2-Dependent tRNA Modifying Monooxygenase (MiaE). *Biochemistry* **2013,** *52* (36), 6182-6196.

129. Subedi, B. P.; Corder, A. L.; Zhang, S.; Foss, F. W. J.; Pierce, B. S., Steady-state kinetics and spectroscopic characterization of enzyme-tRNA interactions for the non-heme diiron tRNA-monooxygenase, MiaE. *Biochemistry* **2014,** *54* (2), 363-76.

130. Yost, R. A.; Fetterolf, D. D., Tandem mass spectrometry (MS/MS) instrumentation. *Mass Spectrom Rev.* **1983,** *2* (1), 1-45.

131. Kloepfer, A.; Jekel, M.; Reemtsma, T., Determination of benzothiazoles from complex aqueous samples by liquid chromatography–mass spectrometry following solid-phase extraction. *J Chromatogr A.* **2004,** *1058* (1–2), 81-88.

132. Chen, S.; Hossain, M. S.; Foss, F. W., Bioinspired Oxidative Aromatizations: One-Pot Syntheses of 2-Substituted Benzothiazoles and Pyridines by Aerobic Organocatalysis. *ACS Sustain Chem Eng* **2013,** *1* (8), 1045-1051.

133. Wang, Q.; Sheng, X.; Horner, J. H.; Newcomb, M., Quantitative Production of Compound I from a Cytochrome P450 Enzyme at Low Temperatures. Kinetics, Activation Parameters, and Kinetic Isotope Effects for Oxidation of Benzyl Alcohol. *J Am Chem Soc.* **2009,** *131* (30), 10629-10636.

134. Oh, N. Y.; Suh, Y.; Park, M. J.; Seo, M. S.; Kim, J.; Nam, W., Mechanistic Insight into Alcohol Oxidation by High-Valent Iron–Oxo Complexes of Heme and Nonheme Ligands. *Angew Chem Int Ed Engl.* **2005,** *44* (27), 4235-4239.

135. Nam, W.; Lee, Y.-M.; Fukuzumi, S., Tuning Reactivity and Mechanism in Oxidation Reactions by Mononuclear Nonheme Iron(IV)-Oxo Complexes. *Acc Chem Res.* **2014,** *47* (4), 1146-1154.

136. Ghosh, M.; Nikhil, Y. L. K.; Dhar, B. B.; Sen Gupta, S., Mechanism of Alcohol Oxidation by FeV(O) at Room Temperature. *Inorganic Chemistry* **2015,** *54* (24), 11792-11798.

137. Yu, J.; Xia, Y.; Lu, M., Iron-Catalyzed Highly Efficient Aerobic Oxidative Synthesis of Benzimidazoles, Benzoxazoles, and Benzothiazoles Directly from Aromatic Primary Amines Under Solvent-Free Conditions in the Open Air. *Synth. Commun.* **2014,** *44* (20), 3019-3026.

138. Bahrami, K.; Khodaei, M. M.; Naali, F., Mild and Highly Efficient Method for the Synthesis of 2-Arylbenzimidazoles and 2-Arylbenzothiazoles. *J Org Chem.* **2008,** *73* (17), 6835-6837.

139. Gopalaiah, K.; Chandrudu, S. N., Iron(ii) bromide-catalyzed oxidative coupling of benzylamines with ortho-substituted anilines: synthesis of 1,3-benzazoles. *RSC Advances* **2015,** *5* (7), 5015-5023.

140. Krebs, C.; Galonić Fujimori, D.; Walsh, C. T.; Bollinger, J. M., Non-Heme Fe(IV)–Oxo Intermediates. *Acc Chem Res.* **2007,** *40* (7), 484-492.

141. Driggers, C. M.; Kean, K. M.; Hirschberger, L. L.; Cooley, R. B.; Stipanuk, M. H.; Karplus, P. A., Structure-Based Insights into the Role of the Cys–Tyr Crosslink and Inhibitor Recognition by Mammalian Cysteine Dioxygenase. *J Mol Biol.* **2016,** *428* (20), 3999-4012.

142. Fellner, M.; Aloi, S.; Tchesnokov, E. P.; Wilbanks, S. M.; Jameson, G. N. L., Substrate and pH-Dependent Kinetic Profile of 3-Mercaptopropionate Dioxygenase from Pseudomonas aeruginosa. *Biochemistry* **2016,** *55* (9), 1362-1371.

Biographical information

Sinjinee Sardar has received her B.Sc., with honors in Chemistry from University of Calcutta, India in 2009. She graduated with Master's degree in Chemistry from Indian Institute of Technology, Madras, in 2011. During her time there, she pursed research under the guidance of Dr. Sundargopal Ghosh on Click-generated triazole based ferrocene-bioconjugates: A highly selective multisignaling probe for toxic metal ions. In 2013, she joined Dr. Brad Pierce's laboratory in the Department of Chemistry and Biochemistry in the University of Texas, Arlington. In her five years there, she has been working on characterizing a Thiol dioxygenase enzyme named 3-Mercaptopropionic acid dioxygenase. Majority of her research involves spectroscopic and kinetic experiments which involves deciphering the role of the “outer-sphere” interactions with the active site of the enzyme and its effect in directing the promiscuous behavior nature of the enzyme.